Jakob Grasserbauer, BSc

In situ Electron Backscatter Diffraction: Recrystallization Behavior and Microstructural Evolution in Al-Mg-Si alloys during heating

MASTER'S THESIS

to achieve the university degree of

Diplom-Ingenieur

Master's degree programme: Advanced Materials Science

submitted to

Graz University of Technology

Supervisor

Oberrat Priv.-Doz. Dipl.-Ing. Dr.techn. Peter Pölt

Co-Supervisor
Oberrat Dipl.-Ing. Dr.techn. Stefan Mitsche

Institut of Electron Microscopy and Nanoanalysis

Graz, February 2018

AFFIDAVIT

I declare that I have authored this thesis independently, that I have not used other than the declared sources/resources, and that I have explicitly indicated all material which has been quoted either literally or by content from the sources used. The text document uploaded to TUGRAZonline is identical to the present master‘s thesis.

Date

Signature

Abstract

In situ electron backscatter diffraction in the scanning electron microscope enables real-time observation of microstructural changes in materials proceeding during heat treatments. Recrystallization has a substantial impact on the final mechanical properties of the material, therefore its control with respect to the improvement of existing and tailoring of new engineering materials is extremely important. In the present work the microstructural evolution of hot rolled AA6016 aluminum sheets, which belong to the group of age-hardenable Al-Mg-Si alloys and are commercially used in the automotive industry, is studied.

The rolling process creates zones with varying shear deformation in the material and this will affect the recrystallization dynamics in the final annealing procedure. The differences in the microstructure at different depths of the hot rolled sheets were investigated. Furthermore, the recrystallization mechanisms and preferential directions of grain growth as well as the changes in the microstructure of samples treated with different heating rates were analyzed especially with regard to nucleation and growth kinetics.

In the last decades a new surface effect emerged, the so-called roping phenomenon, which results in paint brush lines and unpleasant surface quality of the final sheets. It was found to be correlated with the presence of a Cube texture. Therefore, the texture evolution and texture changes accompanying the heat treatments gained center stage in this master thesis and one specified goal was to find an appropriate heat treatment that minimizes the amount of Cube oriented grains in the final aluminum sheets.

Finally, investigations concerning the distribution of the alloying elements and the precipitates formed by them as well as their influence on recrystallization were carried out. The Mg_2Si- and AlFeSi-particles with sizes ranging from about 100 nm up to a few microns can either favor recrystallization by particle-stimulated nucleation (PSN) or pin the grain boundaries by exerting a strong Zener drag. The different recrystallization mechanisms, as well as the occurrence of recovery, were studied in this context.

Kurzfassung

Die *in situ* Elektronenrückstreubeugung im Rasterelektronenmikroskop ermöglicht die Echtzeitbeobachtung mikrostruktureller Veränderungen in Materialien während Wärmebehandlungen. Die Kontrolle des Rekristallisationsverhaltens ist ein wichtiges Thema sowohl bei der Verbesserung als auch der Entwicklung von technischen Werkstoffen, da die endgültigen mechanischen Eigenschaften vieler Materialien stark vom Gefüge beeinflusst werden. Die vorliegende Arbeit untersucht warmgewalzte AA6016-Aluminiumbleche, die zur Gruppe der aushärtbaren Al-Mg-Si-Legierungen gehören und in der Automobilindustrie eingesetzt werden.

Durch den Walzprozess werden Bereiche mit unterschiedlicher Scherdeformation, welche die Rekristallisation stark beeinflussen können, in das Material eingebracht. Unterschiede in der Mikrostruktur in unterschiedlicher Tiefe der Bleche wurden untersucht. Weiters wurden die Rekristallisationsmechanismen, Wachstumsrichtungen der Körner und das Gefüge von Proben, die mit unterschiedlichen Aufheizraten behandelt wurden, hinsichtlich Keimbildung und Wachstumskinetik analysiert.

In den letzten Jahrzehnten wurde ein neuer Oberflächeneffekt (*roping* genannt), der zu reduzierter Oberflächenqualität führt, beobachtet und mit dem Auftreten von Cube-Texturen in Verbindung gebracht. Daher stehen die Texturveränderungen während der Wärmebehandlungen der Bleche im Mittelpunkt dieser Arbeit. Als ein Ziel wurde unter anderem die Entwicklung einer geeigneten Wärmebehandlung, welche zur Verminderung des Anteils der Cube-orientierten Körner führt, vorgegeben.

Weiters wurden die Verteilung der Legierungselemente, der daraus aufgebauten Ausscheidungen und die mit ihnen verbundenen Effekte im Rahmen der Wärmebehandlung untersucht. Die Mg_2Si- und AlFeSi-Partikel mit Größen von etwa 100 nm bis zu einigen Mikrometern können entweder die Rekristallisation durch partikelstimulierte Keimbildung (PSN) begünstigen oder die Korngrenzen durch einen starken Zener-Effekt fixieren, wobei erneut die verschiedenen Rekristallisationsmechanismen sowie das Auftreten von Erholung analysiert wurden.

Acknowledgement

I would like to thank Professor Ferdinand Hofer, head of our institute, for giving me the possibility to write my master thesis at the FELMI-ZFE and Professor Peter Pölt for his superior supervision and all the helpful discussion on the topic of electron backscatter diffraction.

Next, I would like to thank the company AMAG, especially DI Georg Falkinger, for the financial support and the chance to write my master thesis on such an interesting topic.

My greatest gratitude goes to my co-supervisor Dr. Stefan Mitsche, who instructed me on how to handle the SEM, prepare my samples and perform meaningful EBSD scans. His collegial supervision and the interesting discussions made the time at FELMI-ZFE very pleasant.

Further thanks go to my office colleagues and the whole FELMI-ZFE team for the warm welcome and the willingness to help unexperienced students like me with their unsolved problems. It was a wonderful time at the institute.

Special thanks go to my friends and teammates, who supported me during my entire time at the university. Their encouraging words in the moments I felt overstrained and unmotivated helped me passing these situations easily.

Lastly, I would like to thank my family with all of my heart for supporting me throughout my entire life, especially my parents for their unconditional love and enormous backing in all situations.

Table of Contents

List of Abbreviations

Al	Aluminum
AlFeSi	Aluminum-Iron-Silicon
BSE	Backscattered Electrons
°C	Degree Celsius
CCD	Charge Coupled Device
CI	Confidence Index
d_{ss}	Distance between phosphor screen and sample
EBSD	Electron Backscatter Diffraction
EDX, EDXS, EDS	Energy Dispersive X-ray (Spectroscopy)
ET	Everhart-Thornley
Fe	Iron
FSD	Forward Scatter Detector
GTA	Grain Tolerance Angle
HAGB	High Angle Grain Boundary
IA	Intermediate Annealing
IPF	Inverse Pole Figure
IQ	Image Quality
KAM	Kernel Average Misorientation
kV	Kilo Volt
LAGB	Low Angle Grain Boundary
Mg	Magnesium
Mg_2Si	Magnesium silicide
min	Minute
mm	Millimeter
nm	Nanonmeter
µm	Micrometer
ND	Normal Direction
O	Oxygen
ODF	Orientation Distribution Function
OIM	Orientation Imaging Microscopy
PC	Pattern Center
PF	Pole Figure
PSN	Particle-Stimulated Nucleation
RD	Rolling Direction
RT	Room Temperature
SE	Secondary Electrons
SEM	Scanning Electron Microscopy / Scanning Electron Microscope
Si	Silicon
SIBM	Strain-Induced Boundary Migration
SSD	Solid-State Detector
TD	Transverse Direction
WD	Working Distance

1 Introduction and Motivation

The mechanical properties of engineering materials have a major impact on the research and development of products in different fields of industry. Starting from raw materials, the different processing steps influence the microstructure and simultaneously the materials behavior in their later usage. The Al-Mg-Si alloys (6xxx series) belong to the group of age-hardenable aluminum alloys and combine properties like high strength, good corrosion resistance, good formability and lightweight (Engler and Hirsch 2002).

In case of aluminum sheets, the rolling process and subsequent heat treatment control the morphology and crystal orientation of the grains. Their orientations can be either randomly distributed or aligned along a preferred direction. Electron backscatter diffraction (EBSD) in the scanning electron microscope (SEM) can be used to determine the orientations of grains and to investigate the samples' (micro-) texture.

Processing of the Al-Mg-Si alloys involves nearly always heat treatment. To gain deeper knowledge concerning the evolution of the microstructure especially during this processing step, *in situ* investigations of the recrystallization processes during heating are inevitable. To this aim, specifically designed heating stages with adjustable temperature ramps and fast CCD cameras for the recording of OIM (orientation imaging microscopy) maps are necessary. Besides the EBSD technique to gain crystallographic information of the samples, the simultaneous recording of energy dispersive x-ray (EDX) maps of the same area provides information about changes in the distribution of precipitates and the specific alloying elements during heating.

This thesis focuses on the influence of different thermal treatments on the final microstructure and the fraction of texture components in hot rolled Al sheets as well as on the recrystallization mechanisms and their influence on texture banding (Bennett *et al.* 2010) during the heating. Especially the occurrence and development of Cube bands were investigated, which is one specific recrystallization texture component in aluminum and is nowadays said to be responsible for the ridging or roping phenomenon. Roping describes an agglomeration of fine-grained Cube orientations, which result in an uneven surface during forming. Besides affecting the sheets anisotropy and acting as strain concentration sites, the Cube bands can also lead to the so-called paintbrush lines, which display a diminished surface quality (Engler and Hirsch 2002; Hirsch and Al-Samman 2013).

2 Fundamentals

This chapter provides general information concerning scanning electron microscopy, electron backscatter diffraction, and texture analysis, which are a necessity for the understanding of the work in this thesis.

2.1 Scanning Electron Microscopy

In a scanning electron microscope (SEM), an electron beam is focused on the surface of a specimen and the incident electrons interact with the sample. Generating various interaction products, which can leave the sample, the electrons can be detected and be distinguished by their energy.

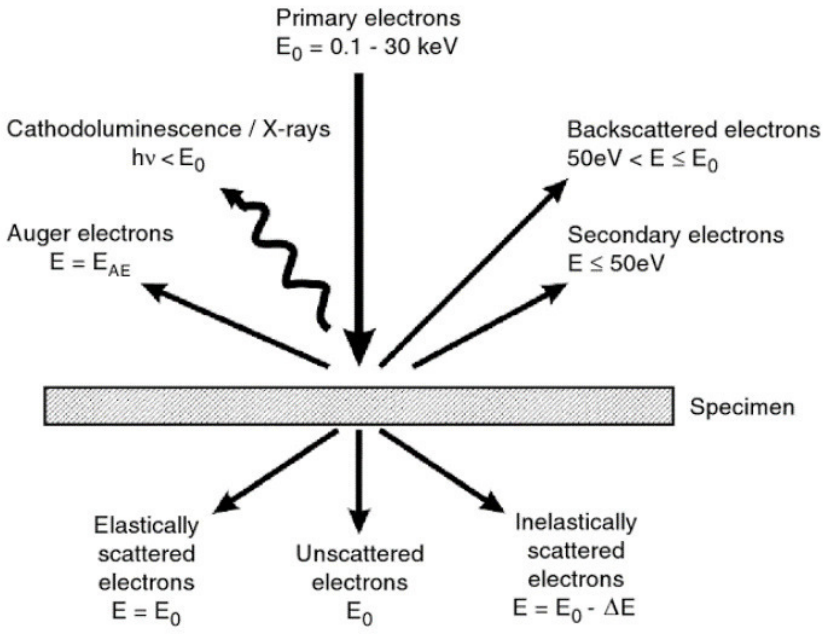

Figure 2.1: Primary electron beam-specimen interaction and the resulting radiation (Hawkes and Spence 2008)

Figure 2.1 shows the interaction products of the electrons with a thin electron transparent specimen. An elastic scattering process is lossless, whereas in an inelastic scattering process the electrons lose energy. The different electron signals provide information about the morphology, the chemical composition and the crystal structure of the sample. However, in an SEM generally bulk specimens are used and in that case the signals in the lower part of **Figure 2.1** are of course no longer available.

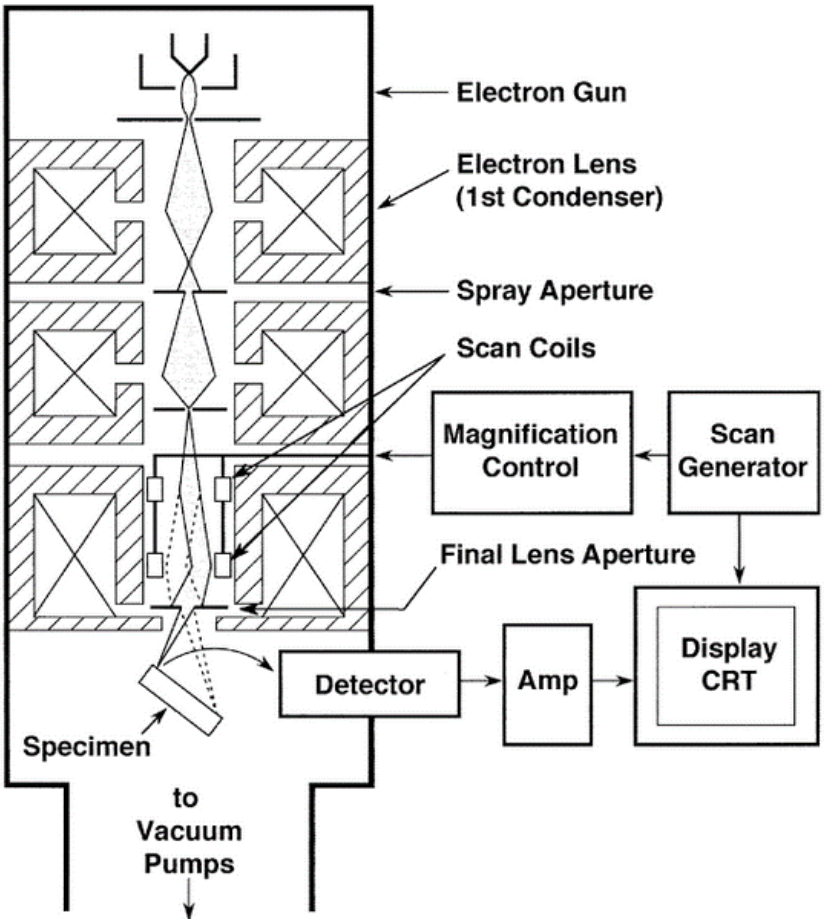

Figure 2.2: Schematic representation of the SEM electron column (Goldstein *et al.* 2003)

Figure 2.2 illustrates schematically the most important parts of an SEM. The electrons generated by an electron gun are accelerated to a predefined energy (0.1-50 keV), and the source radius at the gun exit is decreased by the use of electron lenses (demagnification) and apertures. Scan coils deflect the electron beam across the surface of the specimen and deliver image contrast from point to point as specified by the pixel size. The total system requires high-vacuum conditions, which are generated by different vacuum pumps. The apertures in the SEM are used to adjust the beam current. Especially in case of EBSD measurements or x-ray maps higher currents lead to an improvement in the signal-to-noise ratio for a predefined time, but also cause a stronger contamination and potentially damage of the sample surface.

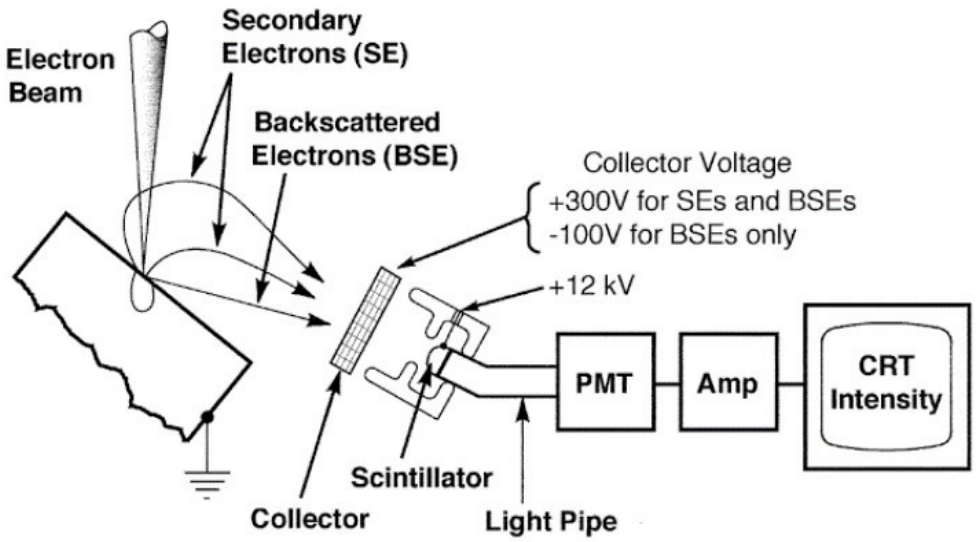

Figure 2.3: Detection methods for SE and BSE in the SEM (Goldstein *et al.* 2003)

Figure 2.3 shows the arrangement of the detectors relative to the specimen and the detectors for the signal collection. For imaging, one can use either the secondary electron (SE) signal collected with an Everhart-Thornley detector or the backscattered electron (BSE) signal using either the ET-detector or a dedicated BSE detector like the solid-state-detector. The schematic drawing does not show the SSD-detector, which is usually placed below the lowest pole piece. Beside the imaging mode, many SEMs are also provided with a detector for energy dispersive x-ray spectroscopy (EDX). This method is a powerful analytical tool to investigate phase distributions in samples. The primary electron beam generates not only SE and BSE but also x-ray photons, which have specific energies corresponding to the element of their origin.

The final resolution and image quality are strongly influenced by different components in the SEM. The choice of the proper electron source is crucial to get high resolution. Often thermal emitters are used because of their low cost, but for high-resolution imaging field emission guns are a necessity. For focusing and defocusing as well as deflecting the electron beam on the sample surface, magnetic lenses are used. Similar to optical glass lenses they also suffer from a number of lens aberrations (astigmatism, spherical aberration, chromatic aberration, …), which can only be minimized but never completely canceled out using multipole lenses and a monochromator. However, apart from astigmatism, correctors for lens aberrations are not integrated into SEMs (Goldstein *et al*. 2003; Hawkes and Spence 2008).

2.2 Electron Backscatter Diffraction (EBSD)

The information and detailed images obtained by conventional electron microscopy do often not meet the requirements of the user. EDX, for example, provides information about the elements in the sample and their concentrations but does not give information about the oxidation state and bonding. Yet, when even EDX measurements are not sufficient for complete sample characterization, crystallographic analysis can bring light into the darkness. In the scanning electron microscope, one has the possibility to use the electron backscatter diffraction technique to gain crystallographic information with a lateral resolution down to 50-100 nm.

2.2.1 Principle Set-up and influencing factors

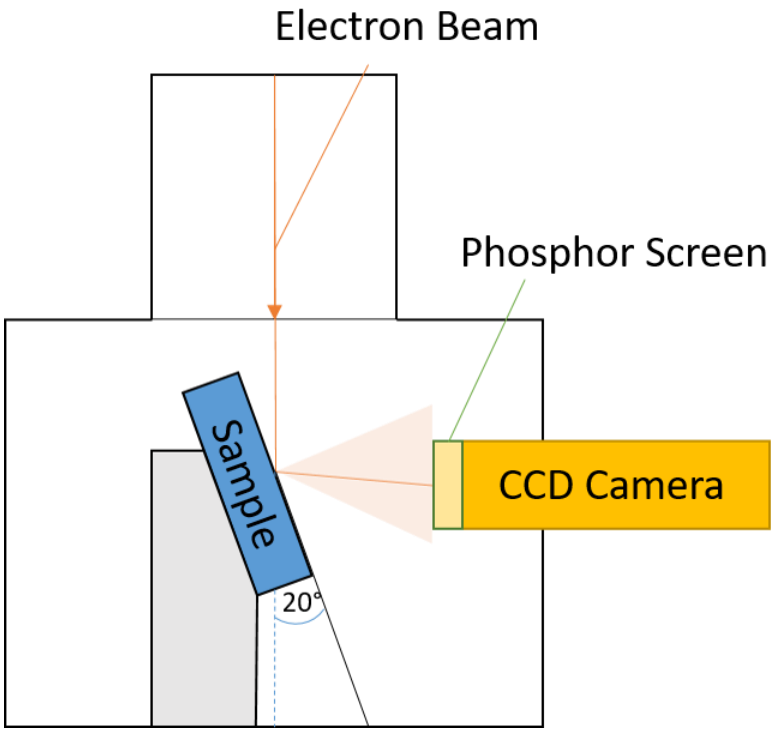

Figure 2.4: Set-up principle for EBSD measurements

Figure 2.4 shows the principal set-up for EBSD measurements, where the primary electron beam is scanned across the specimen surface. The incoming electrons are inelastically scattered, with some electrons hitting the crystal at a Bragg reflecting position, and contain the crystallographic information of the irradiated point. When these backscattered electrons hit a phosphor-coated screen, a specific pattern (Kikuchi pattern) is observed. For each obtained Kikuchi pattern, a CCD camera takes an image for further evaluation. The Kikuchi lines in this

pattern correspond to zone axes of the sample crystal system and indexing of these gives the crystal orientation at the sampled point. After finishing the indexing process, the electron beam jumps to the next point on the specimen, with the step-size defined by the user. A proper choice of the step size is crucial to get meaningful crystallographic maps.

A variety of factors influences the quality of the obtained Kikuchi pattern. The accelerating voltage E_0 defines the penetration depth of the electrons and therefore the spatial resolution. For higher beam currents, more of the primary electrons are backscattered and thus lower measurement times can be chosen. However, while the beam diameter increases and thus the lateral resolution decreases, the specimen drift and contamination can deteriorate the resolution.

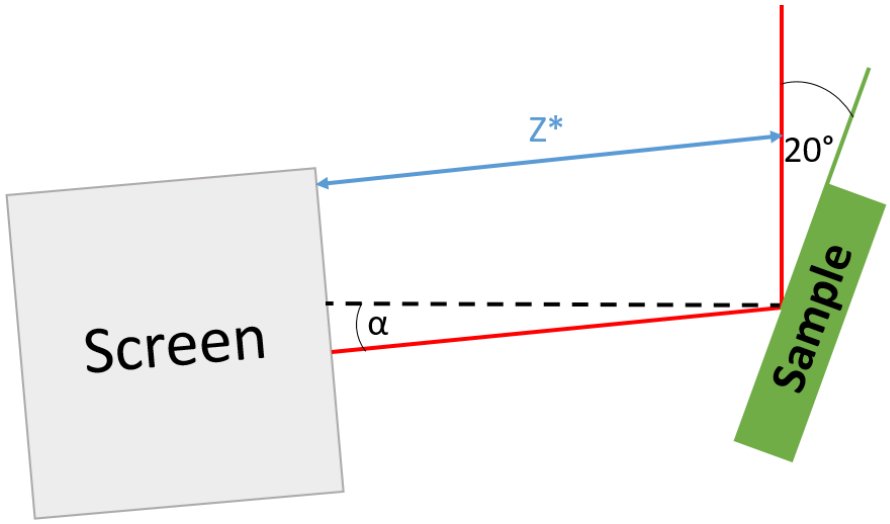

Figure 2.5: More detailed geometrical arrangement of the EBSD system

Figure 2.5 illustrates the geometrical relationships in EBSD. The angular distribution of the backscattered electrons is strongly dependent on the incidence angle of the primary electron beam. Whereas for normal incidence (0°) the distribution can be approximated by a cosine law, for large incidence angles most of the backscattered electrons are reflected at an angle corresponding to the reflection of light. Therefore, that most of the backscattered electrons hit the phosphor screen, specimen tilt larger than 45° is necessary. A 70° tilting angle is a good compromise because for larger angles one obtains excessive anisotropy of the sampled volume (Randle and Engler 2000).

The distance between the phosphor screen and the specimen surface also plays an important role concerning the calculation of the crystal orientation. For standard EBSD measurements, the screen, mounted on a movable holder, is brought close to the sample surface. As sketched

in **Figure 2.5**, the combination phosphor screen – camera is tilted about 5 degrees to the normal of the incident beam. These geometrical aspects play an important role for pattern evaluation that will be discussed in section 2.2.3.

At least the influence of the working distance has to be mentioned. Usually for minimized focusing distortions and best resolutions, small values of the WD are necessary. In general, the geometry of the SEM and the EBSD system are limiting factors in minimizing the working distance. Especially in the case of *in situ* EBSD using a heating device, one has to go to larger working distances to avoid any risk of collisions of microscope parts. This can result in a decrease in the pattern quality and furthermore in problems concerning pattern indexing.

2.2.2 Models for EBSD: Formation of Kikuchi Patterns

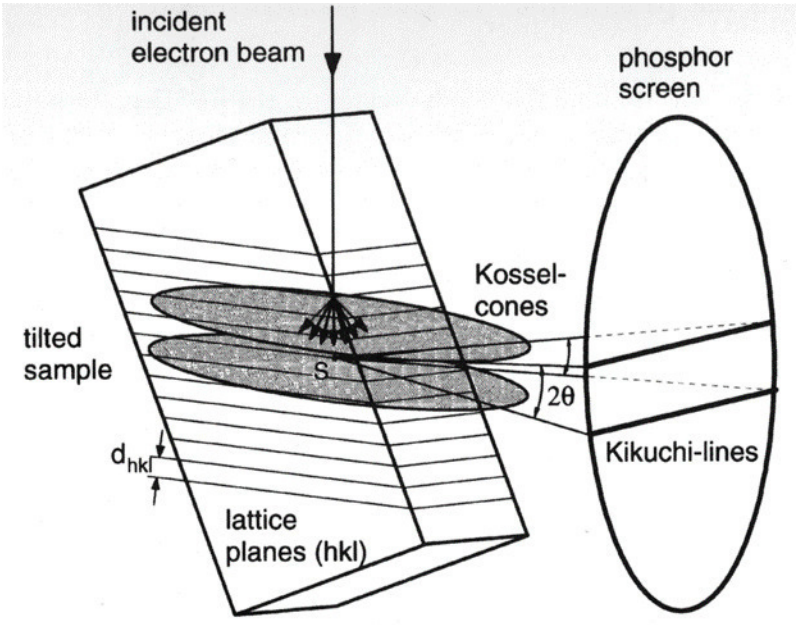

Figure 2.6: Formation of Kikuchi lines from EBSD perspective (Schwartz *et al.* 2000)

The BSE can be used for imaging and contain some chemical information. Because the inelastic scattering of the BSE is diffuse, they travel in all directions through the crystal lattice of the sample and some of them fulfill the criteria described by Bragg's law:

$$n\lambda = 2d_{hkl} \sin\theta$$

These electrons can be elastically scattered again to build a reinforced beam. Because the diffraction of the BSE occurs again in all directions, the diffraction radiation spreads out from the source considered point, which lies between two lattice planes, on the surface of the geometrical shape of a cone. The apex angle of the named Kossel-cones, two resulting from each family of planes, is $180° - 2\theta_B$. Because of very short wavelength (~ 0.1 Å) and typical values for interplanar spacing d_{hkl} inserted in Bragg's law, the Bragg angle θ_B is only about 0.5°, which results in "straight-looking" conic parallel Kikuchi lines when the Kossel-cones intercept the phosphor-coated screen, although in fact they are hyperboles. The spacing between the lines is proportional to an angular distance of $2\theta_B$, which is also proportional to the interplanar spacing (Schwartz *et al.* 2009).

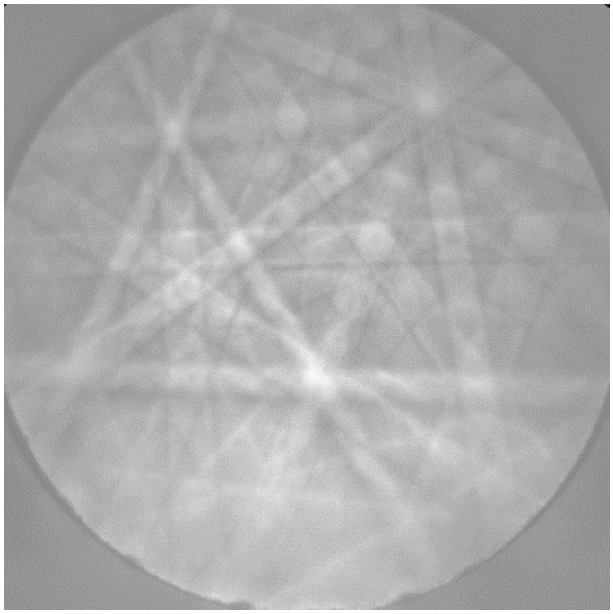

Figure 2.7: Exemplary image of a Kikuchi pattern obtained from EBSD

The Kikuchi bands (pairs of parallel lines), an example of a diffraction pattern is given in **Figure 2.7**, are characteristic for distinct crystallographic planes. The intersection of bands is known as zone axis, with major zone axes corresponding to the intersection of several bands. The Kikuchi pattern contains the full three-dimensional crystallographic information of the analyzed crystal and all angular relationships between the sampled point (volume) and the reference axes (Randle and Engler 2000).

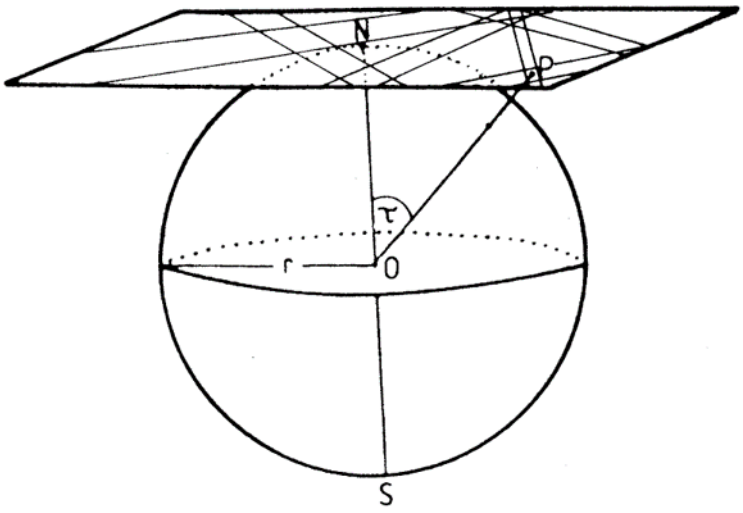

Figure 2.8: Formation of the Kikuchi lines from the gnomonic projection (Randle and Engler 2000)

The Kikuchi pattern is a 2-dimensional projection of the 3-dimensional crystal lattice. In fact, it is a map of the angular relationships between the directions and planes in the crystal. **Figure 2.8** shows the projection process with the help of a reference sphere. The sampled point at the sample surface lies in the center (origin) of a sphere with radius r = ON, which is the distance between the origin and the phosphor screen (tangent "north pole" plane). N also represents the pattern center (PC), which is important for indexing the patterns. The diffracted electron beams intersect the sphere at specific positions, which are projected onto the screen. Because of the geometrical arrangement, the position of a point P (a pole in the pattern) on the screen is given by ON*(tan τ), where τ is the angle between ON and OP and comprises the total crystallographic information (Randle and Engler 2000).

2.2.3 Indexing and Evaluation of EBSD patterns

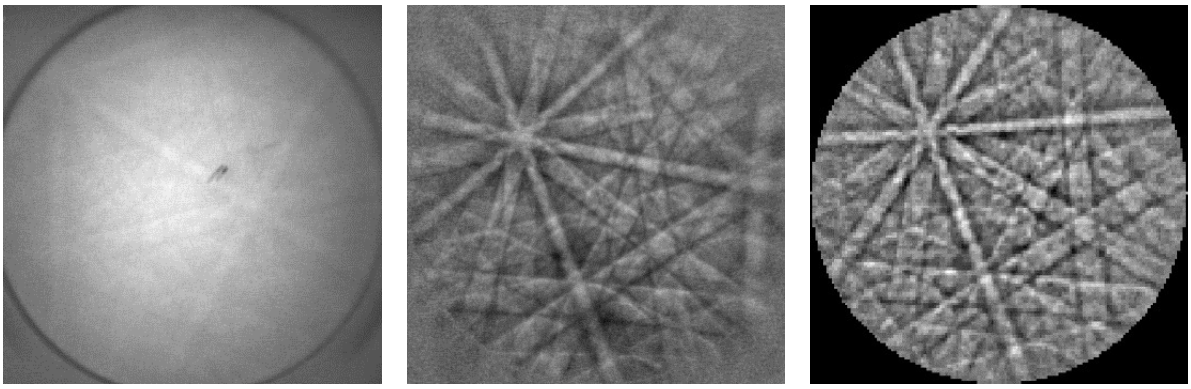

(a) (b) (c)

Figure 2.9: a) "raw" Kikuchi pattern, b) underground-corrected pattern and c) compressed pattern

Starting from raw patterns, one first needs to enhance the signal to noise ratio. Using CCD cameras, this integrating procedure can directly be performed on the chip (**Figure 2.9** (a)). Next, a background correction is required (**Figure 2.9** (b)). Therefore, the background intensity is calculated by integrating the pattern signals of numerous, differently oriented grains. As a result, only the non-uniform illumination of the screen remains. Once the “background” is determined, either it is subtracted from the EBSD pattern or the patterns are divided by the background intensity.

The last step is an image compression, which merges blocks of pixels and replaces them by a single pixel. This does not only speed up the analysis of the patterns but also reduces point-to-point noise. CCD cameras provide this option by direct binning of the chip (**Figure 2.9** (c)). Once the final pattern, after the prior image processing steps, is completed, the bands are extracted from the pattern using the Hough transform (Krieger Lassen 1996), which is an algorithm designed to specifically find lines. The Hough transformation is based on the following equation:

$$\rho = x\,cos(\theta) + y\,\sin(\theta)$$

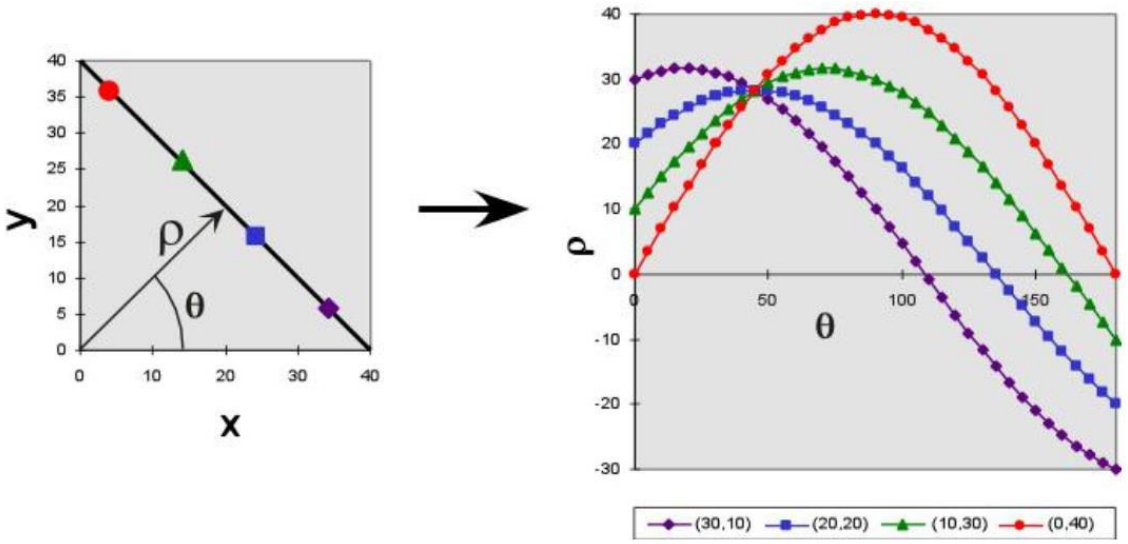

Figure 2.10: Hough transformation from real space to Hough space (OIM 1997)

If an edge detector finds an edge point, the Hough transform will find all the straight lines on which this edge point (x, y) can lie. This means it will assign to every (x, y) pair all possible values of the Hough parameters ρ and θ, giving a line in the Hough space. The lines of all edge points belonging to the same straight line in real space intersect in Hough space, providing the accurate values ρ and θ for that specific line in real space. Thus, the (Kikuchi-) lines in real space transform into points of high intensity (peaks) in the Hough space, with the parameters ρ and θ as designated in **Figure 2.10**.

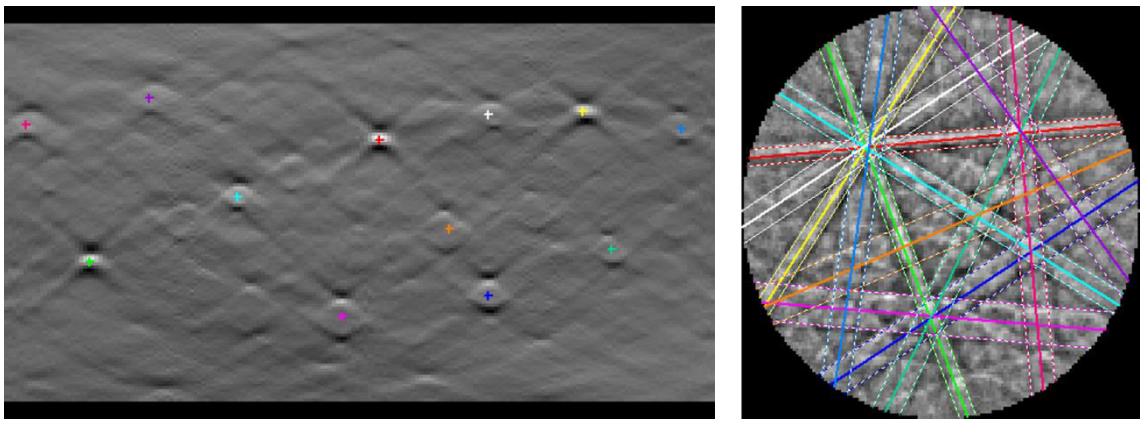

Figure 2.11: Colored dots marking lines in Hough space and indexed Kikuchi pattern

The problem of band detection has now turned into finding peaks of high intensity in the Hough space. These peaks are always accompanied by two surrounding intensity valleys, which arise from the Kikuchi pattern and combined they embody some information about the real-space bandwidths (**Figure 2.11**).

After detecting the bands, the software automatically calculates the corresponding zone axes using the angles and lattice plane spacing. This also requires the exact knowledge of some geometrical parameters like working distance and screen distance (z* in **Figure 2.5**), both influencing the position of the pattern center.

The indexing does not always provide an unambiguous result and thus several different orientations may be found for a given diffraction pattern. The system ranks the respective orientations using various parameters. The two main parameters used for assessing the quality of the indexing are the "confidence index (CI)" and "Fit" value (Schwartz *et al*. 2009). The confidence index is based on the voting scheme for the different orientations and the fit parameter determines the average angular deviation between the detected Kikuchi bands and the recalculated ones. The CI value ranges from 0 to 1 with higher values indicating more reliability of the indexing.

The final orientation determination of the crystal is done by determining the position of the crystal coordinate system relative to a reference system. Using rolled material sheets, the typical reference system is set up by the rolling direction (RD), normal direction (ND) and transverse direction (TD).

2.3 Representation of EBSD data and Texture Analysis

Many properties of a material depend strongly on its microstructure. Because EBSD analyzes the microstructure and simultaneously the microtexture, it tremendously increases our capabilities in this field. The type of representing the gained data, especially for texture analysis, where three-dimensional spatial relationships are translated into two dimensions, mostly governs the final interpretation of the EBSD measurement. This section sketches different possibilities of EBSD data representation, especially the ones used in the experimental part of this thesis.

2.3.1 Representation of EBSD data

Image Quality

Besides the Euler angles containing the crystallographic information of the crystal, the EBSD system also stores an "image quality (IQ)" value, describing the quality of the Kikuchi pattern of each sampled point. It is essentially the sum of the detected peaks in the Hough transform of the pattern.

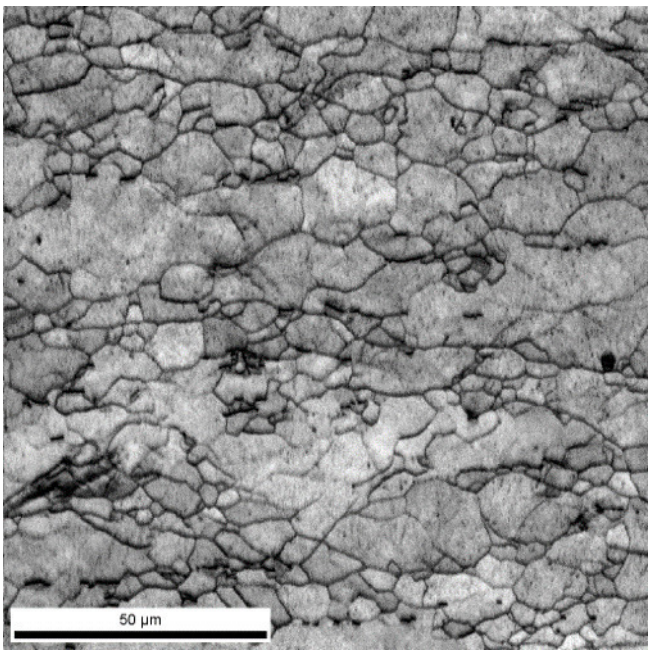

Figure 2.12: Image Quality map obtained after Hough transformation

Figure 2.12 shows the IQ-plot of an EBSD measurement. The image quality of a pattern is not only influenced by the electron beam properties during pattern recording, but also by intrinsic materials properties, surface effects, lattice distortions, and e.g. the video processing. Therefore, this style of representation leaves a large scope of interpretation. Grain boundaries, inclusions, and pores but also mechanical damage (scratches, grooves) are all displayed as dark regions in the image, which puts the distinction between all these factors often into the user's hands and his experience.

Kernel Average Misorientation (KAM)

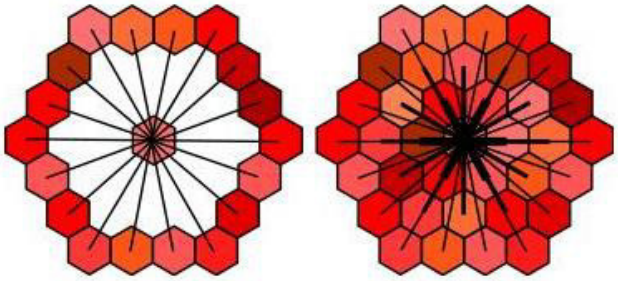

Figure 2.13: Kernel and pixel arrangement in the Kernel average misorientation calculation (OIM 1997)

The Kernel Average Misorientation calculates the misorientations between the center point of the Kernel and the neighboring points. A specific selection of the points is up to the user. The average misorientation value is then assigned to the center point and plotted with a color gradient (**Figure 2.13** and **Figure 2.14**).

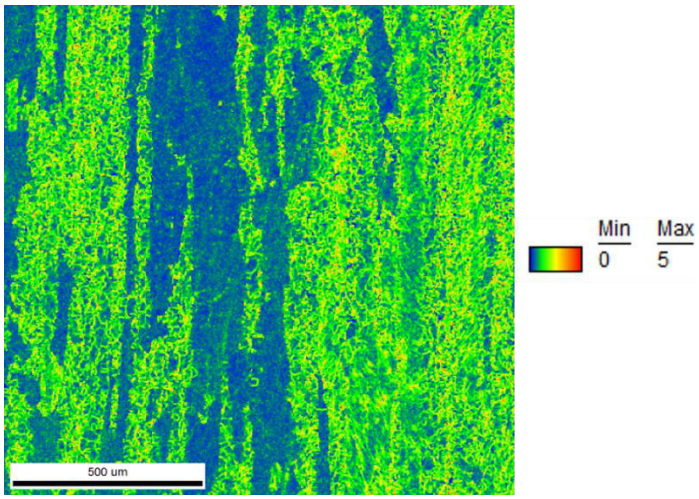

Figure 2.14: KAM map indicating regions of lower and higher residual stresses

The misorientation between neighboring points is an indication of residual inner stresses of the material, which depend on the dislocation density. Grains with higher dislocation density have more stored energy and can act as starting sites for the strain-induced boundary migration (SIBM) recrystallization mechanism (Beck and Sperry 1950).

Pole Figure and Inverse Pole Figure

One of the most common types of EBSD data representation is the use of Inverse Pole Figure (IPF) and Pole Figure (PF) plots. Both are 2D illustrations of the 3D crystallographic data, based on a stereographic projection, which is in principle similar to the gnomonic projection shown in **Figure 2.8**.

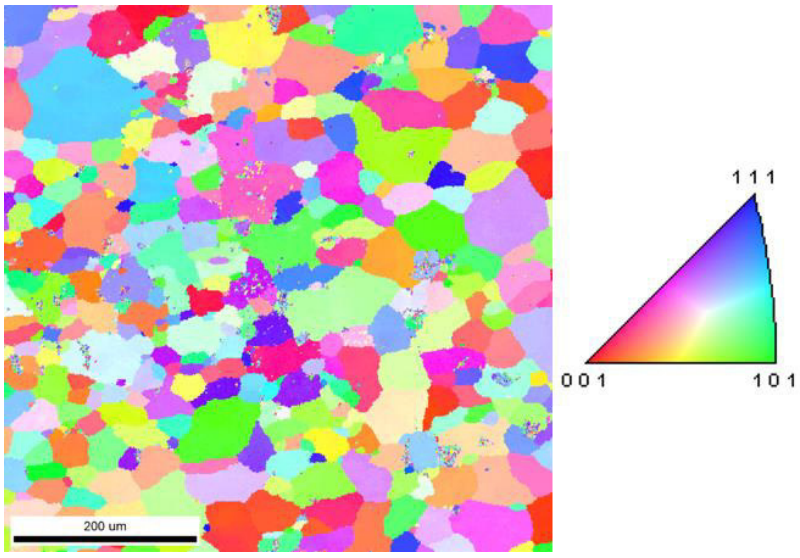

Figure 2.15: [001] Inverse Pole Figure map obtained from a hot rolled Al sheet

The IPF map, exemplarily shown in **Figure 2.15**, depicts the distribution of a selected direction in the specimen in relation to the crystal axes. As the name already tells, it is exactly inverse to the usual Pole Figure (PF), where the position of a pole (normal to a lattice plane) relative to the sample reference frame is shown. The complete interpretation of IPF maps is difficult and needs a lot of experience, but it easily shows the orientations of the different grains and gives first evidence for textural governing of the samples microstructure.

The standard projection (for cubic crystal symmetry) for IPF only shows $1/24^{th}$ of the complete stereographic projection, because all of the 24 unit triangles in the reference spheres basic circle are similar.

Using rolled sheet materials, the PFs are usually labeled with the sample directions RD, ND, and TD. A PF contains the projected intersections of the poles of a specific lattice plane with the reference sphere from all different grains. Considering the {100} pole figure of a cubic material, this plot shows only the spatial locations of the poles corresponding to the {100} planes. Normally these intersections are not plotted as points but as contour lines instead, all assigned to a specific number times random. Clustered points in a PF plot indicate a textured material sheet and the number assigned represents the density of the poles. Values greater than 1 times random denote a concentration of poles, which actually represents a textured material (Suwas and Ray 2014).

Orientation Distribution Function (ODF)

The orientation distribution function ODF is a probability density function describing the probability of finding a grain with an orientation g within a given distance in orientation space (Δg) of a specified orientation g_0 in a polycrystal or within the volume fraction of material oriented within Δg of g_0 (OIM Manual, OIM Analysis). Bunge and Morris found that the orientation distribution function, which is mathematically a series of generalized spherical harmonics, could represent the density of all points in the 3d orientation space. The orientation parameters $\varphi 1$, Φ and $\varphi 2$ (Euler angles) define an orientation space, where clusters of points resulting from the orientation of the specimen indicate a textured material. The ODF plots usually use the parameters $\varphi 1$ and Φ as axes and are plotted in constant spacings of $\varphi 2$, depicting the crystallographic information without any projection and loss of information. Although ODF plots are the most powerful method of data representation, the interpretation is more difficult, which makes it unfavorable for inexperienced users.

2.3.2 Texture Analysis

For further improvement in materials properties, not only the alloying elements and thermomechanical processing are of major interest, but also the control of the development of texture components gained center stage in the last years. Texture-related problems occur in many materials, but here I only want to mention the relevant fibers for rolled aluminum sheets.

A texture is defined as the accumulation of similarly oriented grains in the material, in the present case the rolled aluminum sheets. This orientation cannot only be introduced during the rolling process (→ rolling texture), but also during the subsequent thermal heat-treatment (→ recrystallization texture), both leading to characteristic texture components.

Table 2.1: Major rolling and recrystallization texture components in Al sheet alloys (Engler and Hirsch 2009)

Designation	Miller indices {hkl}<uvw>	Euler angles φ1, Φ, φ2
Cu	{112}<111>	90°, 30°, 45°
S	{123}<634>	59°, 34°, 65°
Bs	{011}<211>	35°, 45°, 0°/90°
Goss	{011}<100>	0°,45°, 0°/90°
Cube	{001}<100>	0°, 0°, 0°/90°
R	{124}<211>	53°, 33°, 60°
P	{011}<122>	65°, 45°, 0°/90°
Q	{013}<231>	45°, 15°, 10°

The components can be specified by either Miller indices or Euler angles. Because textures are often introduced by an axially symmetric deformation, they can be described by the crystallographic direction <uvw>, which is (nearly) parallel to the axis of deformation, and a plane normal (hkl), which is parallel to the sample surface.

This thesis focuses especially on the occurrence of the Cube component in the recrystallization texture. Cube oriented nuclei emerge from the so-called Cube bands, which are transition bands of unstable orientations or deformed grains with retained Cube orientation (Engler and Hirsch 2009). One major goal of the thesis is to find a way to reduce the amount of the Cube component with an intermediate annealing process, because from this component the ridging or roping phenomenon (Baczynski *et al*. 2000) originates, which leads to undesirable surface finish after paint bakery cycles.

3 Heating Device

This section provides general information on the heating device, the calibration of the OIM software and the EBSD set-up for usage of the heating device as well as the results of the *in situ* measurements.

3.1 Specifications

Specially designed for SEM and EBSD usage, the CH0-4 heating device by Kammrath &Weiss provides temperatures up to 1050 °C. In combination with the HCS cooling system (Kammrath & Weiss) and the JUMO Dtron 304d PID-controller, the temperature ramp can be controlled manually or automatically.

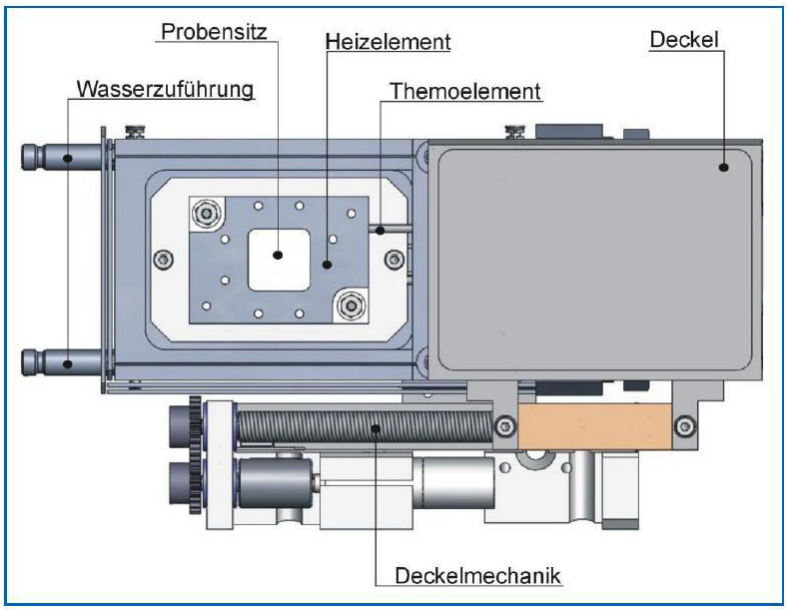

Figure 3.1: Representative image of the CH0-4 heating device (Kammrath and Weiss, n.d.)

Figure 3.1 shows the main parts of the heating device. Beside the water-bearing ports and the motor-operated cover panel, a NiCr-Ni (type K) thermocouple enables temperature measurements from 400 °C to 1050 °C (± 1 °C). The sample position at the heating stage is surrounded by the heating elements (Kammrath and Weiss, n.d.).

The HCS cooling system saves the heating device mechanics, apart from sample and heating elements itself, from heat-damage. The flow rate and temperature of the used cooling liquid are automatically controlled by the system.

The Jumo Dtron 304d is a compact temperature controller providing programming functions. Using the device manually, one can set either the heating power (in %) or a nominal stage-temperature value (in °C). Using the nominal value, the controller automatically heats up to this temperature and holds it.

3.2 EBSD / OIM Calibration

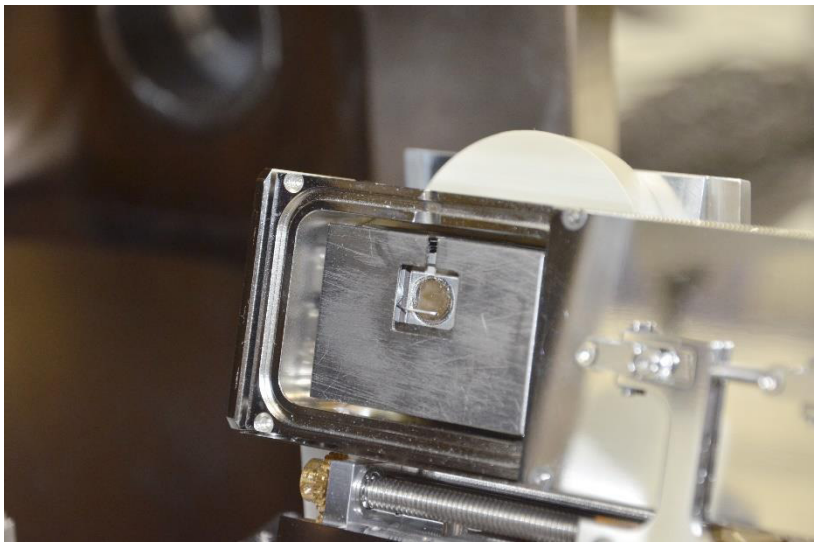

Figure 3.2: Heating device mounted on the pre-tilt holder for EBSD measurements

Figure 3.2 shows the heating device mounted for EBSD *in situ* measurements. The specimen is fixed on the stage with a tungsten pin and molybdenum panels cover the heating element for heat deflection issues.

The set-up is placed in a ZEISS Ultra 55 scanning electron microscope, equipped with EDAX EDX- and WDX-detectors (**Figure 3.3**). The EBSD system is retractably mounted at one of the ports of the SEM, with the possibility to change the camera used for imaging the Kikuchi patterns. Because the fast-frame camera provided not sufficient image quality, all measurements were performed using the high-resolution camera, resulting in lower scan speed and thus longer measurement times.
Right below the phosphor screen a forward scatter detector (FSD) is mounted. Because at higher temperatures the thermal radiation of the samples overexposes this detector, a special cover was designed for protection.

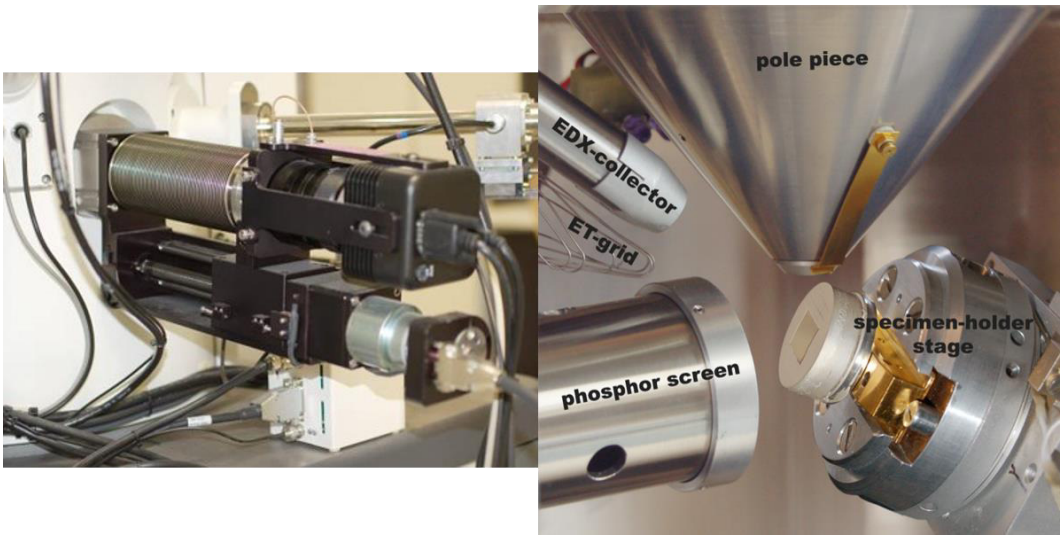

Figure 3.3: Arrangement of the microscope hardware for EBSD measurements inside and the EBSD set-up on the outside of the SEM

The TSL OIM^{TM} Data Collection software provides a variety of options for data acquisition and pattern quality improvement. General parameters for all measurements were 20 kV accelerating voltage and a 240 µm aperture used in high current mode.

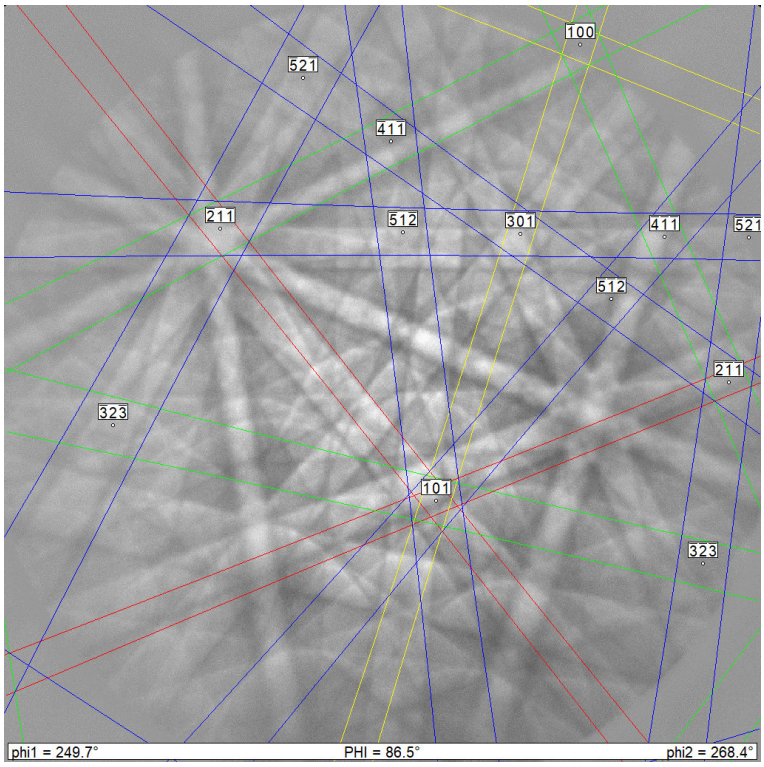

Figure 3.4: Indexing of the Kikuchi pattern for high WD before calibration; CI = 0.01, Fit = 2.24

Because of the higher working distances and modified phosphor screen to sample length (d_{ss}) in comparison to conventional EBSD measurements, the OIM software needed to be calibrated to get a reliable indexing of the patterns (**Figure 3.4**). To this aim, a Ni-standard sample was used on the typical 70° tilt holder (no heating device) and patterns were recorded for working distances starting from 7 mm up to 30 mm. Afterwards, a variation in the screen distance was realized at two different working distances. The measurement of d_{ss} was done outside the microscope using the distance between two edges on the external EBSD stage because there was no possibility to obtain absolute length values of that distance in the SEM chamber.

For calibration, the system the x*, y* and z* values, which describe the position of the pattern center at the phosphor screen and its distance to the analysis point at the sample surface (**Figure 3.5**):
x*, y* - position of the PC on the screen
z* - the distance between sample point and screen

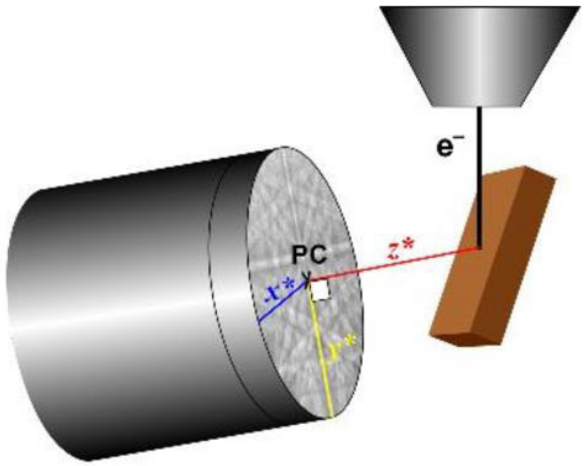

Figure 3.5: Position of the Pattern Center in relation to the sample surface (OIM 1997)

The values are expressed in percent making absolute distance measurements redundant. The PC is purely geometrical, though it is not affected by E_0, spot size or other microscope operating parameters (OIM 1997).
Having a look at **Figure 3.5**, a change in working distance will definitely influence y*. To allow for all angular relationships, z* will also undergo a slight change, whereas x* should remain constant.

The goal was to derive a formula for the calculation of the x*, y* and z* values for all possible working- and screen-distances d_{ss}. Based on the reliability of the x*, y* and z* values of two indexed patterns having high CI and low Fit parameters. The difference of these values in terms of the change in working distance was calculated. The following formulas were derived:

$$y^* = y^*_{standard} - 2.95 * \Delta WD$$
$$z^* = z^*_{standard} - \sin(\alpha) * \Delta WD$$

The parameters $y^*_{standard}$ und $z^*_{standard}$ come from the two Kikuchi patterns mentioned earlier and build the arbitrary origin for all calculations.

The change in z* depends on the angle α describing the inclination of the camera to the horizontal (**Figure 2.5**). First calculations were done with a nominal α value of 5°, the value given by the service technician installing the EBSD system. Not showing the desired improvement in pattern indexing with the new numbers for x*, y* and z*, a recalculation of α was necessary. Based on the two well-indexed patterns, the angle minimizing the misfit in the derived formula and therefore enhancing indexing quality was found to be 7.65°, which was set for all later EBSD measurements.

Once the system was calibrated concerning the working distance, the screen-sample distance was varied for constant WD values. As the EBSD detector screen is retracted, it influences only z* (x*, y* remain constant).

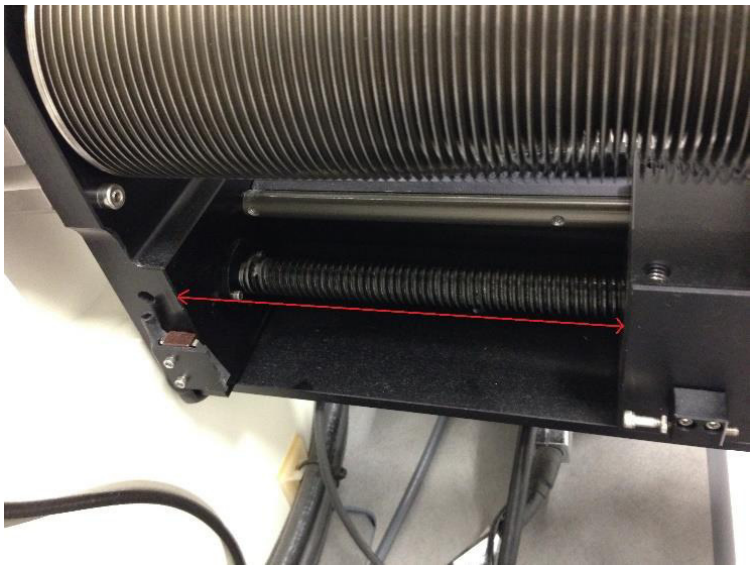

Figure 3.6: Edge-to-edge distance for d_{ss} measurement outside of the microscope

Starting from the completely inserted screen (d_{ss} = 11 mm), it was retracted in steps of a few millimeters, after every step imaging the Kikuchi pattern of the Ni-standard specimen again. To deduce the corresponding formula for z* in this context, the same method as above using two high-quality patterns of two different WD was applied, resulting in

$$z^* = z^*_{standard} + 2.8 * \Delta d_{ss}$$

After optimizing x*, y* and z* for all different working distances and setting the new values as default, the pattern shown in **Figure 3.4** was indexed again, which led to an enormous improvement of index quality (**Figure 3.7**).

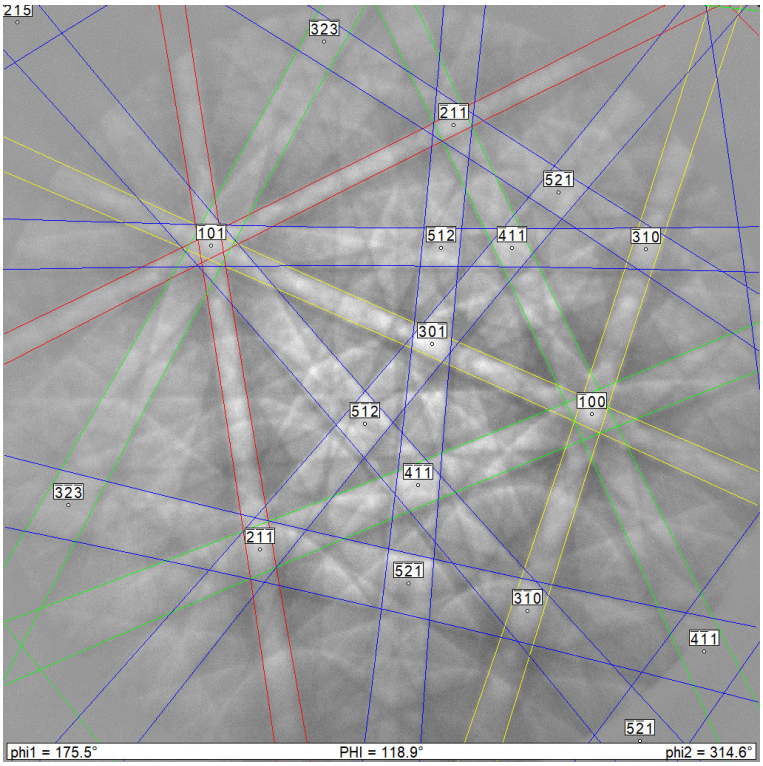

Figure 3.7: Indexed Kikuchi pattern after calibration of the pattern center; CI = 0.94, Fit = 0.32

Comparing **Figure 3.4** and **Figure 3.7**, the gain in accuracy of bandwidth and band-position is tremendous, measurable in the improvement of CI and Fit values.

Concerning the retraction of the EBSD system, for larger distances between sample and screen only smaller sections of the resulting diffraction pattern intersect the phosphor screen, thus the indexing becomes more complicated. Another import factor is the intensity of the diffraction radiation arriving at the phosphor screen, which decreases rapidly for higher distances. Besides these negative aspects, the change in convergence angle improves the resolution of the Kikuchi lines on the screen. This is utilized in sample strain measurements, where very small misorientations occur emerging from an accumulation of dislocations.

3.3 Temperature at specific positions inside the SEM

The major advantages of *in situ* EBSD are based on the continuous observation of changes in microstructure occurring during heating, deformation or other strains. It enables, therefore, the nearly exact determination of the parameters of the applied stress, at which especially instantaneous changes in structure, crystallinity etc. happen.

At low temperatures at the heating stages heat radiation will not affect any parts of the system, but for higher temperatures, the heat-affected zone is increased and may damages some of the surrounding microscope parts. Three thermocouples were mounted at different positions in the specimen chamber of the SEM to measure the temperature-profile at the respective positions during heating. Specially designed for the protection of the BSE detector, which is mounted at the pole piece of the microscope, a metallic cover was installed before the first measurements were done. One thermocouple was placed on the BSE protector, one in the middle of the EBSD screen and the last one on the FSD detector, which was used without the cover panel mentioned in 3.2 **(Figure 3.8)**.

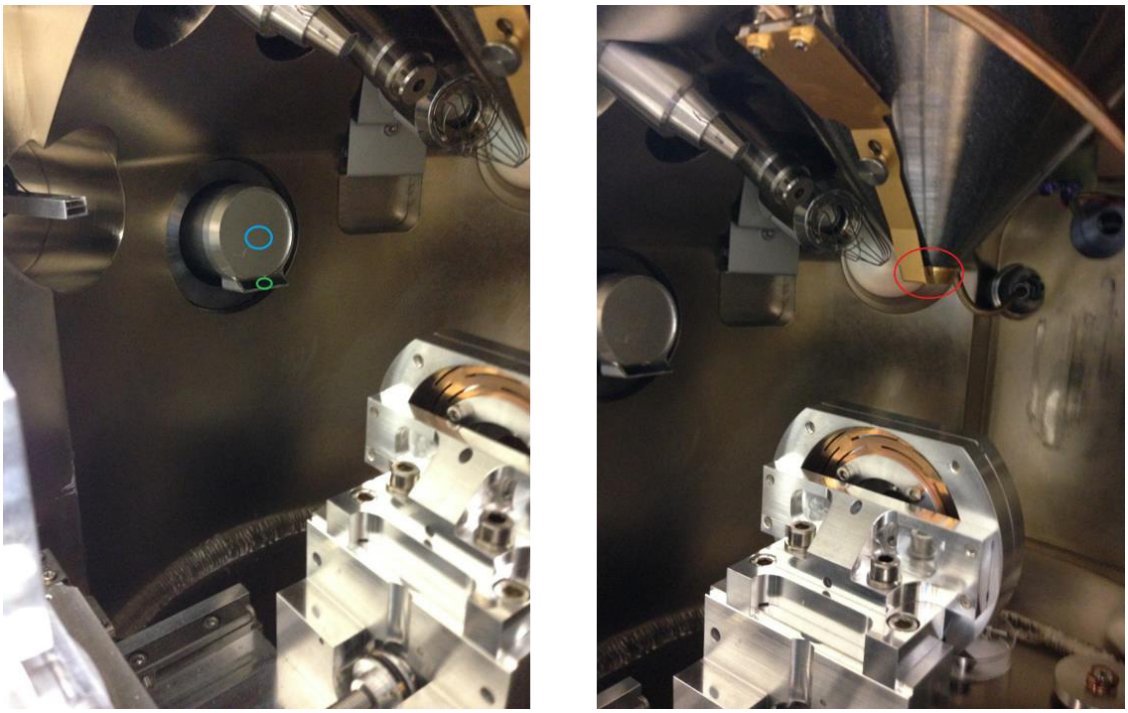

Figure 3.8: Thermocouple positions inside the SEM for temperature profile measurements (blue at the phosphor screen, green at the Forward scatter detector, red at the BSE detector (pole piece))

The heating device was mounted at a position used for the EBSD measurements later on, but without any sample inside. The EBSD screen and FSD detector were inserted in the SEM as

close as possible to the heating stage, resulting in a distance of d_{ss} = 12 mm, measured outside the SEM. The temperature was slowly increased starting from room temperature up to 950 °C. Initially, to avoid any damage, maximum temperatures at the different detectors had to be chosen. When reached, the heating process had to be stopped. For the EBSD and FSD a maximum temperature of 80 °C was chosen. The maximum tolerant screen temperature was valued as 130 °C, estimated from the critical temperatures for some polymeric components in the screen coating.

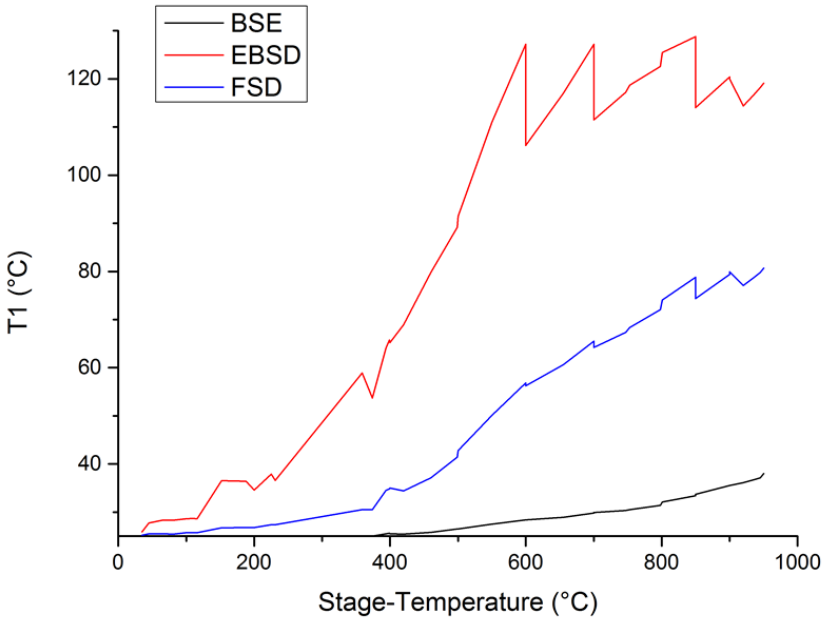

Figure 3.9: Temperature profiles of the thermocouples placed at different positions inside the SEM; Stage-Temperature (°C): actual stage temperature, T1 (°C): temperatures measured at the Backscatter detector, EBSD Screen, Forward scatter detector

The temperature profiles of the different thermocouples are shown in **Figure 3.9**. Evaluating the detector temperatures for different stage temperatures, it is noticeable that only at the phosphor screen of the EBSD system the critical temperature was reached.

The temperature increase at the BSE detector starts only at a temperature of 400 °C at the heating stage and the maximum temperature is around 40 °C, which is only half of the critical value. The actual BSE temperature is influenced by the distance to the heating stage, which is represented somehow in the working distance, although the topmost part of the tilted heating stage is much closer to the detector than the sample. Since this measurement was done at 25 mm working distance, meaning the very small distance between upper heating device frame and BSE protection screen, it should be representative for the temperature evolution.

Comparing the curves of the FSD and BSE detector in **Figure 3.9**, the FSD nearly reaches its limit for stage temperatures above 800 °C. The faster heating of the FSD is based on the smaller distance to the sample and of course the tilt of the heating device, which emits the thermal radiation in the direction of the screen and FSD.

The fastest and largest increase in temperature can be observed at the phosphor screen of the EBSD. The limit of 130 °C was reached at a stage temperature of about 600 °C. For higher stage temperatures, the EBSD system was retracted a little bit to avoid damage, which resulted in the sawtooth-like shape of the EBSD temperature profile in **Figure 3.9**. After every retraction, the new sample to screen distance was measured and tabulated. To simulate real EBSD measurements, the temperature was held at specific stage temperatures for about 10 min.

Table 3.1: Minimum necessary sample to screen distances for temperatures up to 950 °C

Temperature / °C	Edge-edge distance d_{ss} / mm
600	12
700	20
750	30
800	36
850	42
900	50
950	52

The minimum necessary distances d_{ss} measured on the outside of the microscope are listed in **Table 3.1**. Starting from 12 mm at 600 °C, the distance increased up to finally 52 mm at 950 °C. The increased distance makes the indexing of the resulting Kikuchi patterns more complicated. If sufficient index quality is not reachable at 52 mm distance, the distance needs to be decreased, which then causes problems with the screen temperature, with two options to deal with. First, some extra protection panels situated at the heating device could decrease the thermal radiation reaching the screen or second, the EBSD scan duration at the elevated temperature is reduced using faster cameras. It is necessary to continually observe the screen temperature while using distances lower than the ones given in **Table 3.1** because otherwise damaging could not be excluded. The problems mentioned above do not occur during the *in situ* measurements at Al alloys because the maximum temperature used was 600 °C, which is already close to the melting point of aluminum (T_M = 660 °C).

4 *In situ* EBSD: Aluminum hot rolled sheets

4.1 Introduction and Preparation

The industrial use of aluminum started numerous decades ago, when different high strength variants were available. Newer developments led to the usage in other applications, most common example is the automotive industry. Here the fabricators used the good formability and strength combined with high corrosion resistance to produce door panels and other car body parts. The 6xxx Al-Mg-Si alloys belong to the age-hardenable aluminum alloys group, getting their strength and mechanic properties in some final heat treatment cycles and requiring high surface quality of the rolled sheets for automotive use (Hirsch and Al-Samman 2013).

The aluminum sheet properties are strongly influenced by the mechanical processing steps shown in **Figure 4.1**. Starting from bauxite, via the Bayer- and Hall-Heroult-process "pure" aluminum is obtained. The alloying elements are admixed for specific material properties and further processing. Starting with the homogenization heat treatment, the bulk aluminum is hot rolled in a multi-step rolling process and either cooled on air or water quenched. Following this, the sheets are cold rolled to their final thickness, which is about 0.9-1.2 mm. The last steps are solution treatment and aging, which can be integrated into the paint bakery cycles in the automotive industry for example (Burger *et al.* 1995).

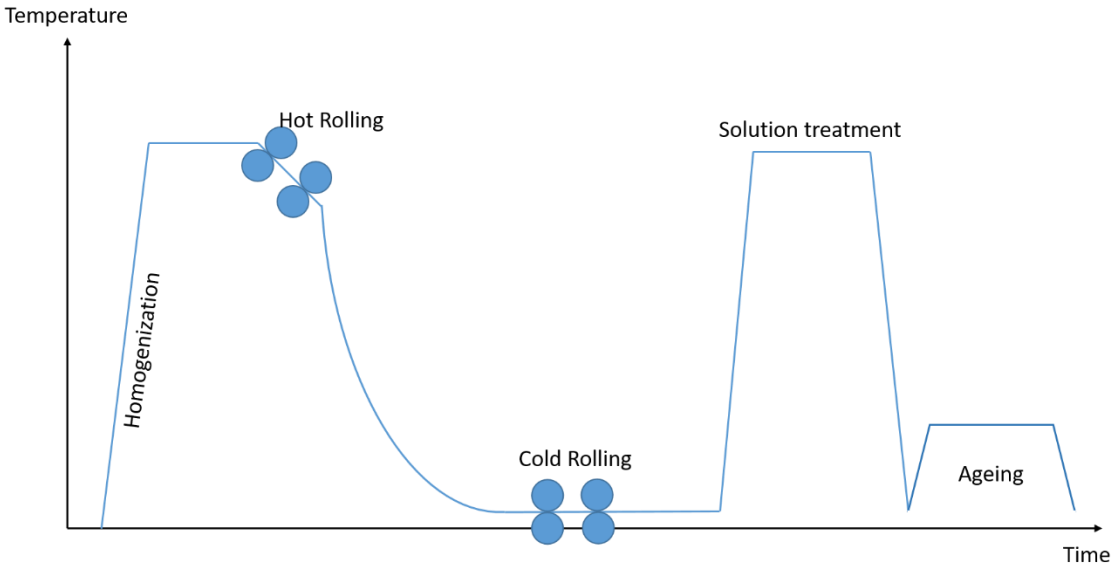

Figure 4.1: Schematic of a commercial aluminum-processing route

The aluminum sheets used for this experimental work are taken from the processing route directly after hot rolling and subsequent air-cooling with a thickness of approximately eight mm. Due to the elevated rolling temperatures, the microstructure consists of partially recrystallized areas as well as strongly deformed grains. Especially the surface of the sheet, which is touched by the rolls during processing, contains nearly 100 %-recrystallized grains. After cutting the hot rolled sheet in pieces of sizes about 9 x 6 mm (RD x TD) with the above-mentioned thickness, the “surface of interest”, which was either the “real” surface, touched by the rolls during processing or the through-thickness cross-section, is prepared (**Figure 4.2**). The cross-sections of the aluminum sheets provide different sections of shear deformation (T/4, T/2), which were analyzed concerning their difference in microstructural evolution. Grinding and polishing of the samples were done in multiple steps, resulting in a surface quality sufficient for EBSD observations. Finally the specimens are electrochemically polished, using the Struers LectroPol-5 polisher with the etchant “AlEP2”, which is composed of 80 % ethanol, 6 % perchloric acid and 14 % distilled water (Petzow 2006) for 15 s at about 7 °C with a voltage of 36 V. The final thickness of about 2.7 mm was arrived by milling the sample down from the backside of the surface.

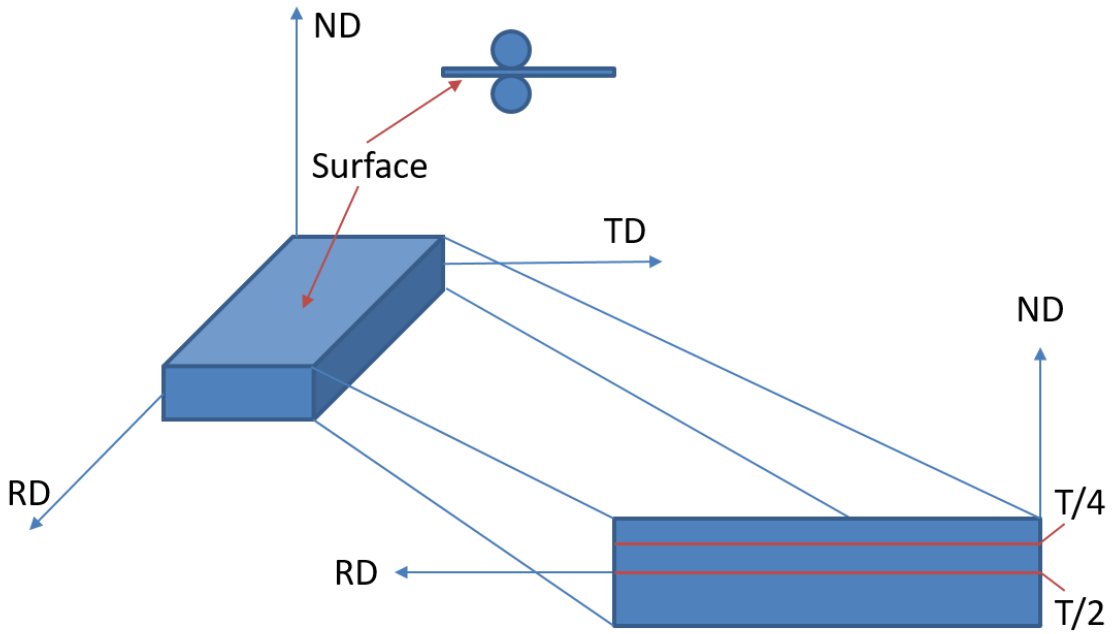

Figure 4.2: Schematic representation of the investigated "surfaces" of the aluminum sheets

4.2 SEM images and alloying elements

The first specimens were prepared and studied using the imaging modes of the SEM combined with EDXS to investigate the composition of the Al sheets as well as the precipitates' distribution. The specific aluminum alloy used in this master thesis is the AA 6016 provided by the company AMAG. Standard alloy composition is given in **Table 4.1**.

Table 4.1: Aluminum alloy AA 6016 standard composition range (wt %) (Engler and Hirsch 2002)

Alloy	Mg	Si	Cu	Fe	Mn	Zn	Ti
AA 6016	0.25-0.6	1.0-1.5	< 0.2	< 0.5	< 0.2	< 0.2	< 0.15

Comparing the AA 6016 and other 6xxx aluminum alloys, the stronger differences are in silicon and magnesium amount, which affects the particle distribution and therefore the total microstructural evolution during heating. The other alloying additions are in the typical range of 6xxx aluminum alloys.

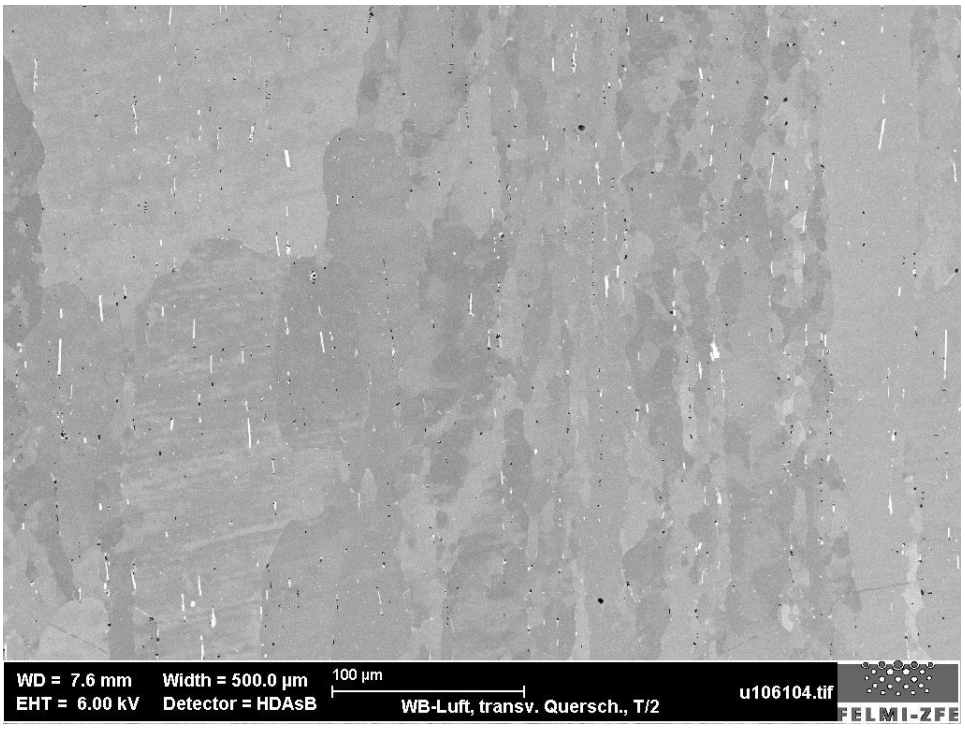

Figure 4.3: Microstructure of the cross section at T/2 before heating

Figure 4.3 shows the microstructure of the materials' cross-section at T/2 before heating. The various sizes of the grains result from partial recrystallization during hot rolling. The white rods represent a specific agglomeration of elements in this alloy, namely the AlFeSi-phases. The size of this phase lies in the range of a few microns. Going to higher magnifications, other phases could be observed. The main alloying elements Mg and Si form the Mg_2Si precipitates, which normally show sizes around 1 µm or below.

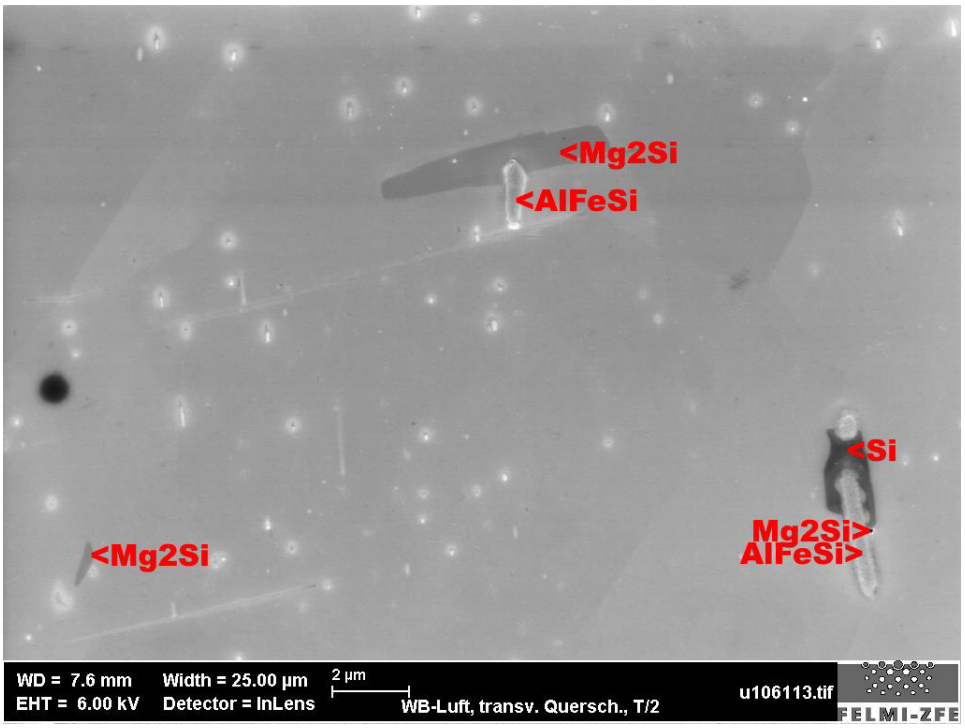

Figure 4.4: Precipitates in the AA 6016 alloy

In **Figure 4.4** the different precipitates of the AA 6016 alloy are shown at higher magnification. The image was obtained using the InLens detector, which shows higher phase contrast in this case compared to the BSE detector.

The Mg_2Si- and AlFeSi-particles are randomly distributed in the aluminum matrix. Beside these phases, the other alloying elements do not build up precipitates, but remain in solid solution at room temperature and often accumulate in small ranges at the precipitation sites of Mg_2Si and AlFeSi.

The white circles around points all over the image represent etchant artifacts and their imaging with the InLens detector and do not display any material features.

4.3 Surface sample / Grain growth

First heating experiments were performed on samples prepared for surface (not cross-section) investigations. Starting from RT, the temperature was increased in varying steps of °C, using the PID controller and performing an EBSD scan at each step. Because of scan durations may exceeding the time range of microstructural changes, the overview-maps made at room temperatures show a larger section of the surface in comparison to the *in situ* maps during heating. Furthermore, the scans before and after the heating experiment at RT include the EDX information, which is discussed in 4.7.

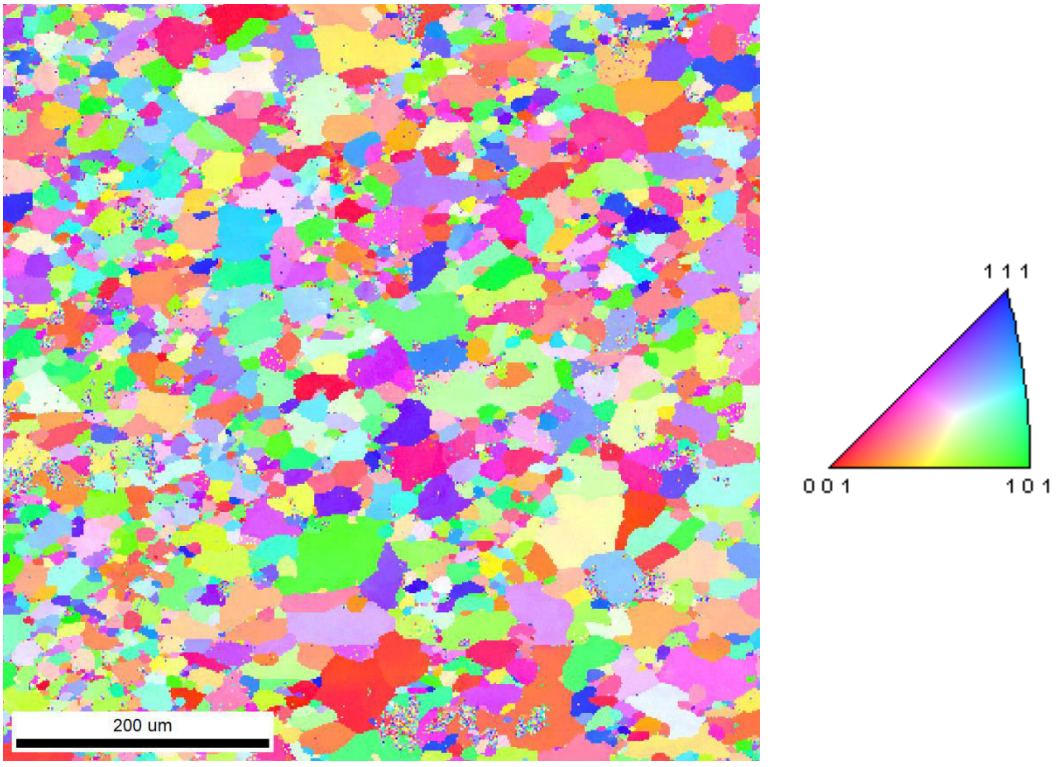

Figure 4.5: [001] - IPF overview-map of the surface of sample 1 with color-code legend; step-size: 1.5 µm

Figure 4.5 shows the 600 µm x 600 µm overview map of the surface of sample 1 recorded before heating, the crystal orientations are given by the color-coded legend. Since every IPF is plotted with the same direction of reference ([001]), color-code is the same for every map in this thesis.

Detailed examination of **Figure 4.5** shows some wrongly indexed data points in the IPF map. Unable to analyze the diffraction patterns in these areas due to contaminations, grain boundaries, scratches or other failures, the OIM software assigns to these pixels orientations,

which seem to be random. In this case, the software provides an iterative cleaning method, where orientations of these pixels are deduced from the orientations of their neighbors. But one has to be aware, that the wrongly indexed pixel could originate from the precipitates. In this case, the cleaning could cause minor errors in the grain sizes.

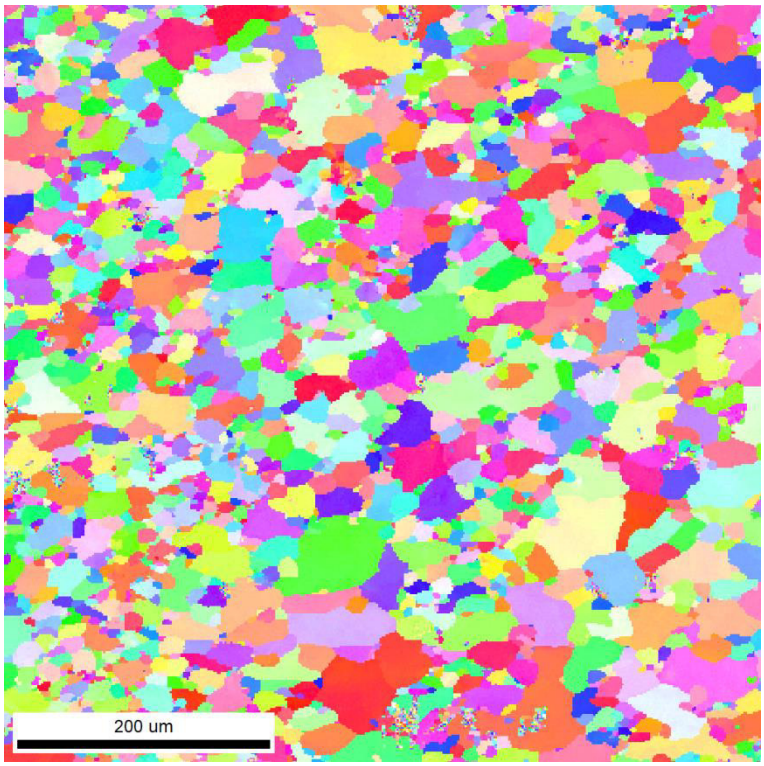

Figure 4.6: Cleaned [001] - inverse pole figure overview-map of the surface of sample 1; step-size: 1.5 µm

Figure 4.6 shows the IPF after cleaning and many of the originally wrongly indexed pixels have other, more suitable orientations, thus the cleaning routine seems to work properly and was used for all further IPF maps.

The microstructure of the aluminum sheet surface is dominated by recrystallized grains and does neither show any signs of elongated grains in rolling direction nor highly strained areas. The elevated temperatures during hot rolling led at the surface to complete recrystallization and strain-free grains after air-cooling.

The KAM map of the sample shown in **Figure 4.7** indicates no regions of high dislocation density. This strengthens the assumption that during heating the low amount of stored energy will be further reduced in form of grain growth and grain annihilation, starting at sites of higher energy.

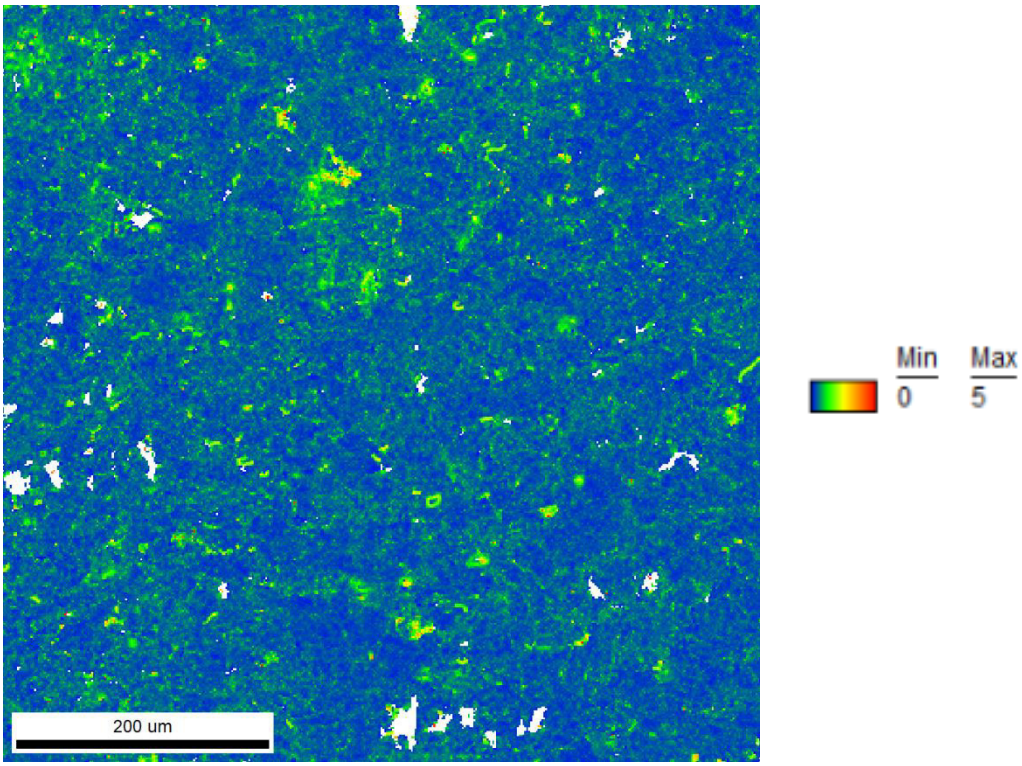

Figure 4.7: Kernel average misorientation map of sample 1 with color-code legend

During heating, a reduced area of size 200 µm x 200 µm was investigated. After reaching steady-state conditions concerning temperature increase and oscillations around the preset temperature, the sample had to be repositioned due to its thermal expansion.

The evolution of the microstructure during heating is depicted in **Figure 4.8**. Showing grains of different sizes, the smaller grains are annihilated by bigger ones as the temperature is increased and taking over the orientation of the big grains, but apart from that, no orientation changes could be observed during the experiment. The final temperature of the heat treatment was 550 °C, but because of highly unsatisfying image quality and non-essential changes in microstructure, the series of IPF images ends at 500 °C.

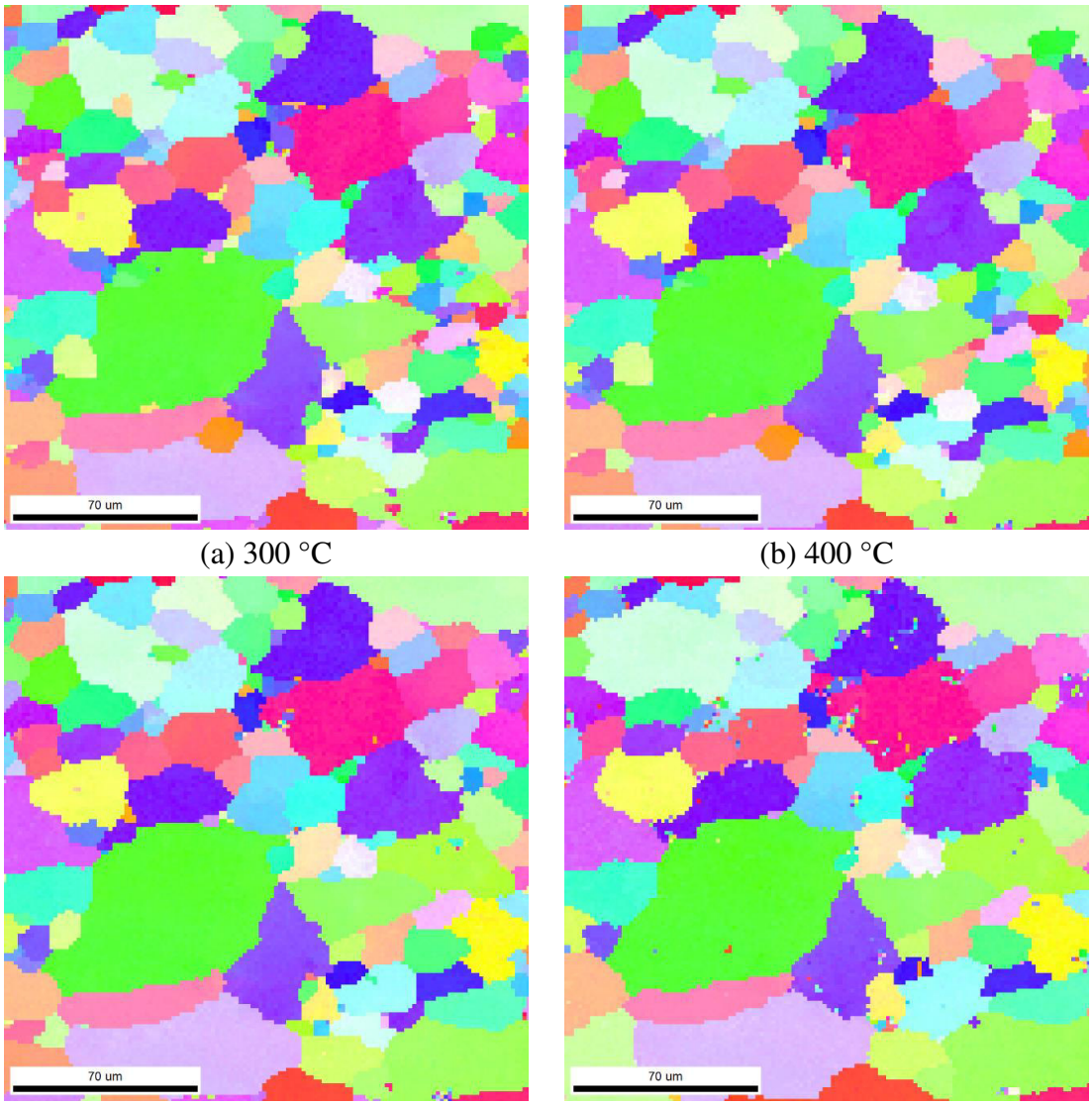

(a) 300 °C (b) 400 °C

(c) 450 °C (d) 500 °C

Figure 4.8: IPF maps of the surface of sample 1 at (a) 300 °C, (b) 400 °C, (c) 450 °C, (d) 500 °C; step-size: 1.5 µm

After slow cooling on air, the sample was repositioned and the same area as in **Figure 4.6** was scanned at room temperature. The sample again only showed grain growth, no other recrystallization mechanism seems to be activated, and the kernel average misorientation plot indicates slightly reduced residual stresses, as shown in **Figure 4.9**. The white areas in **Figure 4.9** (b) arise from indexing problems, also visible in numerous erroneous pixels in (a).

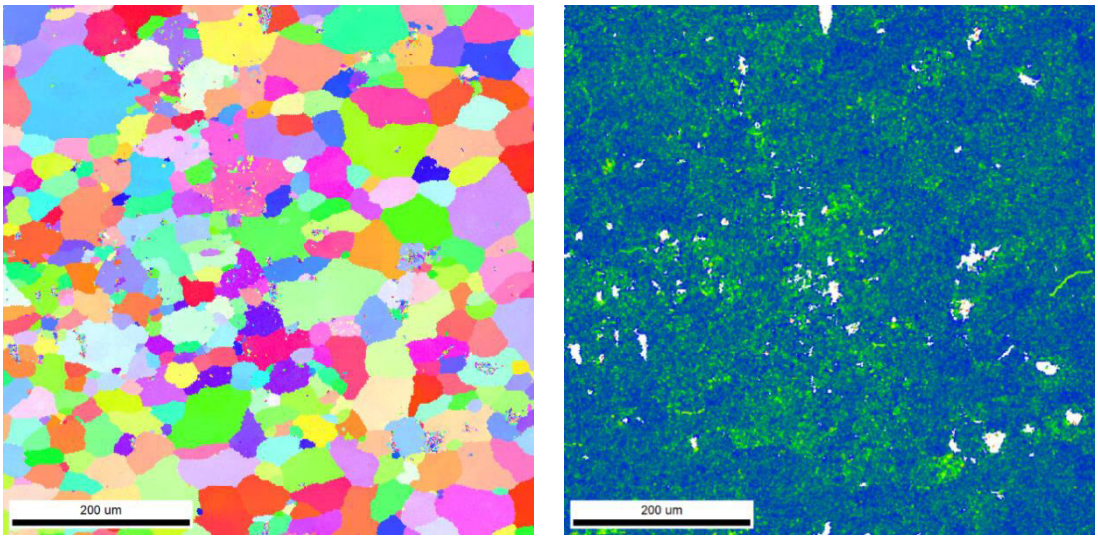

(a) (b)

Figure 4.9: (a) IPF and (b) KAM overview maps of the surface of sample 1 obtained after heating; step-size: 1.5 µm

The results gained from measurements at the specimen surface confirm the expected mechanisms behind the microstructural evolution. Since the investigated surface consisted only of recrystallized domains, the subsequent grain growth was a priori expected. The grain sizes at different stages of the heating experiment highlight the impact of temperature on the grain growth. Besides temperature, not only time and starting grain size influence the grain growth kinetics, but also the texture is associated with these microstructural changes. However, stated on the results of the surface sample, the focus was then put on cross-section investigations to get more information concerning microstructural evolution in the material during heat treatment.

4.4 Cross sections of samples: *In situ* recrystallization processes

4.4.1 Different cross section positions

During the deformation of metallic materials, a variety of mechanisms and processes takes place. Considering plane strain conditions like in usual rolling processes, the behavior of a material is in principle defined by its stacking fault energy (γ_{SFE}) and crystallography. The two main mechanisms of deformation in metals are slip and twinning, where higher γ_{SFE} enables cross slip and thus favors slip deformation. The slip systems of metals, defined by slip plane and slip direction, are a function of the crystal structure. Preferentially slip takes place in the most densely packed planes and directions.
The deformation process introduces different features of microstructural changes. Starting from single dislocations or dislocation tangles, these can move and form cells and subgrains, which can be aligned or have different orientations. It is often found that in (coarse-grained) materials grains subdivide into deformation and transition bands, especially when the material suffers from inhomogeneous stresses and instabilities inside the grains. The transition bands are narrow regions between the deformation bands. If planes inclined to the rolling direction undergo intense shear, the non-crystallographic shear bands occur, representing the plastic instability of the material (Humphreys and Hatherly 2004).

The sections of different shear-deformation in the hot rolled aluminum sheets mentioned in 4.1 are investigated on differences in their recrystallization behavior. Two specimens were prepared, representing the T/2-cross-section position (sample 2) and T/4-position (sample 3) respectively. The *in situ* EBSD scan procedure is similar to the one in 4.3. The duration at each preset temperature was about eight minutes, consisting of 6.8 min scan duration and the residual time necessary for repositioning of the specimen. The final temperature of 380 °C was chosen due to nearly 100 % recrystallization in the scanned area. This section shows only some representative results but the characteristic behavior of the Al sheet will be thoroughly discussed.

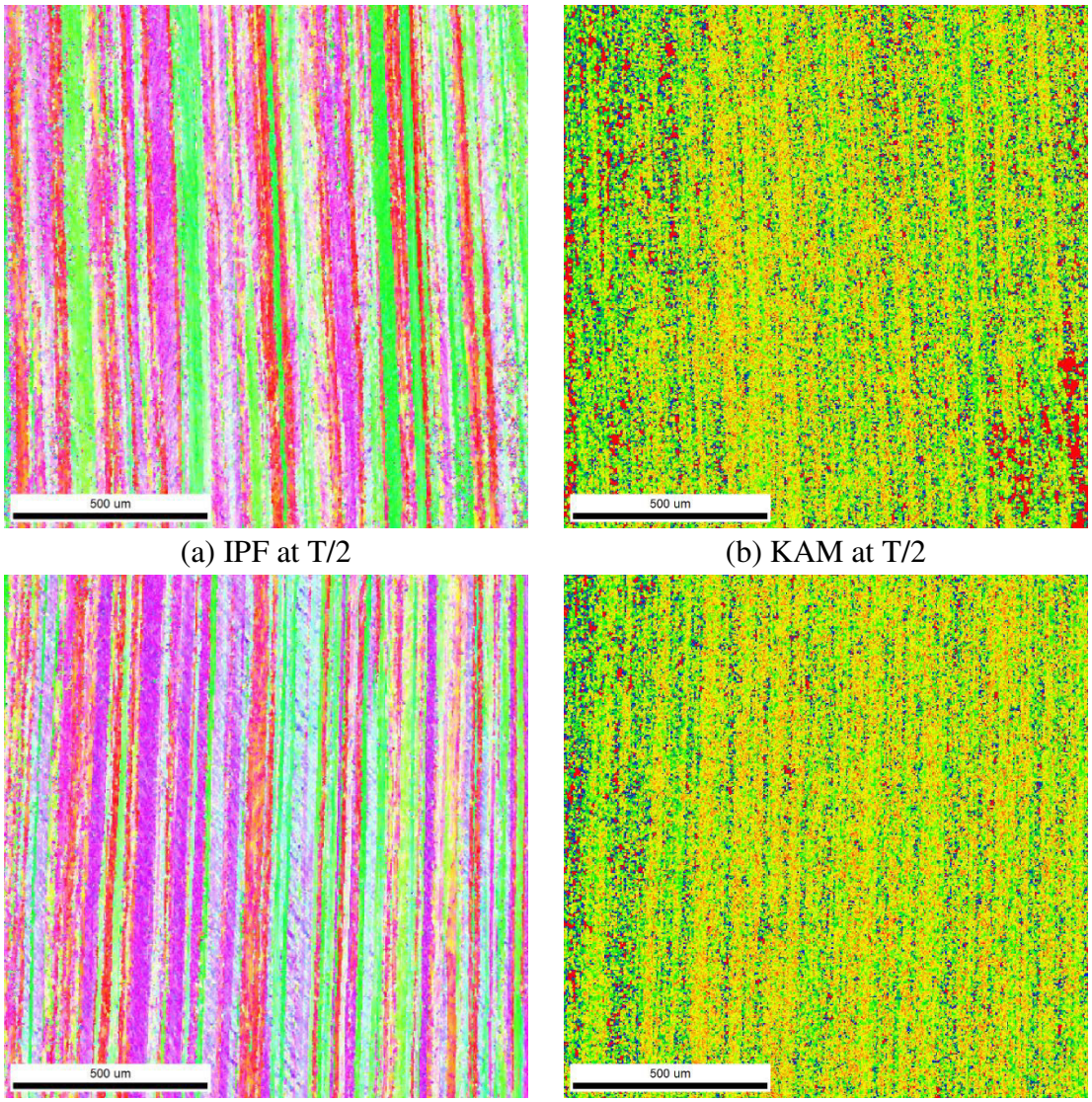

(a) IPF at T/2 (b) KAM at T/2

(c) IPF at T/4 (d) KAM at T/4

Figure 4.10: IPF and KAM maps of the microstructure of the aluminum sheets cross section (a) and (b) sample 2 at T/2, (c) and (d) sample 3 at T/4; step-size: 3 µm

Figure 4.10 shows the overview maps recorded at two different positions at the cross-section of the aluminum sheets, both indicating equivalent microstructural features, namely shear and deformation bands, which were also found at these positions in cold rolled Al sheets by Chen *et al.* (2013). The typical lamellar structure is induced by the alignment of large fractions of grain- and subgrain boundaries with the rolling direction.

The KAM map indicates regions of high residual stresses, being slightly enhanced at half of the sheet thickness. This negligible difference suggests the assumption that both areas will show similar behavior under heat treatment. Regions having high KAM values are usually the sites where recrystallization starts and regions with low dislocation densities are the most stable ones.

First recrystallization nuclei occurred at 350 °C for both specimens, capable of growing until meeting the nearest grain boundaries. The elongated grains in RD led to fast growth in this direction, whereas recrystallization in the lateral direction is restrained, which can be described by SIBM (2.3.1).

The mechanisms of oriented nucleation and oriented growth mentioned by Dillamore and Katoh (1974) and Molodov *et al.* (1998) determine the preferred orientations of recrystallized grains. Recrystallization nuclei formed somewhere in the transition bands due to a strong recovery and polygonization processes act as the basis for further microstructural evolution. Especially Cube nuclei resulting from substructures are responsible for the development of a strong Cube component in aluminum, which will be discussed in 4.5.2.
Following the evolution of the microstructure step-by-step (shown in the appendix), the first observed recrystallized areas have orientations close to <101> (green colored) in both samples. As time passes and the temperature is increased, other directions also appear in the maps, most prominent being the Cube orientation (red colored), whereas the formation of the <111> direction is suppressed.

The final microstructures of both specimens are presented in **Figure 4.11**. They show a variety of differently oriented grains, all of them still being elongated along RD, the <100> and <101> orientations are dominating, indicating the preferred orientations concerning oriented nucleation and oriented growth. Since only a few grains lie entirely in the scanned area, reliable grain size evaluation is impossible. To this aim, much larger areas would have to be mapped.

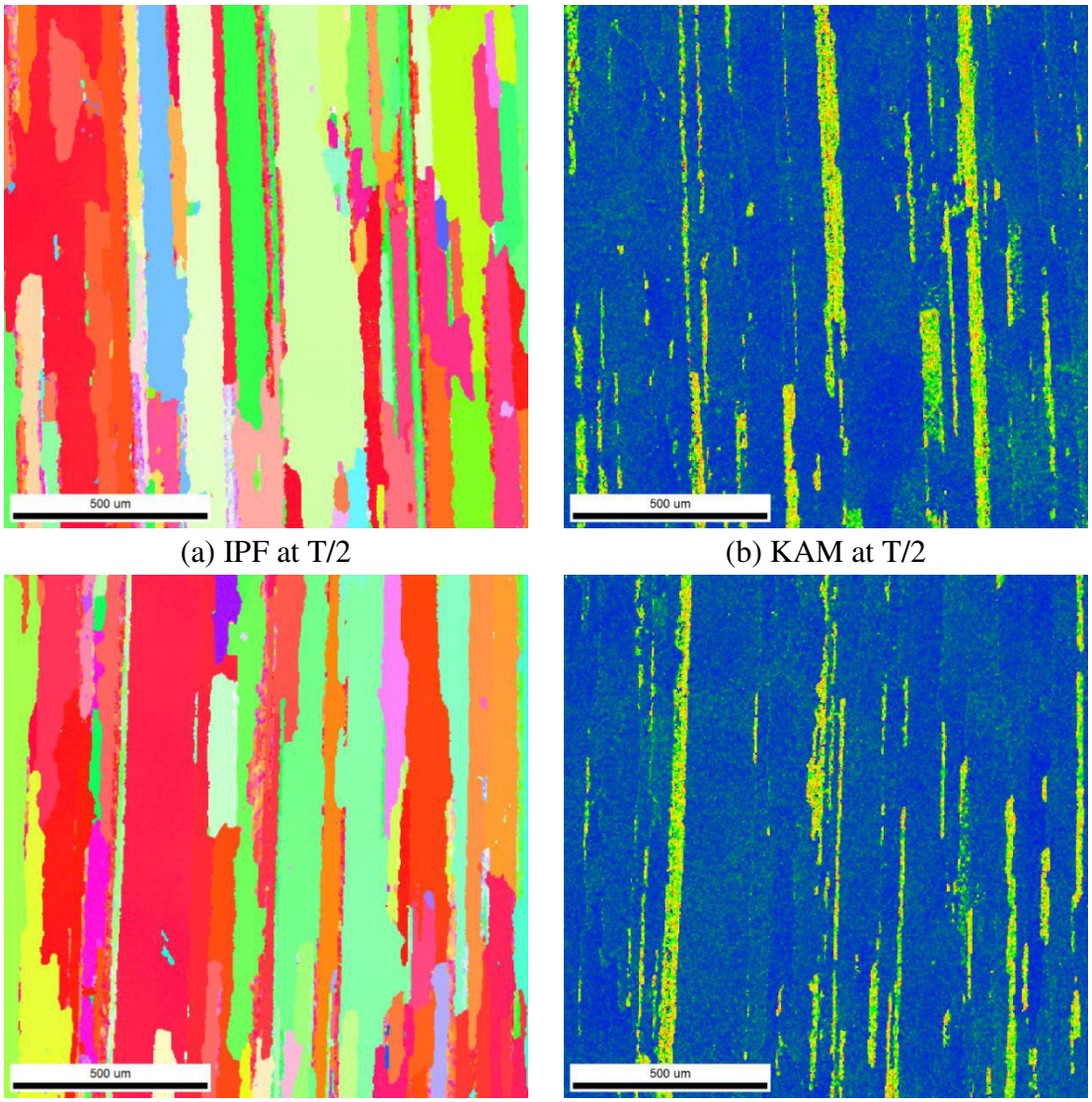

(a) IPF at T/2 (b) KAM at T/2

(c) IPF at T/4 (d) KAM at T/4

Figure 4.11: IPF and KAM maps of the microstructure recorded at the cross sections of the aluminum sheets after heating: (a) and (b) sample 2, (c) and (d) sample 3; step-size: 3 µm

Generally, the microstructures at the two different positions at the cross section showed the same evolution during the *in situ* EBSD measurements. Since also the results obtained from other heat treatment experiments were position independent, the position is considered to be irrelevant for the used aluminum hot rolled sheets. However, a generalization of this behavior is not recommended, as there are no standard characterization criteria for the sheets taken from hot rolling, which makes them incomparable and eventually individual concerning the microstructural evolution.

4.4.2 Constant temperature experiment

The two main factors governing the heat treatment are time and temperature. Since the evolution of the microstructure with rising temperature is shown in **Figure 4.10** and **Figure 4.11**, the following experiment depicts the changes in microstructure with time at constant temperature. Specimen 4, with an area mapped at the T/2 position of the cross-section, was heated up fast (approximately 3 min) to 325 °C and the temperature was held constant for about 14 hours. The choice of the temperature was based on the results of the cross-section measurements of the samples 2 and 3. Scan duration was 5.5 min, resulting in about 150 EBSD scans during the whole soaking time of the temperature.

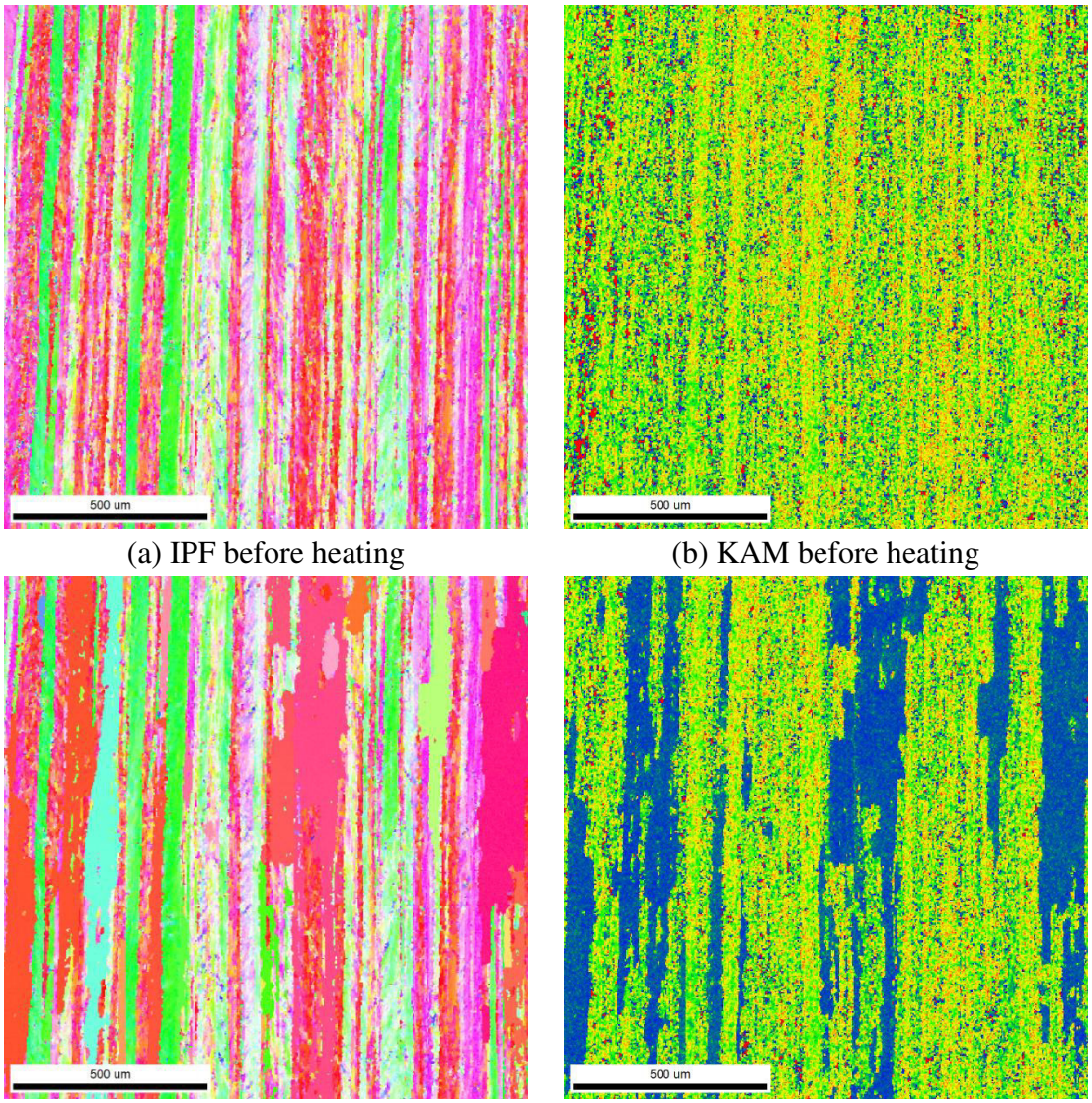

(a) IPF before heating (b) KAM before heating

(c) IPF after heating (d) KAM after heating

Figure 4.12: Overview IPF and KAM maps of the constant temperature recrystallization experiment with sample 4; (a) and (b) before heating, (c) and (d) after heating at RT; step-size: 3 µm

Evaluation of **Figure 4.12**, which displays the pre-post comparison of the EBSD measurements of sample 4, reveals large areas showing no indices of recrystallization or recovery. Starting again from the lamellar microstructure based on dislocations, deformation- and transition bands, only few recrystallization nuclei are built. Since the temperature is relatively low, the growth of the nuclei is very slow and hemmed. The final microstructure shows significant conformance in grain orientations with the initial microstructure, meaning some present orientations at the beginning grew at the expense of their vicinity.

Figure 4.13 shows relevant changes in the microstructure of the smaller, permanently scanned area. Initially, the temperature increase from RT up to 325 °C has no influences on the material. First signs of recrystallization can be observed after 314 min, best visible in the KAM map (**Figure 4.13** (b)). After obtaining the first nucleus, others quickly followed up within the next 90 min, all of them being capable of growing.
Generally, the growth rate and speed of boundary migration are very hard to analyze, since the duration of the EBSD scans is still by far too long to observe fast occurring changes. However comparing the final dimensions of the grains, some specific orientations show larger growth in the end. The orientations of the newly formed grains and former recrystallization nuclei seem to be randomly distributed at first sight, but a reconsideration of the final microstructure reveals a significant rise in orientations close to <001>, similar to the recrystallization of sample 2 and sample 3. Since the heat treatment is undergone by hot rolled sheets, the results can be compared to the ones of Bennett *et al.* (2010), who studied the influence of intermediate annealing (IA) on the final microstructure and texture properties. They also found an increased amount of Cube texture after IA, which had positive consequences on the overall texture banding in the alloys, as discussed in 4.5.

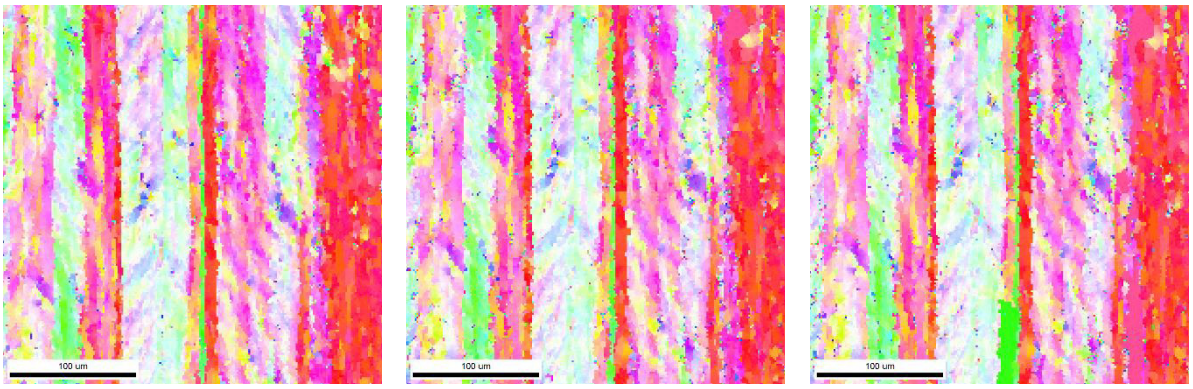

(a) RT (b) 314 min (c) 330 min

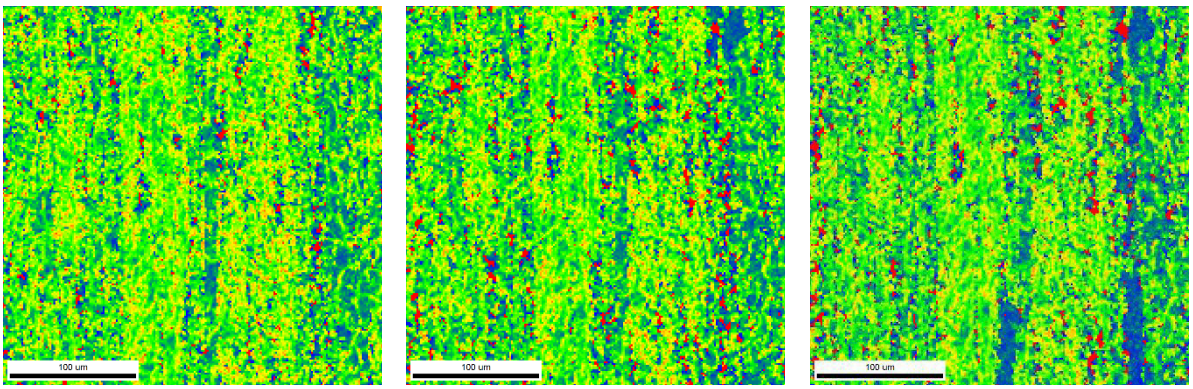

(a) RT (b) 314 min (c) 330 min

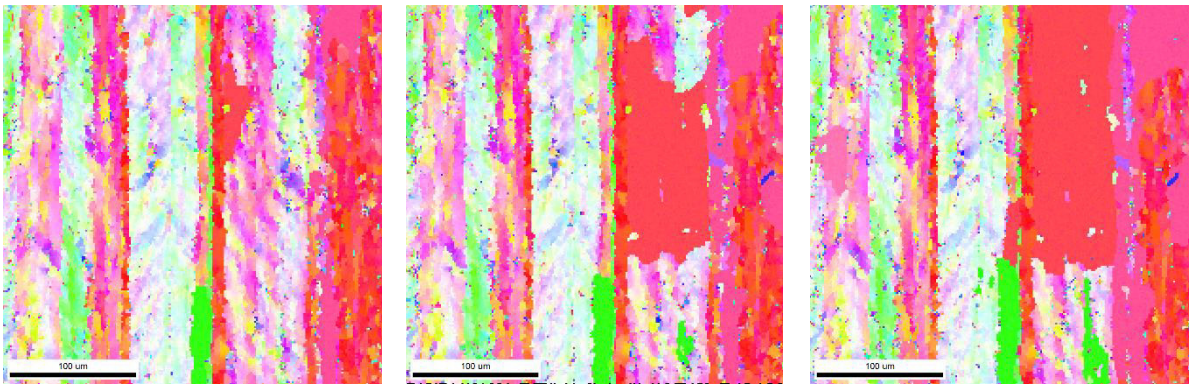

(d) 396 min (e) 578 min (f) 852 min

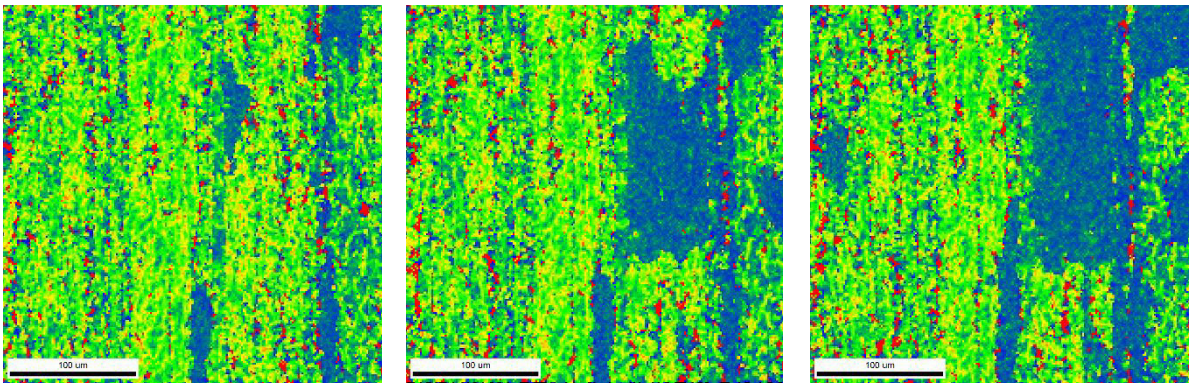

(d) 396 min (e) 578 min (f) 852 min

Figure 4.13: IPF and KAM maps of the microstructural evolution of sample 4; (b) – (f): T = 325°C; step-size: 1.5 µm

Since aluminum represents a metal with high stacking fault energy, the usual mechanism of energy reduction and inner stress relief is based on dislocation movement and formation of subgrains. However, starting from room temperature the KAM map shows no clear incidence of recovery at any point of experimental progress. One possible explanation for the absence of recovery in the *in situ* heating experiments is that recovery already occurred earlier during the deformation process, which would also account for the relatively low total dislocation density in the used Al sheet.
As Burger *et al.* (1995) showed for 5xxx alloys, the Mg content has influences on recovery issues during paint bakery cycles in automotive sheet production. Being present in the AA 6016 alloy along the side of Si and Fe, the stable particles of variant sizes can affect the mobility of dislocations and thus the microstructural evolution.

4.4.3 Partially recrystallized sample

Samples 2 to 4 showed heavily deformed microstructures after hot rolling. In this section, the sample no. 5 had partially recrystallized areas, representing some kind of mixture between the surface of sample 1 and all other samples so far.

The systematic evolution of the microstructure shown in **Figure 4.14**, resolves the expansion of the recrystallized areas with rising temperature. The elongated grains show a mixture of deformation and shear as well as recrystallization. Enhancing the temperature stepwise, first nuclei for recrystallized grains occurred at 400 °C. The grain, having an orientation close to <101>, is visible in the lower right corner of **Figure 4.14** (b), first grows along the rolling direction (vertical in the pictures), which denotes similar behavior to samples 2 and 3.

Since having relative strict lateral limitations based on the grain boundaries, the SIBM recrystallization behavior is obtained again. The 420 °C and 430 °C pictures show the converging of differently oriented grains and the further broadening of grains. Once the energy input based on temperature increase exceeds the limitations of SIBM, the grains are also capable of lateral growth.

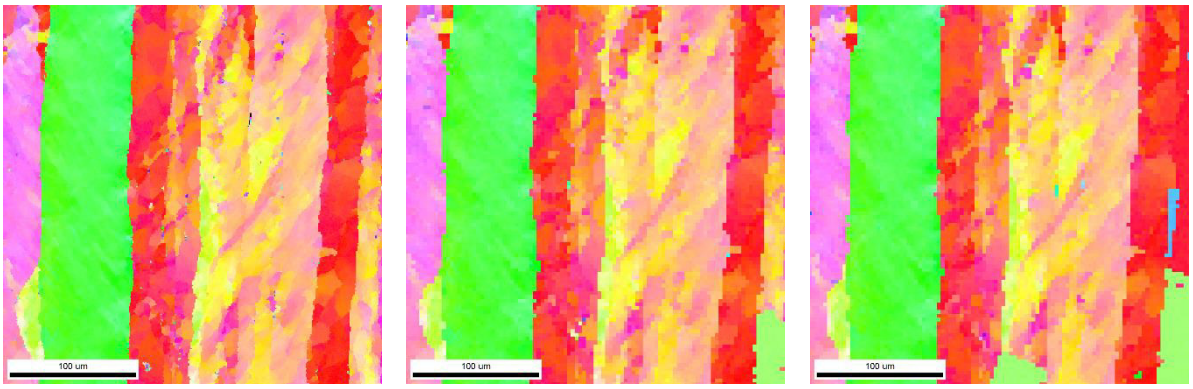

(a) RT (b) 400 °C (c) 410 °C

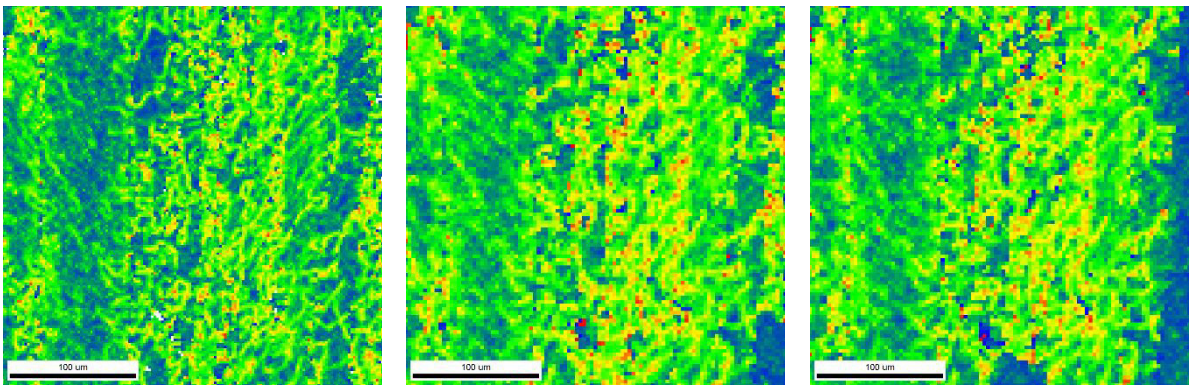

(a) RT (b) 400 °C (c) 410 °C

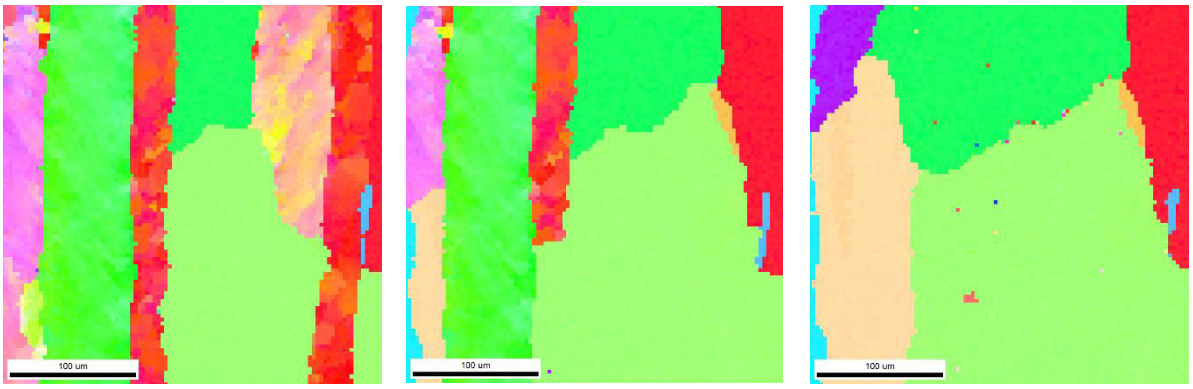

(d) 420 °C (e) 430 °C (f) 470 °C

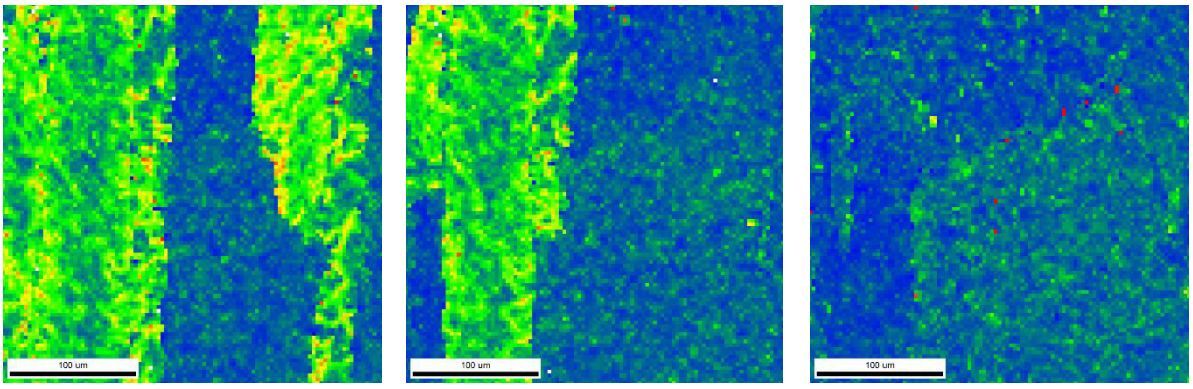

(d) 420 °C (e) 430 °C (f) 470 °C

Figure 4.14: Sample 5, cross section; IPF and KAM maps of the microstructural evolution of partially recrystallized sample; step-size: 2.5 µm

The final microstructure obtained at 470 °C displays sparse accordance to the grain orientations before the heat treatment. Since the area of the *in situ* measurement is very small, the orientations present in **Figure 4.14** (f) cannot be considered to be dominant. The overview IPF and KAM maps presented in the appendix show differing results. Opposite to the small area scanned during heating the evaluation of the orientations of the grains after heat treatment allows the conclusion that most of the grains retain the directions existing already in the as-deformed microstructure.

Another feature supposable in the overview IPF maps as well as **Figure 4.14** (a) is the angular relationship between the rolling direction and the boundaries of shear deformation. Bay *et al.* (1992) and Hurley and Humphreys (2003) showed on commercial purity aluminum and aluminum cold rolled sheet, that besides the major alignment of the grain boundaries along RD another direction at an angle of 40° to the RD is in favor. Especially for lower strains present after hot rolling, the derived assumptions seem permissible. Although validity is not proven, comparison with samples 2-4 confirms the assumptions.
The KAM maps show similar results as obtained from samples before. The recrystallized areas show an extreme drop in dislocation density and regions of high stored energy provide preferential sites for further recrystallization, which was already stated by Humphreys and Hatherly (2004).

The EBSD measurements on sample 5 were also used for the evaluation of the influence of the "grain tolerance angle" on the calculations in the TSL OIM software. Besides the IPF maps, the software also allows displaying auto grain maps, which are derived from calculations concerning the misorientations between neighboring grains. The grain tolerance angle (GTA) is the minimum necessary misorientation between neighboring points that they can be assigned to two different grains. **Figure 4.15** shows three different grain maps, using GTAs from 5° to 15°, which reveal a strong dependence of the average grain size on the GTA. No well-defined grain boundaries can be extracted from the IPF maps, thus it is difficult to choose an optimum GTA. Humphreys and Hatherly (2004) mentioned the difference between HABG and LAGB. While HAGB (> 15°) represent boundaries between two distinct grains, LAGB (< 15°) result from subgrains within one grain. However, representation of EBSD data with grain maps has to be treated with caution, since there is no general value for the GTA deducible.

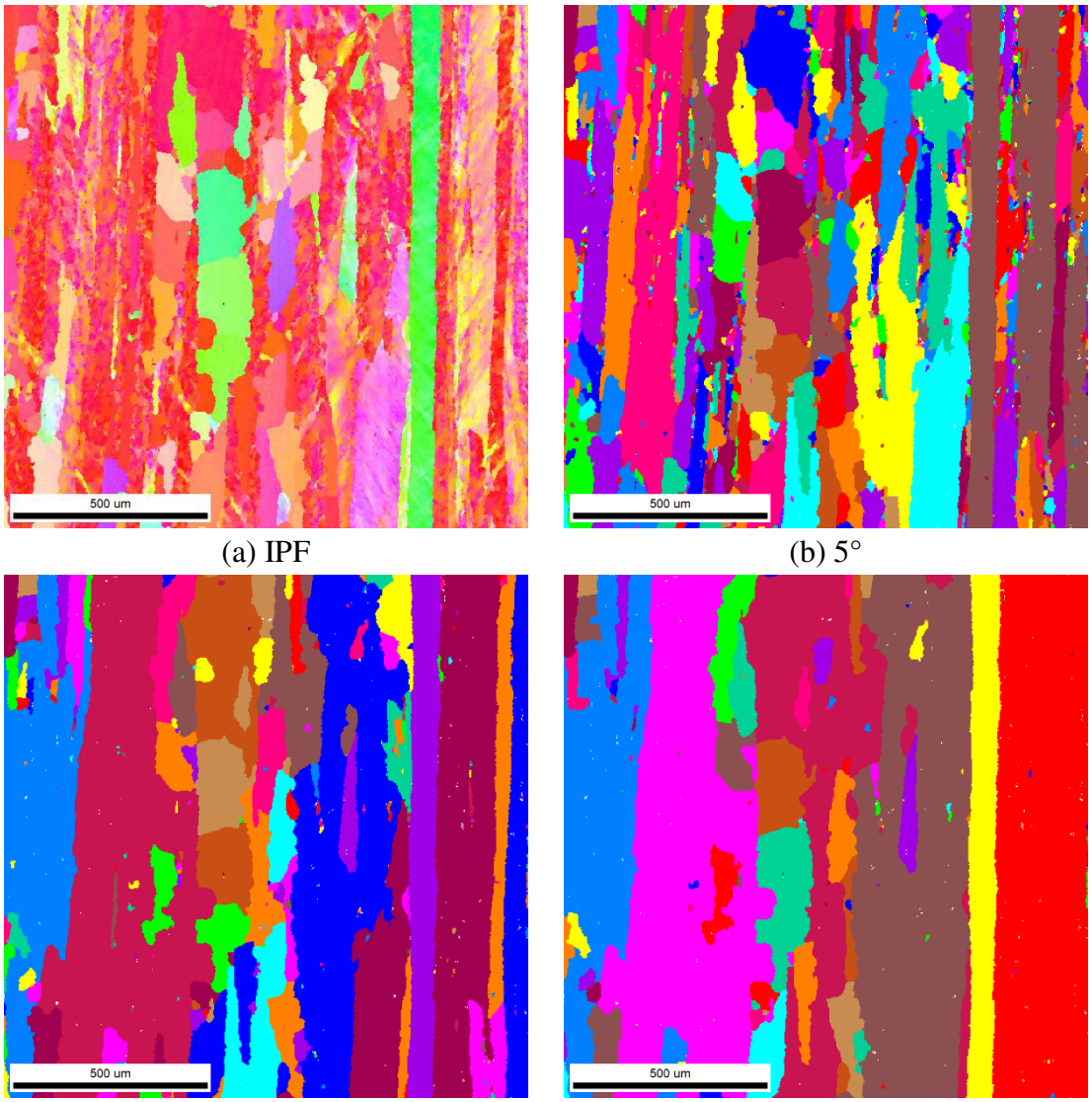

(a) IPF (b) 5°

(c) 10° (d) 15°

Figure 4.15: IPF and grain maps of sample 5 with different grain tolerance angles; (a) IPF, (b) 5° GTA, (c) 10° GTA and (d) 15° GTA

4.4.4 Different heat treatments: fast vs. slow heating

Based on the information gained in the former measurements, the focus was put on the influence of the heating rate on the changes in the microstructure. Samples 6 and 7, both showing heavily deformed grains, were cut out of the aluminum hot rolled sheet close to each other for consistent material properties. The time-temperature plot of the heat treatment as well as the as-deformed microstructures are given in **Figure 4.16**.

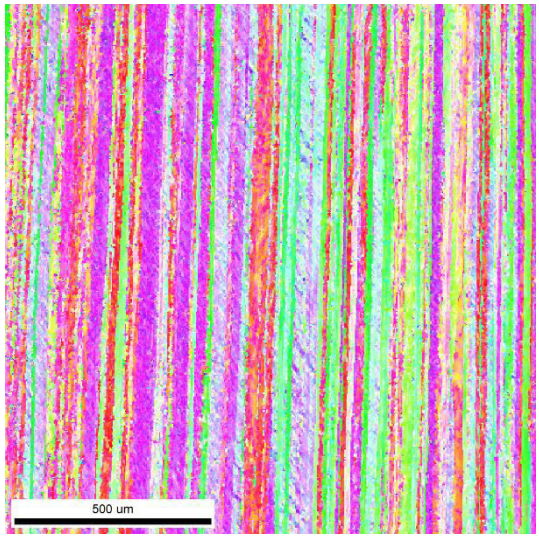

(a) IPF of sample 6 before heating

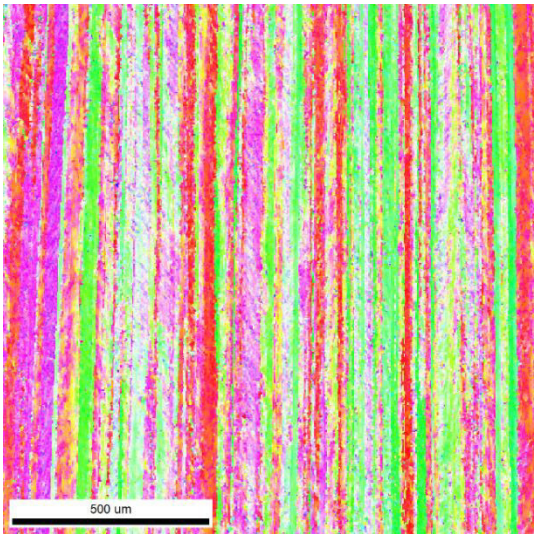

(b) IPF of sample 7 before heating

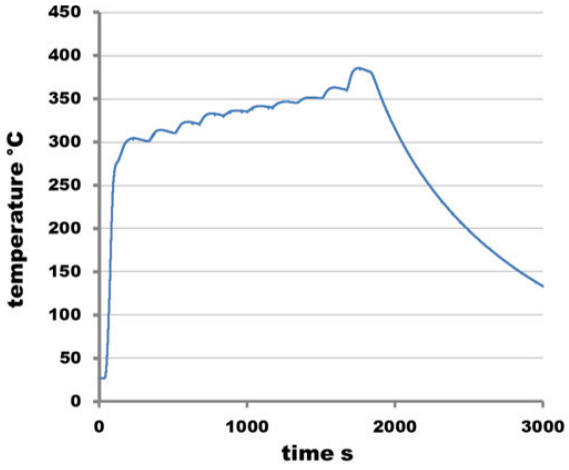

(a) heat treatment sample 6

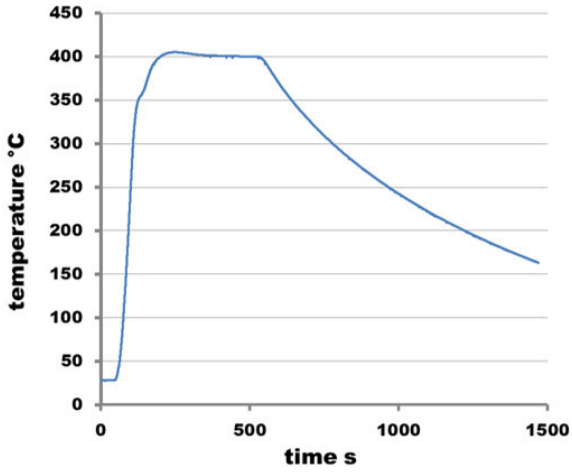

(b) heat treatment sample 7

Figure 4.16: Overview IPF maps and applied temperature profiles of (a) sample 6 and (b) sample 7; step-size: 3 µm

The results of this experiment totally match the conclusions of Wang *et al.* (2015). The slow, step-wise increase of the temperature on sample 6 results in a similar microstructure as obtained for the samples 2 to 5. Finding elongated grains in RD, the aspect ratio of the grains is far from 1 and because of the small scanned area gives poor statistics for grain diameter and

orientation evaluation. In contrast, the faster-heated sample 7 shows grains of shorter length in rolling direction. After repetition of this experiment, the same results were obtained, and thus the microstructures shown in **Figure 4.17** should be representative. The microstructures of both samples contain only a few unrecrystallized areas, meaning that the heat treatments, although being completely different in time duration, can for both samples be considered to have nearly finished at this point.

Humphreys and Hatherly (2004) explained the microstructural evolution during the heat treatment in general. As the temperature is increased, recrystallization nuclei are formed at different positions throughout the specimens. These nuclei, more likely growing into regions of heavily deformed microstructures, represent crystallites of low internal energy. Being separated by HAGB, both the nucleation rate and the growth rate depend on the temperature. Johnson, Mehl, Avrami, and Kolmogorov derived the first mathematical descriptions of these processes, which today is commonly known as JMAK-model. Although considering the change in nucleation rate with progressing time and amount of recrystallization, the assumption of randomly distributed nucleation sites causes unsatisfactory results.

In accordance to Somerday and Humphreys (2003), these results underline the importance of heating rate on the final microstructure. Fast heating activates more recrystallization nuclei at the same time, growing until abutting upon the grain boundary of a recrystallized neighbor. Since fewer recrystallization sites are formed during slower heating, the size of the respective crystallized grains is larger in comparison to those gained by fast heating.

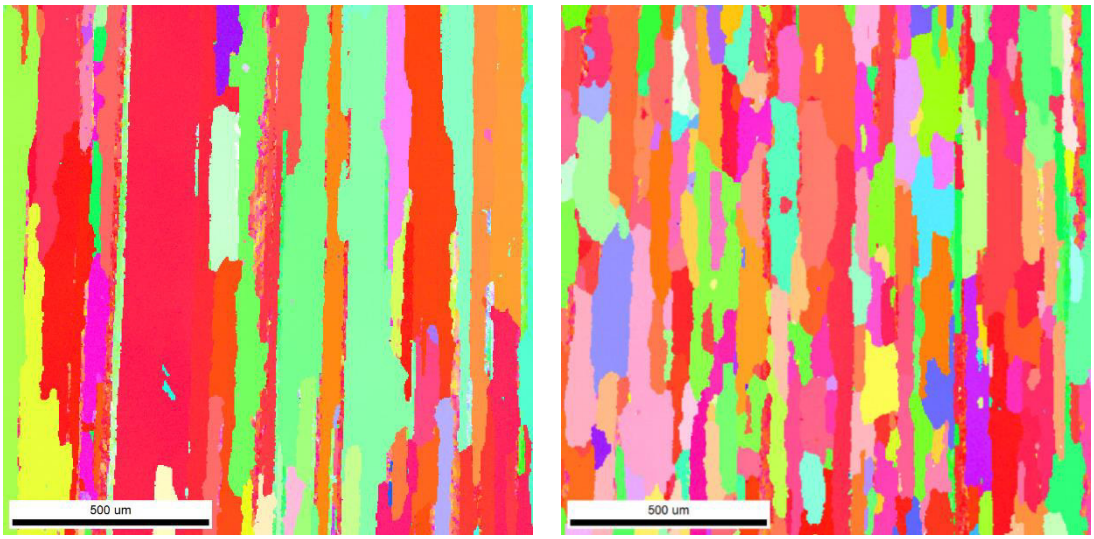

(a) (b)

Figure 4.17: Overview IPF maps after heating of (a) sample 6 and (b) sample 7; step-size: 3 µm

4.5 Texture Analysis

Texture banding in aluminum is one of the major microstructural effects during age hardening of the heat-treatable alloys. The fcc rolling texture, which developed during the rolling process, transforms during recrystallization and gives rise to new texture components. Affecting not only the final mechanical properties but also causing problems concerning the sheet materials plastic anisotropy, attention is focused increasingly on the control of texture throughout the entire processing.

4.5.1 General texture development in aluminum hot rolled sheets

The typical fcc rolling texture contains different orientations, most occurring Brass, Goss, Copper, and S textures (Hamad *et al* 2016), which are built due to preferential orientations of slip during deformation. The final texture after the heat treatment, most prominent components being Cube and R, results from the recrystallization process based on the mechanisms mentioned above.

Engler and Hirsch (2009) stated that the final texture is dominated by the fastest growing orientations, starting from many different oriented nuclei or in contrast by oriented nucleation, where the preferential formation of specific orientations defines the recrystallization texture.

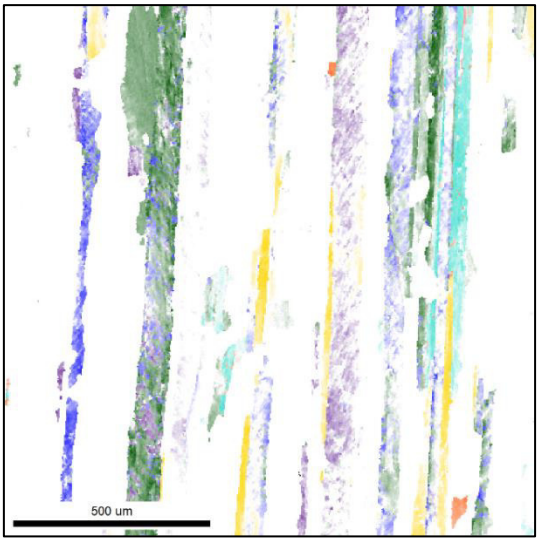

(a)

Orientation Euler Angles	Orientation {hk(i)l}<uv(t)w>	Min	Max	Total Fraction
(39.2, 65.9, 26.6)	(1 2 1)[1 -1 1]	0°	10°	0.000
(90.0, 35.3, 45.0)	(1 1 2)[-1 -1 1]	0°	10°	0.003
(56.8, 77.4, 26.6)	(2 4 1)[1 -1 2]	0°	10°	0.016
(56.8, 29.2, 63.4)	(2 1 4)[-1 -2 1]	0°	10°	0.028
(27.0, 64.1, 14.0)	(1 4 2)[2 -1 1]	0°	10°	0.006
(123.2, 29.2, 26.6)	(1 2 4)[-2 -1 1]	0°	10°	0.074
(64.9, 74.5, 33.7)	(2 3 1)[1 -2 4]	0°	10°	0.000
(46.9, 36.7, 63.4)	(2 1 3)[-1 -4 2]	0°	10°	0.005
(15.0, 57.7, 18.4)	(1 3 2)[4 -2 1]	0°	10°	0.031
(64.9, 105.5, 56.3)	(3 2 -1)[2 -1 4]	0°	10°	0.014
(52.9, 74.5, 33.7)	(2 3 1)[3 -4 6]	0°	10°	0.005
(59.0, 36.7, 63.4)	(2 1 3)[-3 -6 4]	0°	10°	0.029
(27.0, 57.7, 18.4)	(1 3 2)[6 -4 3]	0°	10°	0.007
(121.0, 36.7, 26.6)	(1 2 3)[-6 -3 4]	0°	10°	0.024
(270.0, 27.2, 45.0)	(4 4 11)[11 11 -8]	0°	10°	0.006
(270.0, 152.8, 225.0)	(-4 -4 -11)[11 11 -8]	0°	10°	0.024
(54.7, 90.0, 45.0)	(1 1 0)[1 -1 2]	0°	10°	0.020
(35.3, 45.0, 0.0)	(0 1 1)[2 -1 1]	0°	10°	0.019
(0.0, 45.0, 90.0)	(1 0 1)[0 -1 0]	0°	10°	0.000

(b)

Figure 4.18: (a) fcc rolling texture components map of a cross-section measurement before heat treatment and (b) color code legend including partition fractions

Figure 4.18 shows the fcc rolling texture components based on the EBSD measurement of a partially recrystallized cross-section sample (T/4). The Euler angles and orientations in the color code legend do not exactly coincide with the information listed in **Table 2.1**, which is due to calculations in the TSL OIM software also considering small deviations from the perfect standard orientations.

However, color orange represents a Copper component, red Goss and yellow as well as cyan both stand for Brass. The S component is split into three parts and therefore has assigned colors green, blue and violet. Hence, the as-deformed microstructure consists at least of some of the expected components.

The recrystallization component map of the same sample used for the representation of the rolling components after heating is shown in **Figure 4.19**.

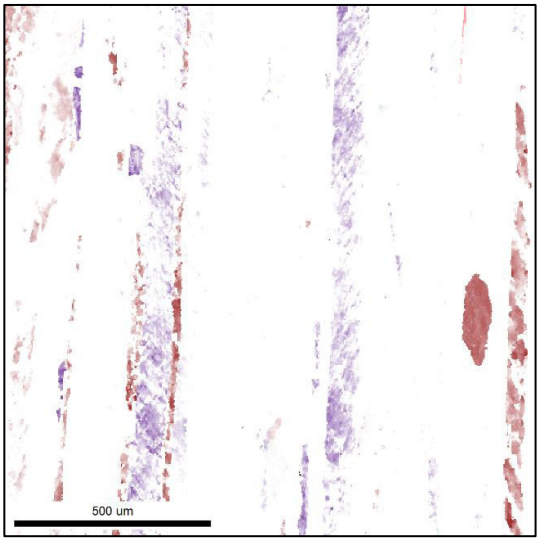

Orientation Euler Angles	Orientation {hk(i)l}<uv(t)w>	Min	Max	Total Fraction
(0.0, 0.0, 0.0)	(0 0 1)[1 0 0]	0°	10°	0.065
(54.7, 45.0, 0.0)	(0 1 1)[1 -1 1]	0°	10°	0.000
(46.5, 18.4, 0.0)	(0 1 3)[3 -3 1]	0°	10°	0.002
(15.0, 57.7, 18.4)	(1 3 2)[4 -2 1]	0°	10°	0.082

(a) (b)

Figure 4.19: (a) fcc recrystallization texture components map of a cross-section measurement and (b) color code legend including partition fractions

Depicting only weak recrystallization texture, the representative components namely Cube (red), R (violet) and Q (beige) are present. Similar to the S rolling texture, the R component is an indication for *in situ* recrystallization and SIBM (Hirsch and Lücke 1985), most frequently obtained in Fe-containing alloys. R orientations usually nucleate from existing orientations at grain boundaries and show the deviations from original S orientation due to preferential growth or nucleation effects (Hirsch and Al-Samman 2013).

The Q orientation is normally assigned to the existence of shear bands, more common in cold rolled Al sheets. However, small amounts of Q texture components can also be found in the hot rolled sheets used in this thesis.

At least to mention is the influence of particle-stimulated nucleation on the final texture. Not present in the recrystallization textures of the used aluminum samples the PSN mechanism typically results in preferred P orientation. Detailed discussion on this topic is provided in section 4.7 (Engler and Hirsch 2009).

4.5.2 Cube texture component

Besides the overall rolling and recrystallization texture mentioned above, one specific component gained center stage in the last decades. The control of Cube component plays a key role in designing and developing new technologies. Forming processes such as deep drawing crucially depend on the materials anisotropy and earing values. Since both are directly related to the recrystallization texture, which is in general dominated by the Cube component, the impacts on drawability are tremendous.
In addition to the plastic anisotropy another phenomenon, commonly denoted as "*ridging*" or "*roping*", is associated with the presence of Cube bands. Indicated by the presence of uneven sheet surfaces after forming, roping does not only limit the sheet formability but also affects the final sheet quality even after painting. Because of these undesirable effects, research departments work intensively on methods in Cube texture control and prediction. One attempt therefor is the reduction of Cube oriented grains in the hot rolled sheets, resulting in higher quality of the later cold rolled material with low amounts of Cube component.

This section outlines some characteristic results gained on Cube texture analysis of the heat treated hot rolled Al sheets. Based on the results of experiments on samples 2-7, the texture maps depict the changes in the amount of Cube component present.

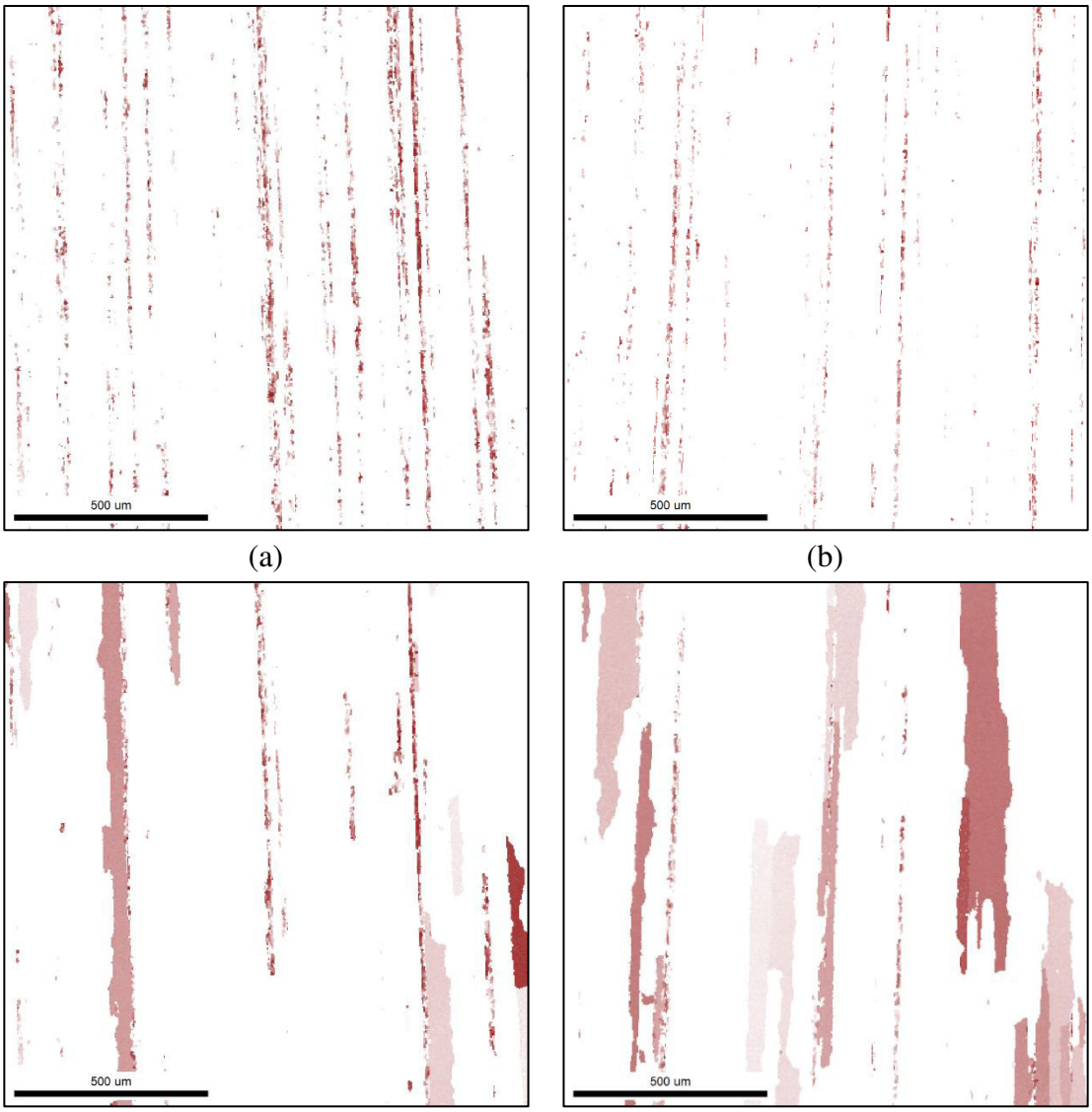

Figure 4.20: Cube component maps of (a) sample 2 and (b) sample 3 before and after heating

Figure 4.20 shows the evolution of Cube components during the *in situ* heating experiment of samples 2 and 3. The Cube bands present in the as-deformed microstructure in the upper images of (a) and (b) result either from transition bands formed from unstable orientations or are grains with suppressed Cube character. The subsequent growth favors Cube oriented grains, because of their high symmetry and advantageous orientation relations to the neighboring points (Engler and Hirsch 2009). As for example De La Chapelle (2001) mentioned, that Cube nuclei preferably grow into neighboring S directions, where the boundaries give a 40° <111> relationship, which is commonly regarded to show the highest growth rate in aluminum.

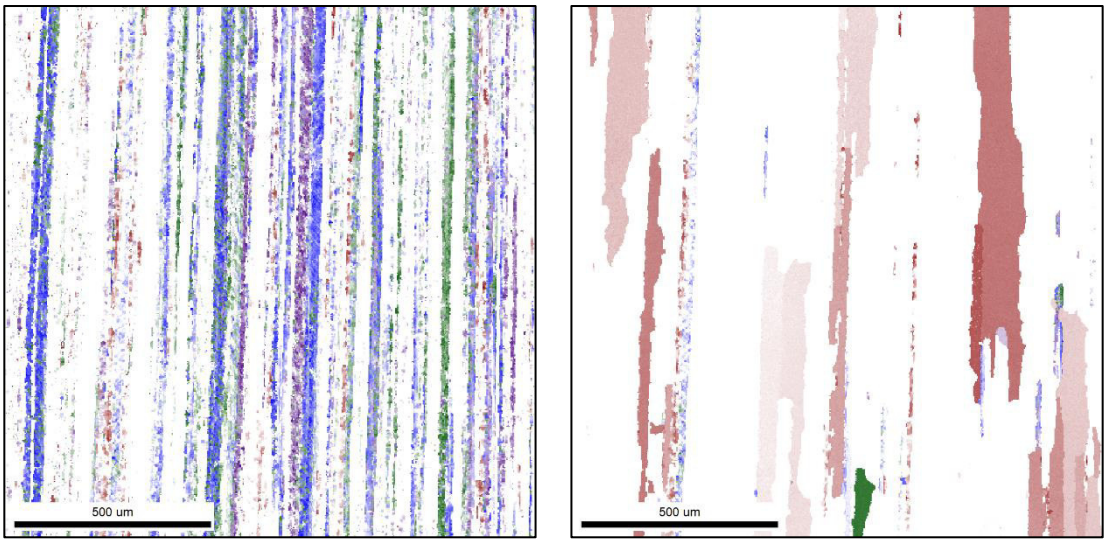

(a) (b)

Figure 4.21: Cube (red) and S (other colors) component maps of sample 3, (a) before heating and (b) after heating

Figure 4.21 displays the Cube and S oriented areas of sample 3 before and after heating. While S components (blue, green and violet) are significantly decreased, the deformed Cube grains grew partially on the expose of them. Especially areas with only small Cube nuclei show high expansion rates in S oriented grains.

The final amount of the Cube component is significantly increased, which is depicted in the lower images of **Figure 4.20** (a) and (b). Although this meets the expectations, the primarily pronounced goal of Cube component reduction is not achieved.

Evaluation of sample 4 is not undertaken since only small parts of the surface of the sample showed recrystallization. However, the result showed a minimal reduction of the total area fraction of Cube oriented grains.

Considering only the results of sample 4, a generalization of this reduction in Cube component is hasty, especially when comparing to results of the samples 2 and 3. Confirmation followed by the analysis of sample 5, with the results depicted in **Figure 4.22**. The Cube amount is significantly reduced after the heat treatment, total fractions occupied being 14.9 % before and 4.5 % afterward. Especially the distribution and size of Cube grains improved, since the elongated Cube oriented grains at transition bands disappeared.

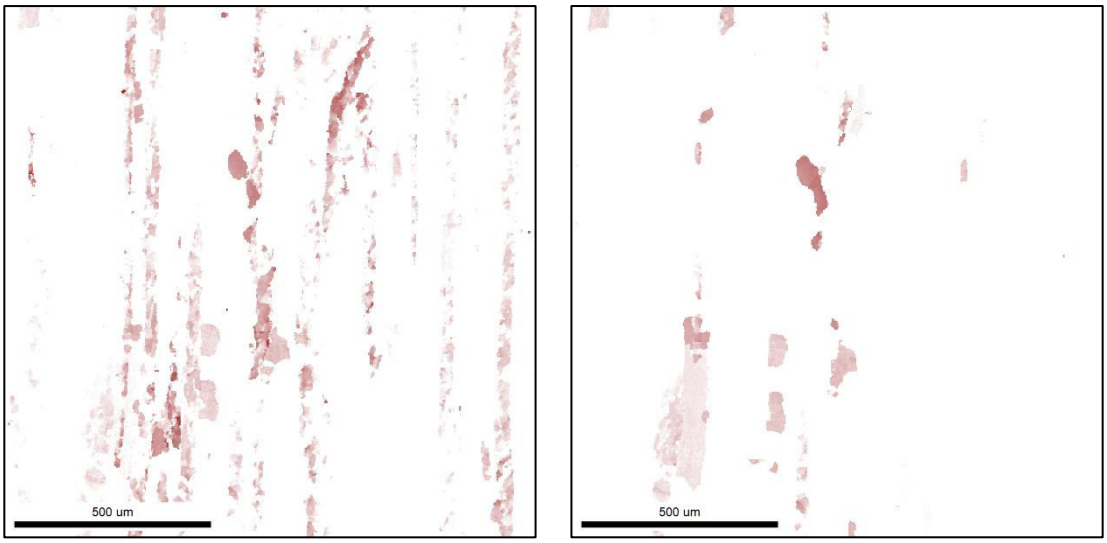

(a) (b)

Figure 4.22: Cube component map of sample 5 (a) before heating and (b) after heating

Finally, **Figure 4.23** shows the Cube texture evolution of samples 6 and 7. As already mentioned above, the different heat treatments led to completely different grain dimensions in the final microstructure, which is very similar to the Cube texture components. Although the fast heated sample 7 shows an increased Cube component, the absolute partition fraction is definitely lower than the one of the slower heated sample 6. This again meets the results of Wang *et al.* (2015), who showed that Cube texture more likely appears in the slowly heated sample.

The influence of Cube grains and their dimension on the final roping effect were discussed by Bennett *et al.* (2010). Their experiments on intermediate annealing of Al sheets between the hot and cold rolling process resulted in improved resistance of intermediately annealed sheets to roping. They attributed this behavior to the presence of a combination of small and coarse grains in the annealed sheets, which, although showing stronger Cube texture than the untreated sheets, resulted in reduced banding of the Cube components.

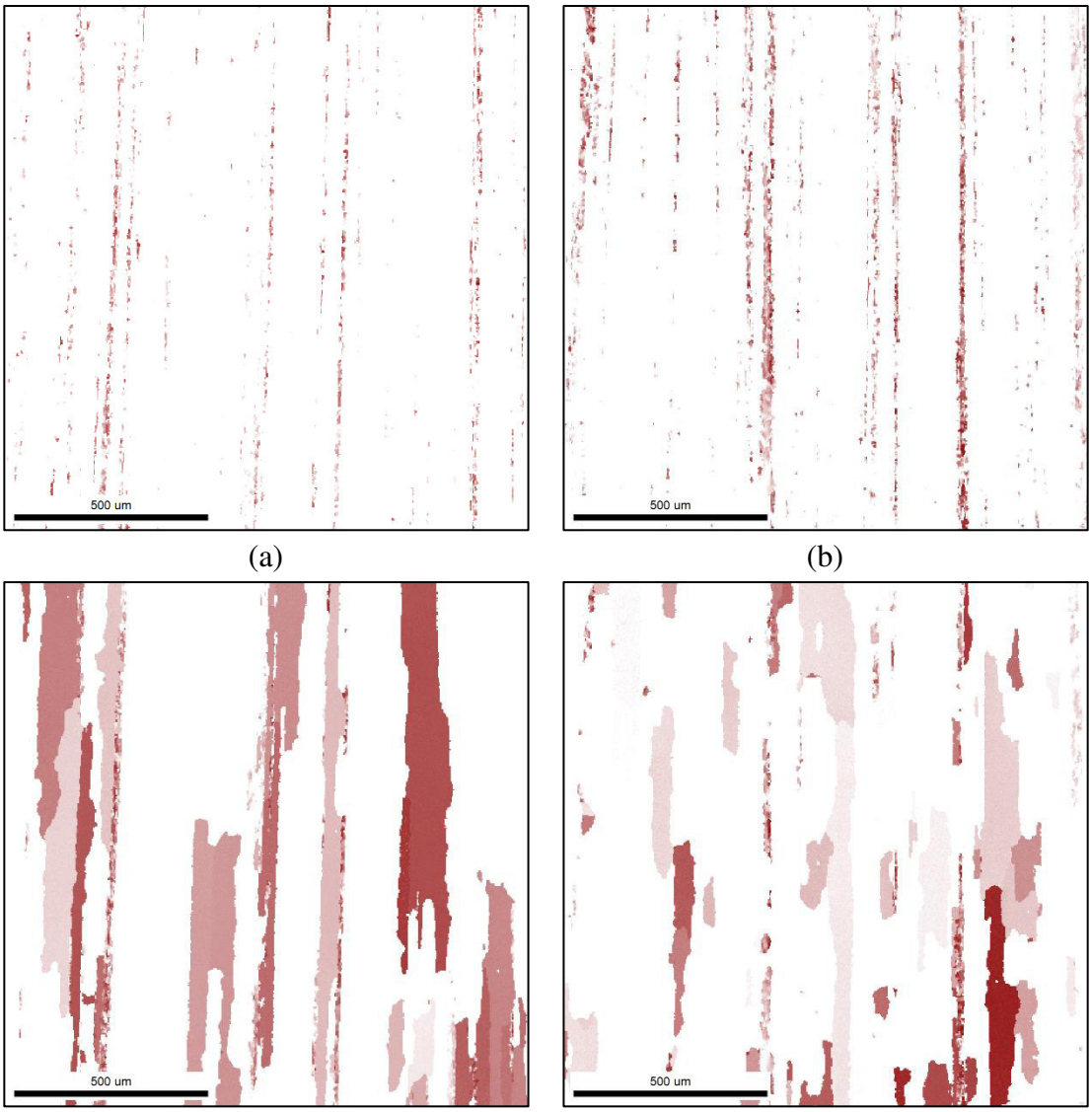

Figure 4.23: Cube component maps of (a) sample 6 and (b) sample 7 before and after heating

Concluding from the results of Cube texture analysis, although the *in situ* heat treatment did not show a reduction in the Cube oriented partition fraction itself for all samples, it has been shown that in case of intermediately annealed sheets the adverse effects of Cube oriented grains are strongly reduced. Assigning high heating rates to the IA heat treatments should improve the microstructures further concerning the roping effect. Clarifications are needed concerning the reduction of the Cube component in partially recrystallized samples 4 and 5. Since the analyzed areas were small, repetition of the experiments on bigger surfaces is necessary to get statistically more meaningful results. However, if sheets containing partially recrystallized areas from hot rolling trend to show a reduction in Cube texture and improved grain ratio distributions concerning roping, the focus should be put on the mechanisms behind this reduction and on the comparison with heavily deformed sheets.

4.6 Bulk behavior

Since EBSD measurements only provide data concerning the surface of the samples (to a depth of around 50 -100 nm), bulk measurements can reveal different effects. Especially during heat treatment of bulk specimens, surface effects, especially due to surface tension, cannot a priori be neglected. To extend the information of microstructural evolution also into the field of bulk behavior, sample 6 was investigated below the original surface at three different positions. The first bulk measurement scan was performed 100 microns below the original surface, after grinding and polishing down to the desired depths. Afterwards, scans on the positions at ¼ and ½ of the specimens' thickness accomplished the investigations.

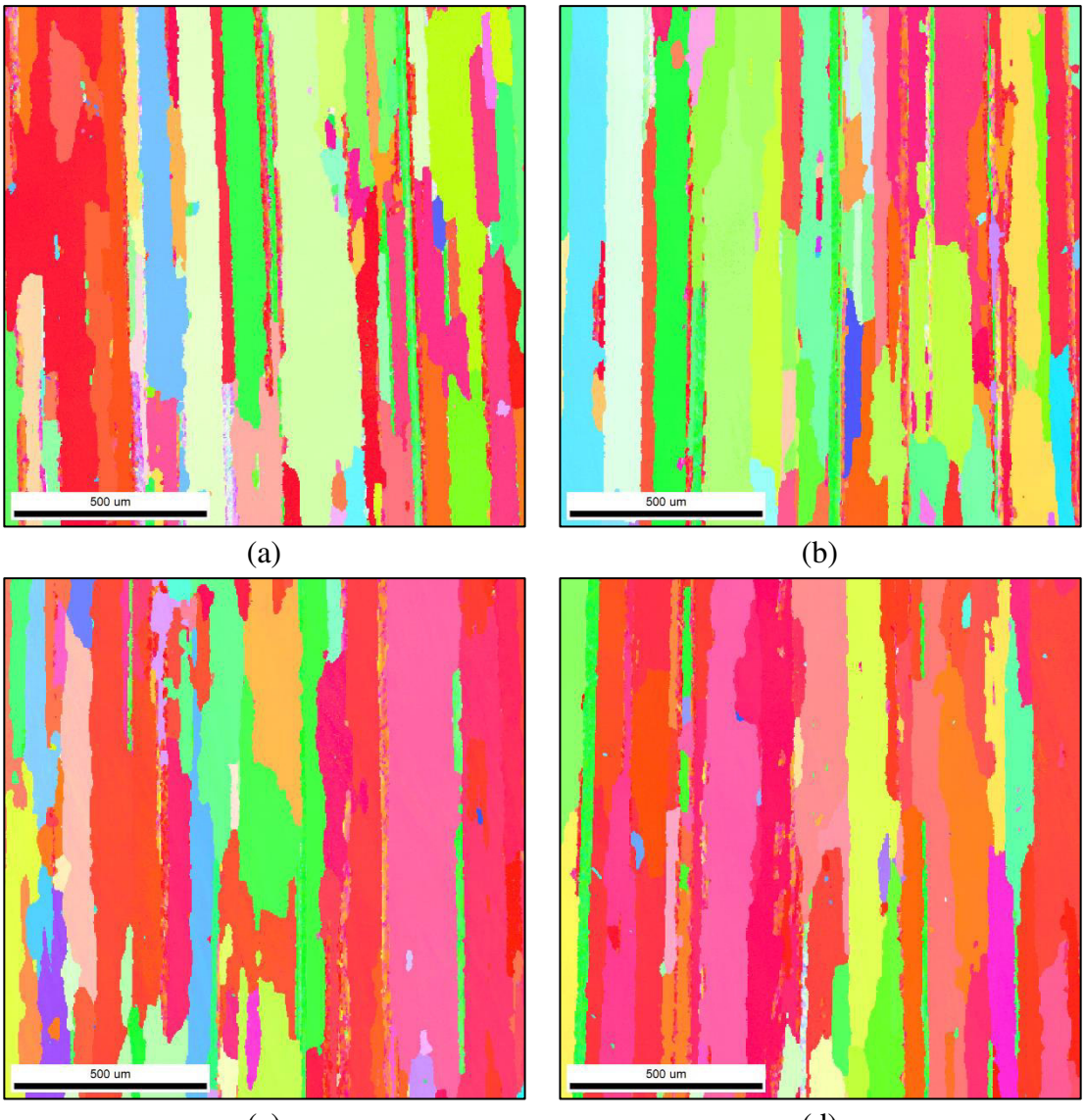

Figure 4.24: Bulk IPF maps of sample 6; (a) original surface, (b) -100 µm, (c) - 1/4 of specimen's thickness and (d) at 1/2 of specimen's thickness; step-size: 3 µm

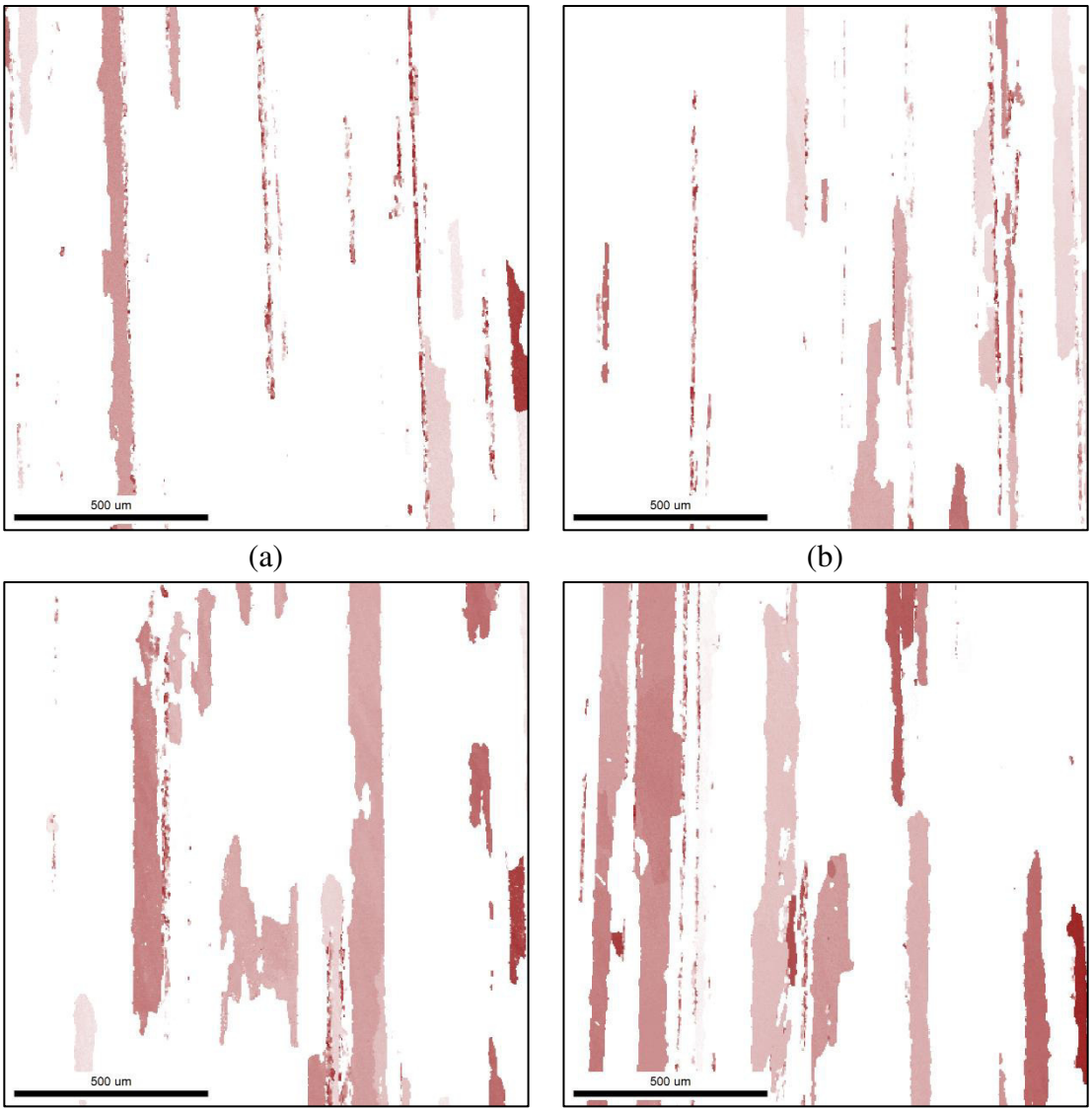

Figure 4.25: Cube component maps of the bulk measurements of sample 6; (a) original surface, (b) -100 µm, (c) - 1/4 of specimen's thickness and (d) at 1/2 of specimen's thickness

Figure 4.24 depicts the differences in microstructure within the bulk specimen. Comparing all IPF maps, no drastic changes are observable. The elongation of the grains is similar throughout the sample and the grains aspect ratios seem comparable for all four positions.

The orientations of the grains seem statistically distributed at first sight, but texture analysis shows increasing amounts of the Cube orientation with an increasing distance from the original surface. The Cube component maps given in **Figure 4.25** show the Cube covered area. The quantitative analysis resulted in the Cube component being 10.3 % at the surface of the sample, 12.9 % at 100 µm below the surface, 19.7 % at the position located at ¾ of the original thickness and 28.2 % at ½ of specimens' depth. The nearly three times increased amount of Cube oriented grains suggests the assumption of surface effects in the *in situ* measurements.

For clarification of this behavior, the same bulk measurements were performed on an equally heat-treated sample. Since this sample showed Cube covered partition fractions being about 20 % at all four positions, the influence of surface effects should be neglectable.

4.7 Particle Stimulated Nucleation: Alloying elements

The evaluation of the experiments above hardly considers the effects of the alloying additions on the microstructure and the final texture in the material. This section sums up different impacts of alloying elements and their changes during heating.
The standard composition range of the AA 6016 alloy is given in **Table 4.1** and the typical microstructure is shown in **Figure 4.3** and **Figure 4.4** respectively. The precipitates play a major role in the recrystallization behavior of aluminum since they affect the mobility of grain boundaries and therefore the speed of recrystallization.

Apart from the grain orientations and the stored energy within the whole grains, the differences between the aluminum matrix and second phase particles are of peculiar interest. Depending on the nature of the particle, meaning whether it is deformable or non-deformable, the resulting microstructure in their nearest vicinity shows tremendous differences. Non-deformable particles lead to the formation of additional dislocations during deformation and regions of increased stored energy, whereas deformable ones can be cut or passed by the dislocations by various mechanisms. However, precipitates' sizes are one of the most important issues. While small particles (< 1 µm approximately), finely dispersed in the Al matrix trend to pin the grain boundaries and thus impede their movement, particles of larger size (> 1 µm approximately) form the basis for particle-stimulated nucleation. This recrystallization mechanism, where the nuclei mainly evolve in the deformation zones around the particles and form characteristic texture components in the annealed microstructure, competes with the classical recrystallization processes such as SIBM (Humphreys and Hatherly 2004; Engler and Hirsch 2009; Bennett *et al.* 2010; Sidor, Petrov and Kestens 2011).

As shown in **Figure 4.4**, the used AA 6016 sheet contains particles of different sizes. Typically suitable for PSN, the AlFeSi-precipitates extend the minimum size mentioned above. In contrast, the Mg_2Si particles with a size around or below 1 µm can exert a strong Zener drag on the grain boundaries (Wang *et al*. 2015).

The first evaluation of elemental distributions was done using the results of the surface of sample 1. **Figure 4.26** depicts the changes in the elemental distributions of Fe and Mg, while those of Si and O are given in **Figure 4.27**.

The Fe-mapping shows statistically distributed particles all over the surface, which do not exhibit a change during annealing. The particle size and the average EDXS signal intensity both remain constant, which implies that Fe containing particles are not affected by solubility or diffusion processes up to temperatures of 550 °C.

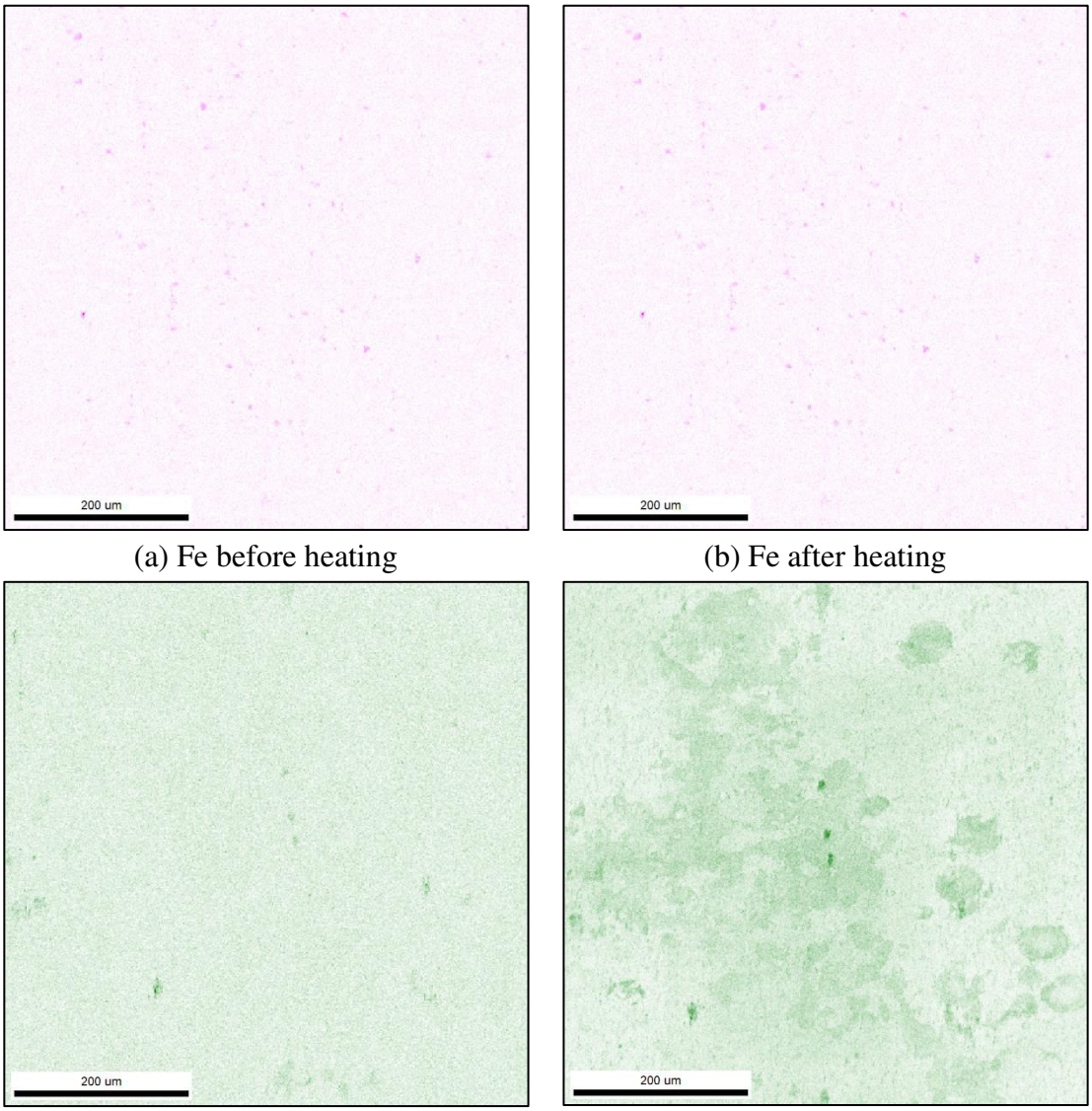

(a) Fe before heating (b) Fe after heating

(c) Mg before heating (d) Mg after heating

Figure 4.26: EDXS element maps from the surface of sample 1; (a) and (b) Fe, (c) and (d) Mg before and after heating

Different results were obtained for Mg, which shows enhanced presence at the surface after the heat treatment. The high temperatures influence the diffusivity and solubility of Mg in Al and can thus lead to a complete re-arrangement of the element in the matrix.
Comparing **Figure 4.26** and **Figure 4.27**, a correspondence between the O and Mg mappings can be noted, in particular, that the magnesium diffusing to the surface reacts with the ambient oxygen. This resembles high-temperature corrosion.

Although silicon shows similar behavior and is clearly redistributed, it seems to dissolve and precipitate again, which is in contrast to the Mg mappings. The Mg_2Si particles cannot be clearly identified in these maps at the magnifications used for the mappings.

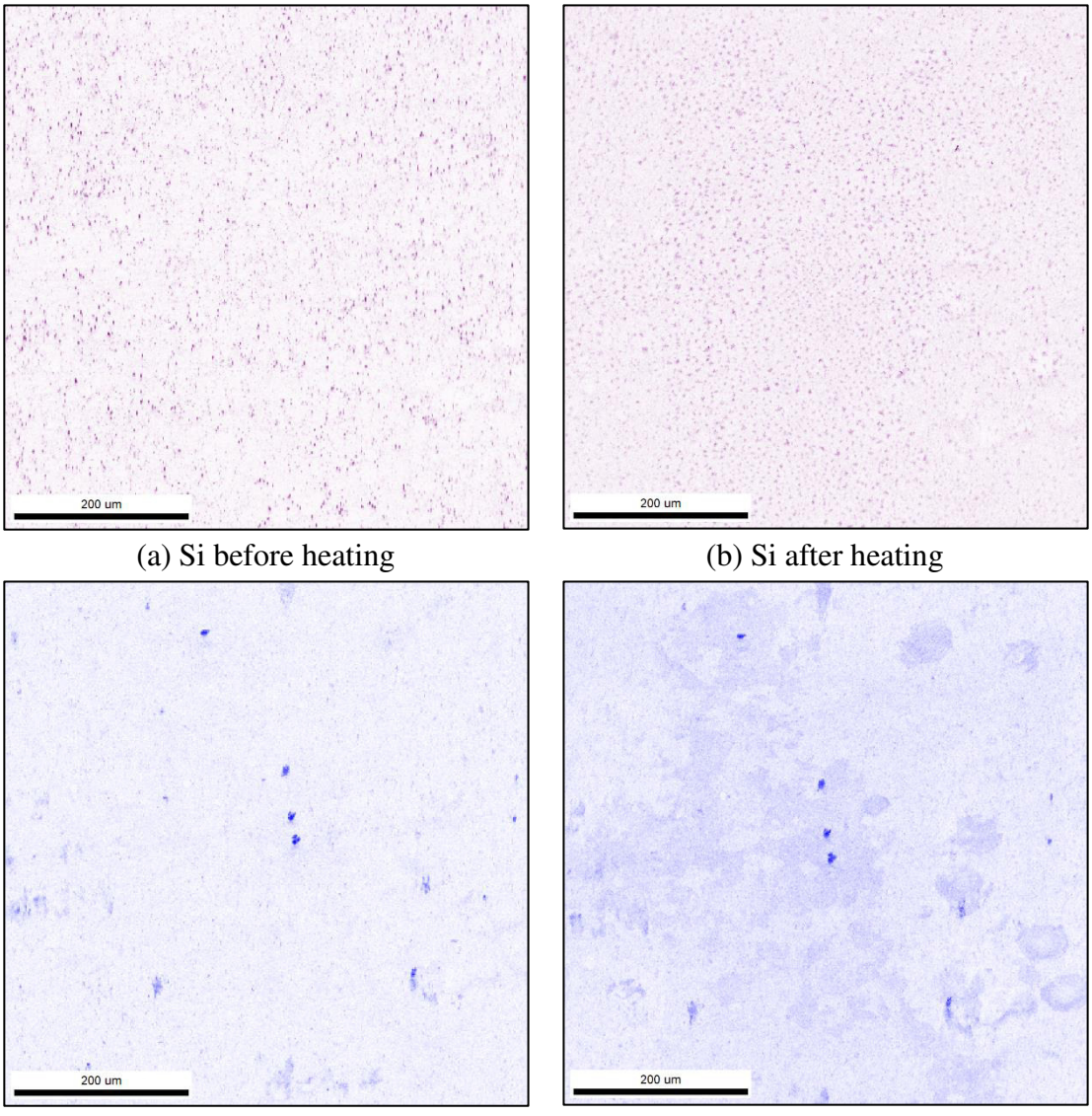

(a) Si before heating (b) Si after heating

(c) O before heating (d) O after heating

Figure 4.27: EDXS element maps from the surface of sample 1; (a) and (b) Si, (c) and (d) O before and after heating

The results from the surface of sample 1 reveal the differences in the distribution of the alloying elements and point to more general processes in materials during heating such as diffusion and solution of elements.

By analyzing and discussing the results of elemental distributions of the samples 6 and 7, which are shown in **Figure 4.28** and **Figure 4.29** respectively, more information concerning PSN and related texture development in the used AA 6016 material were achieved. For easier identification of the small particles only the areas are depicted, which were permanently scanned during the *in situ* heating experiment. The relative positions of these on the surface of the sample are given in the appendix.

Evaluation of the Fe, Mg and Si distributions in both figures indicates very small differences, which can be reasoned by the lower maximum temperature in this case compared to sample 1, possibly below the temperature where surface oxidation starts. The iron elemental map displays dispersion of the iron-containing (often probably AlFeSi) particles all over the area, which is verified by comparison to the spread of silicon. The major problem is again the identification of Mg_2Si particles because either the resolution or the magnification is not sufficient for their observation. However, since obtaining their presence in the microstructure earlier, they are suggested to be present.

Wang *et al.* (2015) also showed the influence of particles in their alloys on final microstructure and texture as well as the impacts of the heating rates on the same. They showed that the AlFeSi-phase in the materials is related to PSN and the final texture, especially the one of the fast heated samples, mainly consists of the $Cube_{ND}$ orientation. In contrast to this, the slowly heated samples showed both a pronounced Cube component and other typical recrystallization texture orientations.

Comparing the results of sample 6 and 7 with literature, PSN seems to be most widely suppressed, since both samples showed classical recrystallization texture components. Texture analysis of the fast heated sample concerning PSN components (P and $Cube_{ND}$) resulted in the area fractions being 0.1 % for $Cube_{ND}$, whereas P orientation was not found at all in the final texture. One possible explanation therefore is that during recrystallization the Cube nuclei outweigh the PSN sites and thus dominate the resulting texture. Another aspect is the heating rate, which is faster in the experiments done by Wang *et al.* (2015). However, for verification of the absence of PSN further *in situ* experiments on very small areas with high resolutions are an absolute necessity.

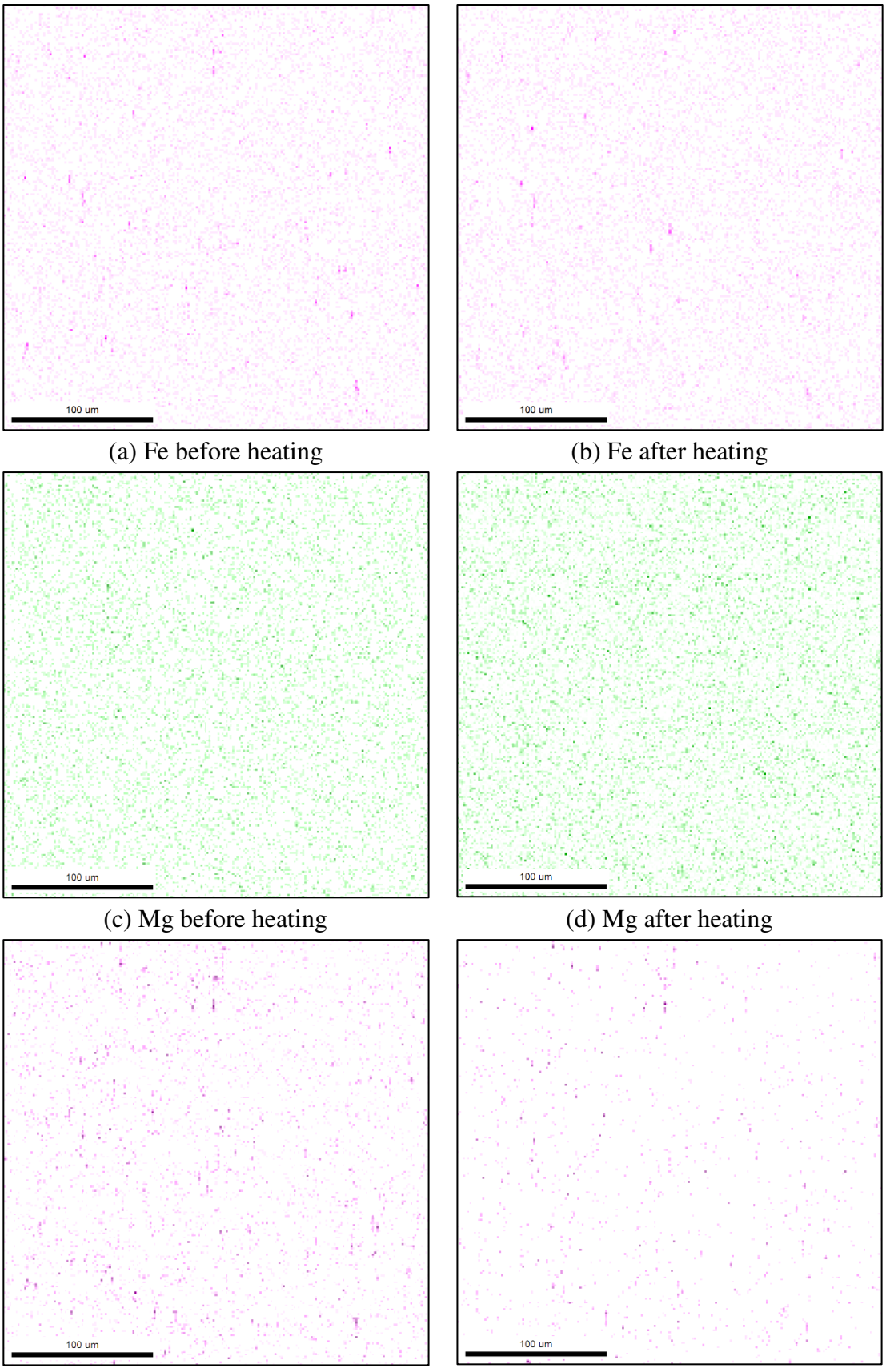

(a) Fe before heating

(b) Fe after heating

(c) Mg before heating

(d) Mg after heating

(e) Si before heating

(f) Si after heating

Figure 4.28: EDXS element distributions maps of sample 6; (a) and (b) Fe, (c) and (d) Mg, (e) and (f) Si before and after heating

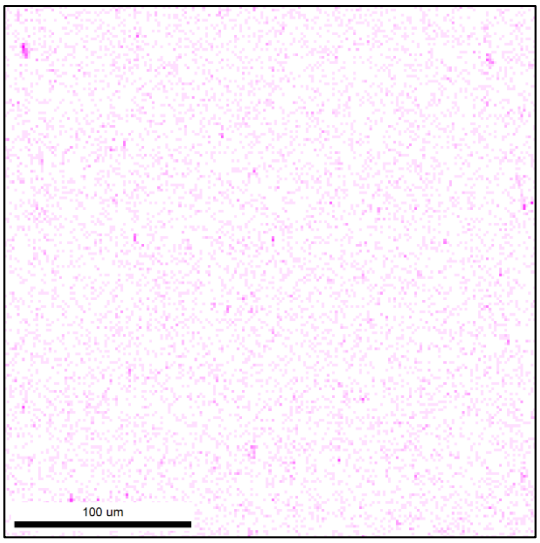

(a) Fe before heating

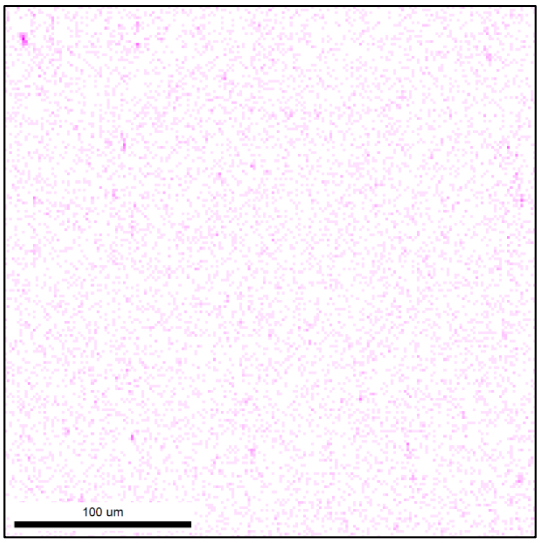

(b) Fe after heating

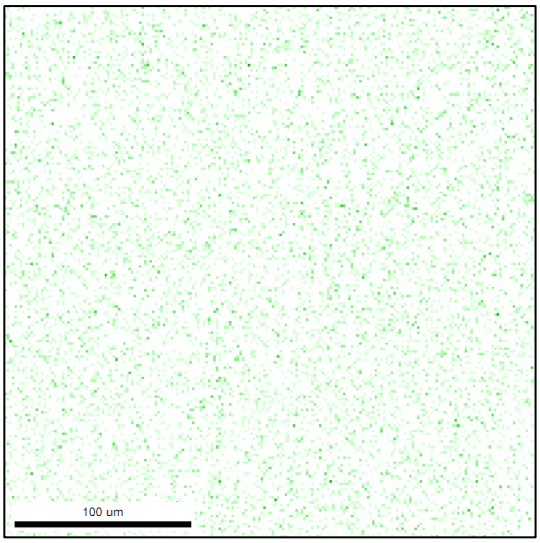

(c) Mg before heating

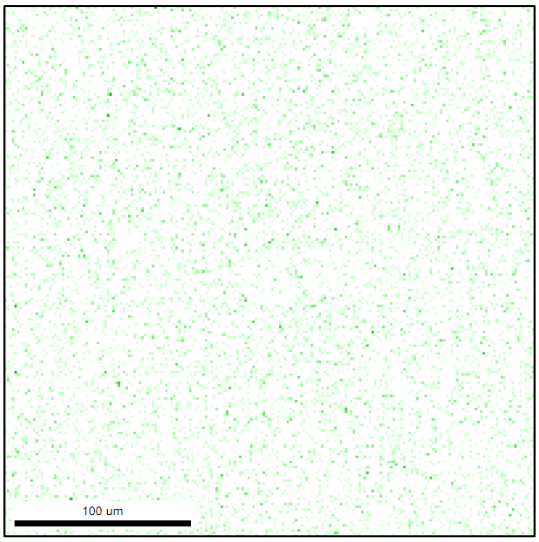

(d) Mg after heating

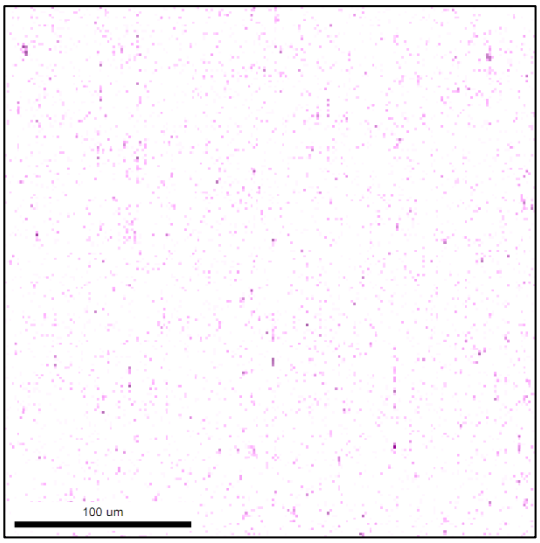

(e) Si before heating

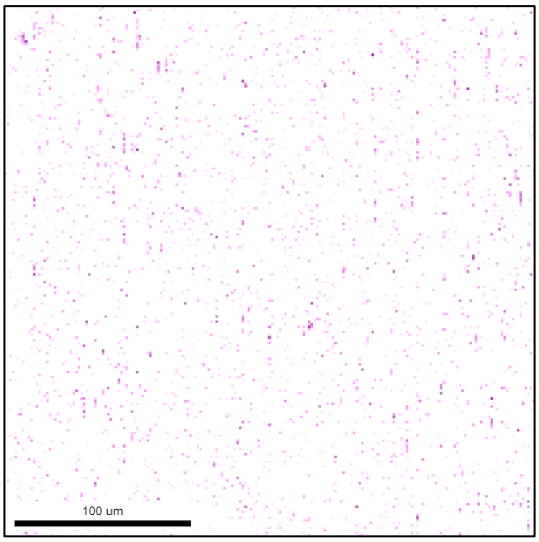

(f) Si after heating

Figure 4.29: EDXS element distributions maps of sample 7; (a) and (b) Fe, (c) and (d) Mg, (e) and (f) Si before and after heating

5 Summary

The aim of this master thesis was the study of the recrystallization behavior of hot rolled aluminum sheets relating to heat treatments. To this aim, electron backscatter diffraction in the scanning electron microscope (SEM) in combination with a CH0-4 heating device (by Kammrath & Weiss) was used. This system enables the *in situ* observation of the changes of the microstructure of materials during heat treatments. To gain reliable EBSD data, at the start the calibration of the whole system was necessary. Furthermore, the undesirable heating of the surrounding SEM parts like detectors and the phosphor screen of the EBSD system caused by heat radiation from the heating stage was investigated. To avoid any damage the temperature at the respective parts should not exceed specified values, and this may limit the maximum temperature that can be applied during the heating experiments. Finally, the microstructure of the samples, the presence of specific texture components, and the distribution of alloying elements and precipitates before and after the heat treatment were analyzed.

The calibration of the EBSD setup was necessary to get a proper indexing of the obtained Kikuchi patterns. Using a Ni-standard, which provides high quality patterns, the coordinates of the pattern center in the TSL OIM software were updated for different working distances (WD) and screen to sample distances (d_{ss}). Furthermore, formulas for the calculation of y* and z* for all different combinations of WD and d_{ss} were derived.

At the start of the experiments, the chemical composition of the AA 6016 sheets was analyzed using the different imaging detectors of the SEM in combination with the attached EDX system. Different precipitates were detected, among them the most common found in such sheets like Mg_2Si and AlFeSi particles. Having different sizes ranging from about 100 nm up to a few microns, they can influence the evolution of the microstructure drastically.
The first *in situ* measurements showed the microstructural evolution of the already recrystallized (during hot rolling) surfaces of the aluminum sheets. Since the corresponding kernel average misorientation (KAM) maps indicated low dislocation densities even before heat treatment, only grain growth but no occurrence of recrystallization nuclei was observed during heating.
Though, the variation in recrystallization behavior as a function of the position at the sheets' cross-section was of major interest. The reason is that the rolling process induces different levels of shear deformation at different depths in the aluminum sheets. Thus the microstructural

transformation will also be different throughout the sample. However, the obtained results gained at positions of T/4 and T/2 showed no significant differences, since the grains had similar aspect ratios and statistically distributed orientations. Clearly evident from the KAM maps of these measurements was the reduction of internal stress in the recrystallized areas. At greater depth below the surface the main mechanisms of recrystallization, namely the strain induced boundary migration (SIBM), where grains grow at the expense of others until they meet another grain boundary, could be observed. Furthermore, studying the samples' microstructures reveals preferred orientation of nucleation being close to <101> followed by the Cube orientation <001>.

Further experiments showed the influence of the heating rate on the evolution of the microstructure. While slowly heated samples showed elongated grains in rolling direction with high aspect ratios, the fast heated samples showed a higher number of grains with length/width ratios close to 1. This effect is due to the competition between growth and nucleation rate.

Since the EBSD signals arise from a depth of around 100 nm, surface effects caused by surface tension or even high temperature corrosion could not be excluded a priori. Therefore, also the changes in the microstructure of the bulk of the samples were investigated. The first results obtained at different depths below the original surface during heating showed no differences in the grain shape but seemed to indicate an increase in the fraction of the Cube texture component with increasing depth. However, this increase in the Cube texture could not be reproduced when repeating the bulk measurements on a specimen using the same parameters for the heat treatment. Thus, either the fraction of the Cube component can vary substantially even in case of the same heat treatment or the investigated areas were too small to get statistically significant results.

Moreover, the focus of this master thesis was put on the analysis of textural changes during heat treatments. The typical rolling texture, which is introduced during hot rolling as well as cold rolling, transforms during the subsequent heat treatment into a typical recrystallization texture. The change in amount of the Cube component, one major component of the recrystallization texture and responsible for the so-called roping effect, was of particular interest. Although the performed heat treatments did not show the desired major reduction of Cube amount per se, the change in shape and size of the Cube oriented grains presumably positively influences the material concerning roping effects. If the final surface quality of the intermediately annealed sheets tops the properties of the commercially manufactured sheets, an intermediate annealing process between hot and cold rolling passes is recommended.

Finally, the influence of the alloying elements on the recrystallization behavior was analyzed. The particles with their varying size can affect the transformation of the microstructure in two different ways: Zener pinning of grain boundaries caused by small particles (Mg_2Si) and particle stimulated nucleation (PSN) initiated by bigger particles (AlFeSi). Since the measured areas were chosen relatively large to get reliable results concerning textural changes, the observation of the particle-induced effects was very difficult. While Zener pinning is usually suspected to be present in all materials, more or less no signs for particle-stimulated nucleation were observed in the measurements. Additional investigations concerning PSN are recommended, since particle stimulated nucleation is one key to get more control over the final microstructure and texture components.

Other important issues are the diffusion and solution of alloying elements during heating up to high temperatures (550 °C). Especially Mg and Si elemental maps showed significant differences in their distributions before and after heating and therefore their influence on the recrystallization mechanisms has to be elucidated.

6 Bibliography

Baczynski, G.J., Guzzo, R., Ball, M.D. and Lloyd, D.J. 2000. “Development of Roping in an Aluminum Automotive Alloy AA6111.” *Acta Materialia* 48 (13). Pergamon: 3361–76. doi:10.1016/S1359-6454(00)00141-5.

Bay, B., Hansen, N. and Kuhlmann-Wilsdorf, D. 1992. “Microstructural Evolution in Rolled Aluminium.” *Materials Science and Engineering A* 158 (2). Elsevier: 139–46. doi:10.1016/0921-5093(92)90002-I.

Beck, P.A. and Sperry, P.R. 1950. “Strain Induced Grain Boundary Migration in High Purity Aluminum.” *Journal of Applied Physics* 21 (2). American Institute of Physics: 150–52. doi:10.1063/1.1699614.

Bennett, T.A., Petrov, R.H., Kestens, L., Zhuang, L.-Z. and de Smet, P. 2010. “The Effect of Particle-Stimulated Nucleation on Texture Banding in an Aluminium Alloy.” *Scripta Materialia* 63 (5): 461–64. doi:10.1016/j.scriptamat.2010.04.028.

Bennett, T.A., Sidor, J., Petrov, R.H. and Kestens, L. 2010. “The Effect of Intermediate Annealing on Texture Banding in Aluminum Alloy 6016.” *Advanced Engineering Materials* 12 (10). WILEY-VCH Verlag: 1018–23. doi:10.1002/adem.201000072.

Burger, G.B., Gupta, A.K., Jeffrey, P.W. and Lloyd, D.J. 1995. “Microstructural Control of Aluminum Sheet Used in Automotive Applications.” *Materials Characterization* 35 (1): 23–39. doi:10.1016/1044-5803(95)00065-8.

Chen, P., Mao, S.C., Liu, Y., Wang, F., Zhang, Y.F., Zhang, Z. and Han, X.D. 2013. “In-Situ EBSD Study of the Active Slip Systems and Lattice Rotation Behavior of Surface Grains in Aluminum Alloy during Tensile Deformation.” *Materials Science and Engineering: A* 580 (September): 114–24. doi:10.1016/j.msea.2013.05.046.

De La Chapelle, S. 2001. “Cube Recrystallization Textures in a Hot Deformed Al-Mg-Si Alloy.” *Scripta Materialia* 45 (12): 1387–91. doi:10.1016/S1359-6462(01)01174-5.

Dillamore, I.L. and Katoh, H. 1974. “The Mechanisms of Recrystallization in Cubic Metals with Particular Reference to Their Orientation-Dependence.” *Metal Science* 8 (1). Taylor & Francis: 73–83. doi:10.1179/msc.1974.8.1.73.

Engler, O. and Hirsch, J. 2002. “Texture Control by Thermomechanical Processing of AA6xxx Al-Mg-Si Sheet Alloys for Automotive Applications-a Review.” *Materials Science and Engineering: A* 336 (1–2): 249–62. doi:10.1016/S0921-5093(01)01968-2.

Engler, O. and Hirsch, J. 2009. “Control of Recrystallisation Texture and Texture-Related Properties in Industrial Production of Aluminium Sheet.” *International Journal of Materials Research* 100 (4). Carl Hanser Verlag: 564–75. doi:10.3139/146.110063.

Goldstein, J.I., Newbury, D.E., Echlin, P., Joy, D.C., Lyman, C.E., Lifshin, E., Sawyer, L. and Michael, J.R. 2003. *Scanning Electron Microscopy and X-Ray Microanalysis*. Third. Boston, MA: Springer US. doi:10.1007/978-1-4615-0215-9.

Hamad, K., Yang, H.W. and Ko, Y.G. 2016. “Interpretation of Annealing Texture Changes of Severely Deformed Al-Mg-Si Alloy.” *Journal of Alloys and Compounds* 687: 300–305. doi:10.1016/j.jallcom.2016.06.101.

Hawkes, P. and Spence, J.C.H. 2008. *Science of Microscopy*. Volume I. Springer Science & Business Media.

Hirsch, J. and Al-Samman, T. 2013. “Superior Light Metals by Texture Engineering: Optimized Aluminum and Magnesium Alloys for Automotive Applications.” *Acta Materialia* 61 (3): 818–43. doi:10.1016/j.actamat.2012.10.044.

Hirsch, J. and Lücke, K. 1985. “The Application of Quantitative Texture Analysis for Investigating Continuous and Discontinuous Recrystallization Processes of Al-0.01 Fe.” *Acta Metallurgica* 33 (10). Pergamon: 1927–38. doi:10.1016/0001-6160(85)90015-X.

Humphreys, F. J. and Hatherly, M. 2004. *Recrystallization and Related Annealing Phenomena*. Second. Pergamon.

Hurley, P.J. and Humphreys, F.J. 2003. “The Application of EBSD to the Study of Substructural Development in a Cold Rolled Single-Phase Aluminium Alloy.” *Acta Materialia* 51 (4): 1087–1102. doi:10.1016/S1359-6454(02)00513-X.

Kammrath, W. and Weiss, K. n.d. “Betriebsanleitung Für Das 1050 °C Heizmodul (CH0-4).”

Krieger Lassen, N.C. 1996. “Automatic Localisation of Electron Backscattering Pattern Bands from Hough Transform.” *Materials Science and Technology* 12 (10). Taylor & Francis: 837–43. doi:10.1179/mst.1996.12.10.837.

Molodov, D.A., Czubayko, U., Gottstein, G. and Shvindlerman, L.S. 1998. “On the Effect of Purity and Orientation on Grain Boundary Motion.” *Acta Materialia* 46 (2). Pergamon: 553–64. doi:10.1016/S1359-6454(97)00277-2.

OIM, Manual. 1997. “TSL OIM Data Collection Software - Manual.”

Petzow, G. 2006. *Metallographisches, Keramographisches, Plastographisches Ätzen*. Gebrüder Borntraeger Berlin.

Randle, V. and Engler, O. 2000. *Introduction to Texture Analysis: Macrotexture, Microtexture and Orientation Mapping*. Gordon and Breach Science Publishers.

Schwartz, A.J., Kumar, M. and Adams, B.L. 2000. *Electron Backscatter Diffraction in Materials Science*. First. Kluwer Academic / Plenum Publishers.

Schwartz, A.J., Kumar, M., Adams, B.L. and Field, D.P. 2009. *Electron Backscatter Diffraction in Materials Science*. Vol. 2. Springer.

Sidor, J.J., Petrov, R.H. and Kestens, L. 2011. “Modeling the Crystallographic Texture Changes in Aluminum Alloys during Recrystallization.” *Acta Materialia* 59 (14): 5735–48. doi:10.1016/j.actamat.2011.05.050.

Somerday, M. and Humphreys, F.J. 2003. “Recrystallisation Behaviour of Supersaturated Al – Mn Alloys Part 1 – Al – 1 . 3 Wt- % Mn.” *Materils Science and Technology* 19 (1). Taylor & Francis: 20–29. doi:10.1179/026708303225008590.

Suwas, S. and Ray, R.K. 2014. *Crystallographic Texture of Materials*. Engineering Materials and Processes. London: Springer London. doi:10.1007/978-1-4471-6314-5.

Wang, X., Guo, M., Cao, L., Luo, J., Zhang, J. and Zhuang, L. 2015. “Effect of Heating Rate on Mechanical Property, Microstructure and Texture Evolution of Al-Mg-Si-Cu Alloy during Solution Treatment.” *Materials Science and Engineering A* 621 (January). Elsevier: 8–17. doi:10.1016/j.msea.2014.10.045.

Appendix

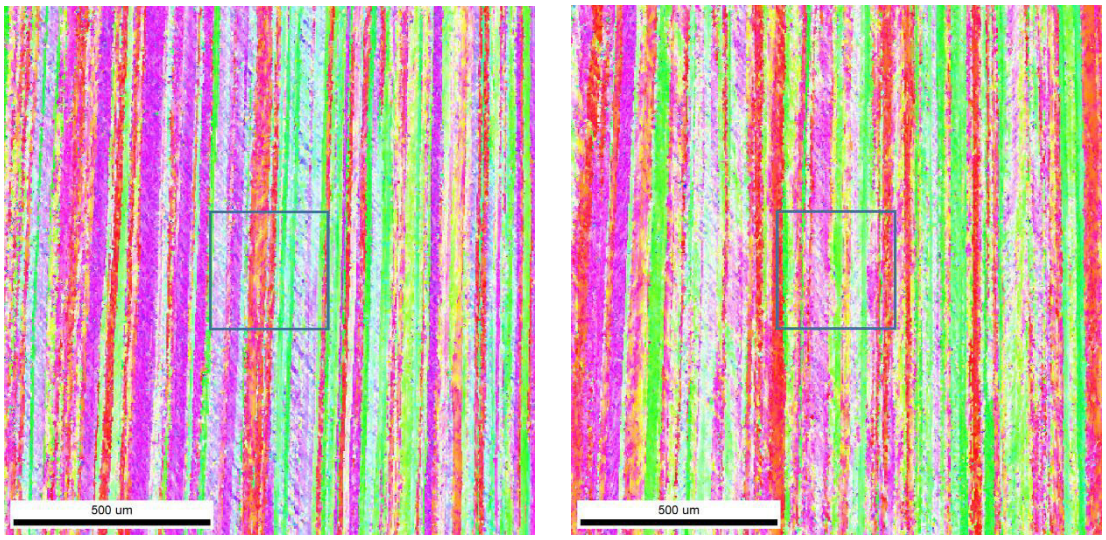

(a) Overview sample 6 (b) Overview sample 7

Figure 7.1: Position of the permanently scanned areas in the overview IPF maps of (a) sample 6 and (b) sample 7

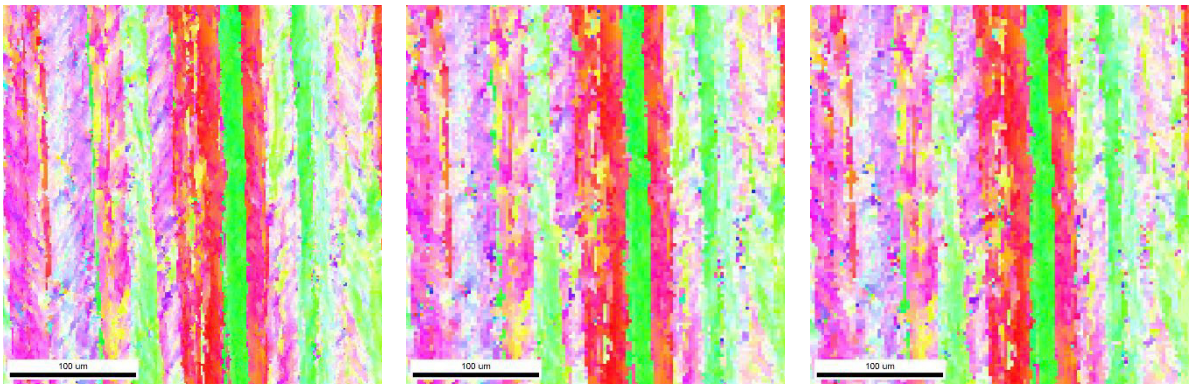

(a) RT (b) 340 °C (c) 345 °C

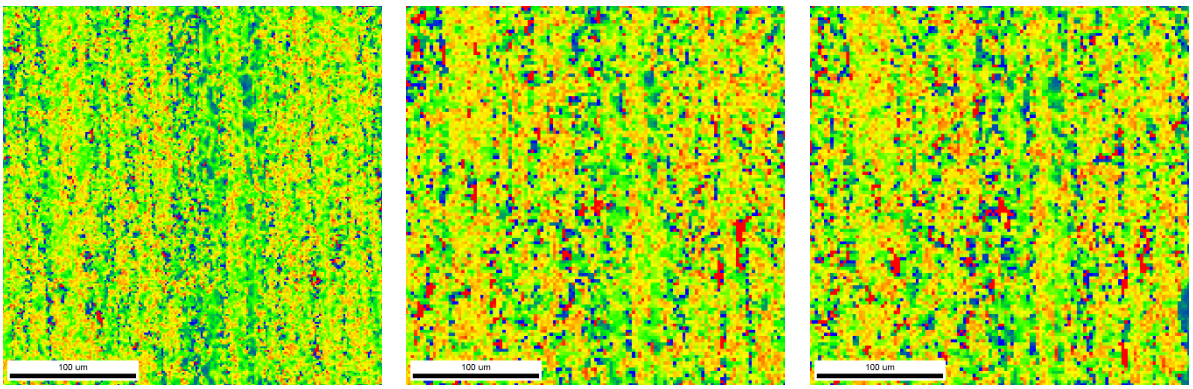

(a) RT (b) 340 °C (c) 345 °C

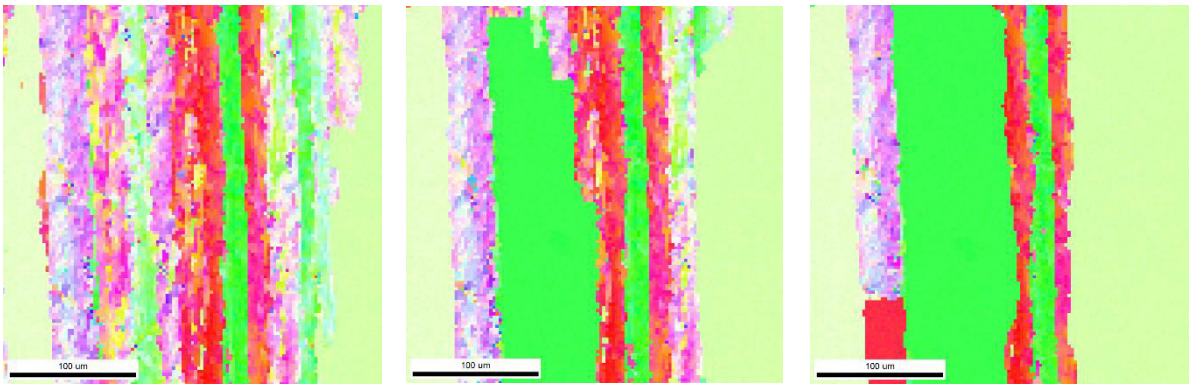

(d) 350 °C (e) 360 °C (f) 380 °C

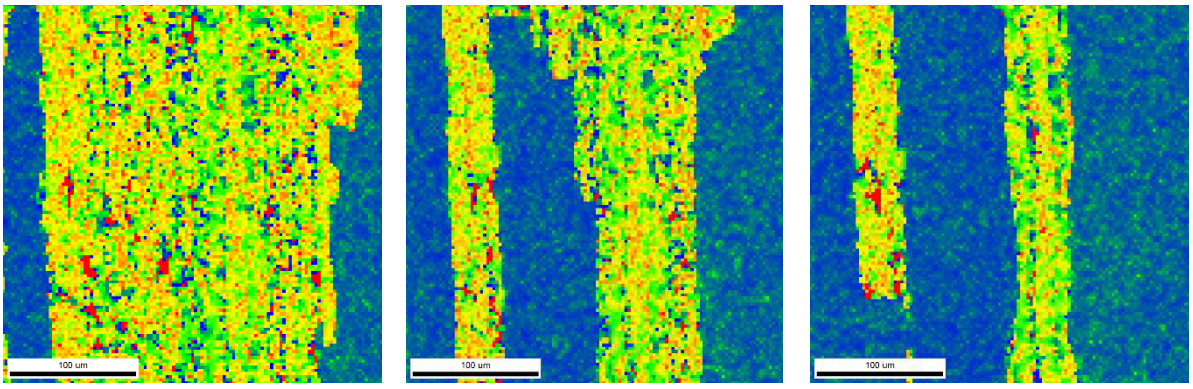

(d) 350 °C (e) 360 °C (f) 380 °C

Figure 7.2: Step-by-step evolution of the microstructure of sample 2; step-size: (a) 1.5 µm, (b)-(f) 2.5 µm

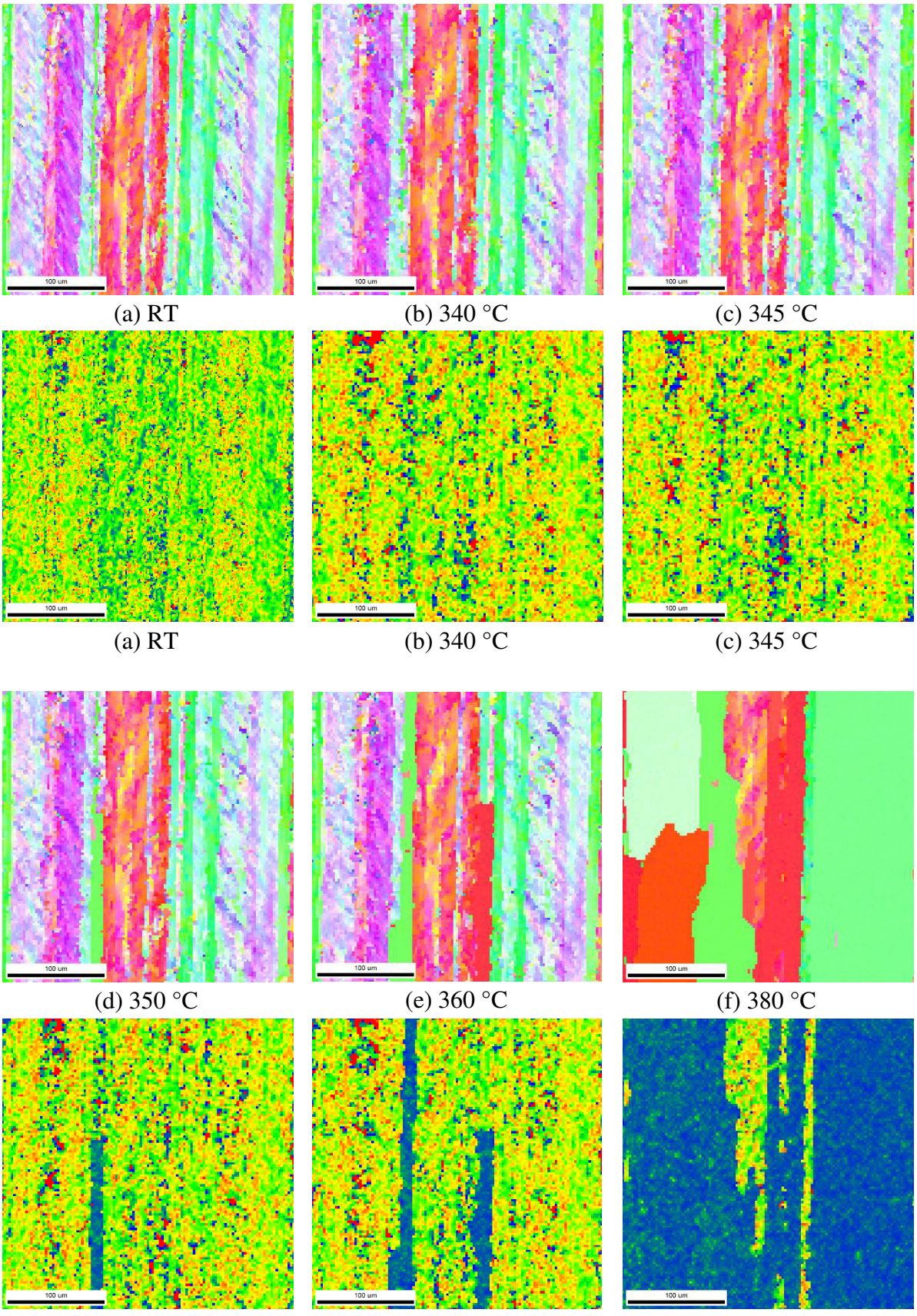

(a) RT (b) 340 °C (c) 345 °C

(a) RT (b) 340 °C (c) 345 °C

(d) 350 °C (e) 360 °C (f) 380 °C

(d) 350 °C (e) 360 °C (f) 380 °C

Figure 7.3: Step-by-step evolution of the microstructure of sample 3; step-size: (a) 1.5 µm, (b)-(f) 2.5 µm

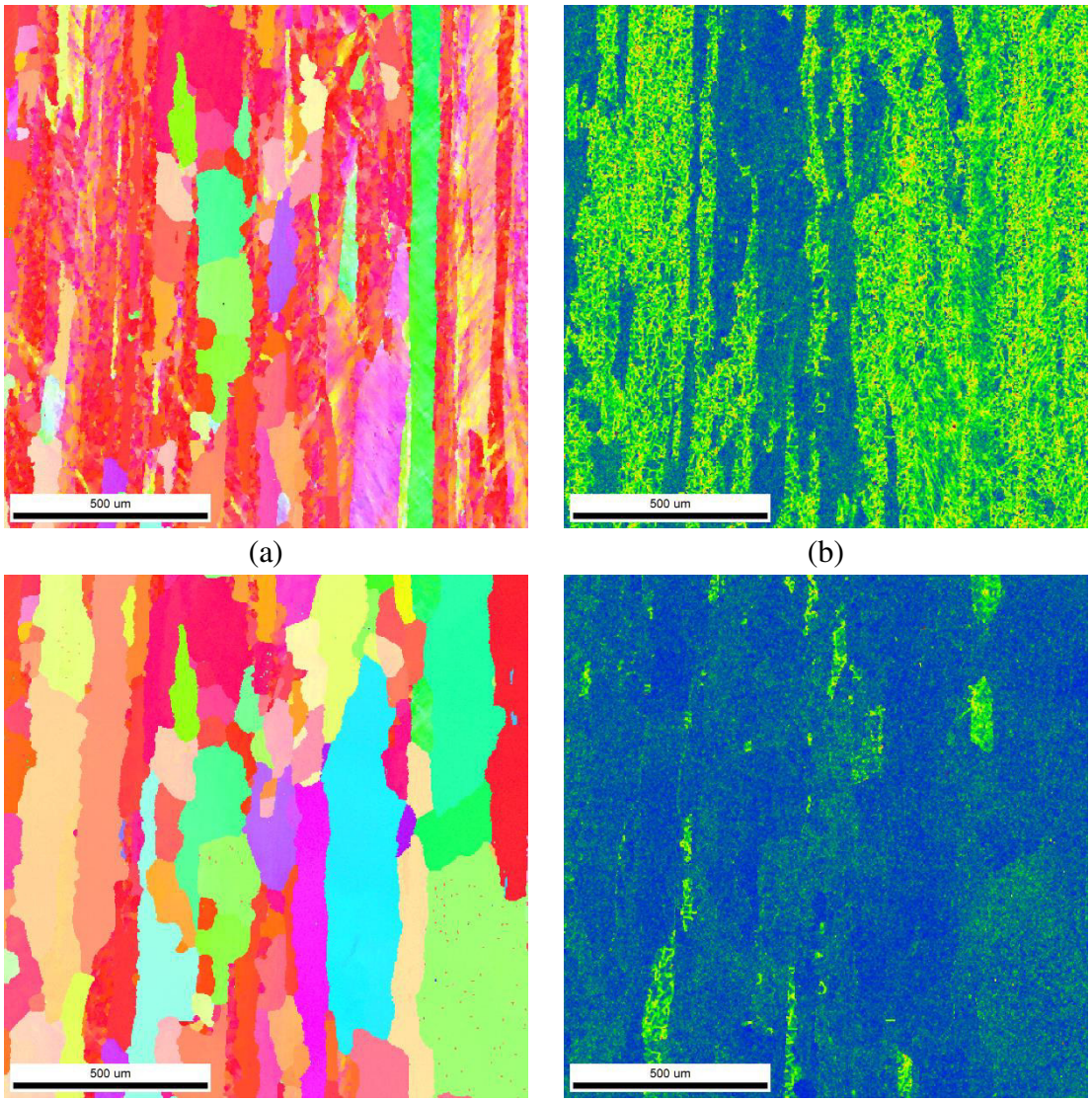

(a) (b)

(c) (d)

Figure 7.4: Overview IPF and KAM maps of sample 5 (a) and (b) before heating, (c) and (d) after heating; step-size: 3 µm